0 0 0 0 0 4 0 0 0 9 4 7

LBL-1973

c.1

GEOMETRY OF SOME METAL HALIDES

RECEIVED
LAWRENCE
RADIATION LABORATORY

NOV 26 1973

LIBRARY AND
DOCUMENTS SECTION

Peter Alan Yarnell

(Ph. D. Thesis)

July 1973

Prepared for the U. S. Atomic Energy Commission
under Contract W-7405-ENG-48

For Reference

Not to be taken from this room

LAWRENCE BERKELEY LABORATORY
UNIVERSITY OF CALIFORNIA
BERKELEY

LBL-1973

c.1

DISCLAIMER

This document was prepared as an account of work sponsored by the United States Government. While this document is believed to contain correct information, neither the United States Government nor any agency thereof, nor the Regents of the University of California, nor any of their employees, makes any warranty, express or implied, or assumes any legal responsibility for the accuracy, completeness, or usefulness of any information, apparatus, product, or process disclosed, or represents that its use would not infringe privately owned rights. Reference herein to any specific commercial product, process, or service by its trade name, trademark, manufacturer, or otherwise, does not necessarily constitute or imply its endorsement, recommendation, or favoring by the United States Government or any agency thereof, or the Regents of the University of California. The views and opinions of authors expressed herein do not necessarily state or reflect those of the United States Government or any agency thereof or the Regents of the University of California.

0 0 0 0 4 0 0 0 3 4 8

GEOMETRY OF SOME METAL HALIDES

Contents

Abstract. vii

I. Introduction. 1

II. Polarizable Ion Model for the Alkaline Earth Dihalides. 4

A. Introduction. 4

B. Construction of the Model 5

C. Derivation of the Electrostatic Potential Energy of the System 9

D. Calculation of the Bending Potential Energy Curves. 20

E. Physical Constants Derived from the Model 21

F. Extension of the Model to Other Triatomics. 32

1. Transition Metal and Group II-b Dihalides 32

2. Europium Dihalides. 35

3. Group IV-a Dihalides. 46

G. Concluding Remarks. 47

III. The "Linear" Polarizable Ion Model. 49

A. Introduction. 49

B. Construction of the Model 49

C. Derivation of the Repulsion Interaction Energy. 50

D. Derivation of the Force on a Bond 54

E. Derivation of the Stretching Force Constant 61

F. Derivation of the Stretching Frequencies. 62

1. Non-Linear Symmetric MX_2 Molecules. 62

2. Linear Symmetric MX_2 Molecules. 63

G. Calculation of Molecular Constants. 63

H. Concluding Remarks 68

IV. Electric Deflection Spectroscopy 72

A. Introduction 72

B. Theory 73

C. Deflection System 74

V. Experimental Apparatus and Procedures 77

A. Introduction 77

B. Apparatus 77

C. Details of Modifications for Electric Deflection Experiments 80

1. Molecular Beam Source Oven 80

2. Electric Deflecting Field 82

3. Phase Sensitive Detection System 86

D. Multichannel Analyzer Data Retrieval System 88

E. Experimental Procedures 89

1. Operational Checks 89

2. Experimental Modifications 89

3. Experimental Techniques 91

VI. Experimental Results 94

A. Introduction 94

B. Calibration Standards 96

1. Lithium Bromide (LiBr) 96

2. Zinc Fluoride (ZnF_2) and Cadmium Bromide ($CdBr_2$) 97

C. Alkaline Earth Dihalides 101

1. Barium Dihalides (BaF_2 and $BaCl_2$) 101

2. Strontium Dihalides ($SrCl_2$, $SrBr_2$, and SrI_2) 107

3. Calcium Dihalides (CaF_2 and $CaCl_2$). 111

4. Magnesium Dihalides (MgF_2 and $MgCl_2$). 117

D. Rare Earth Halides. 121

1. Lanthanum Fluoride (LaF_3) 121

2. Europium Dihalides ($EuCl_2$, $EuBr_2$, EuI_2) 125

E. Summary 132

VII. Conclusions 137

Acknowledgments 139

Appendix A-1. 141

Appendix A-2. 160

Appendix A-3a 176

Appendix A-3b 179

Appendix A-4. 183

References. 188

GEOMETRY OF SOME METAL HALIDES

Peter Alan Yarnell

Lawrence Berkeley Laboratory
University of California
Berkeley, California 94720

July 1973

ABSTRACT

Two polarizable ion models are developed to describe the gas phase of metal dihalide molecules. Both models employ electrostatic and repulsive interactions to predict molecular geometries and molecular constants. The first model is applied to the dihalides of the alkaline earths, group II-b metals, transition metals, group IV-a metals, and europium. In addition to the molecular geometry, bending frequencies (ν_2) are derived for most of these molecules. The second or "linear" model is applied to the alkaline earth dihalides; equilibrium internuclear bond lengths (ℓ), stretching force constants (k_1) and stretching frequencies (ν_1 and ν_3) are determined.

Some of the structural predictions of the polarizable ion model are correlated with experimental data from molecular beam electric deflection spectroscopy. Certain alkaline earth dihalides (BaF_2, $BaCl_2$, $SrCl_2$, $SrBr_2$, SrI_2, CaF_2, $CaCl_2$, MgF_2, and $MgCl_2$) and lanthanum trifluoride (LaF_3) have been reinvestigated to resolve contradictions in some of the earlier experimental work. Significantly improved sensitivity allows more precise determination of geometry. Also, the gas phase geometries of $EuCl_2$, $EuBr_2$, and EuI_2 have been determined using this technique. The correlation between the europium dihalide geometries and analogous alkaline earth dihalides is explored.

I. INTRODUCTION

Debye[1] first considered ions as polarizable entities in studying the problem of bonding in the water molecule. Rittner[2] used this concept to formulate a polarizable ion model to predict and correlate certain physical properties of the alkali halide molecules. He assumed the bonding in these molecules to be largely ionic; consequently, the interactions between ions were governed by electrostatics. The success of the Rittner model triggered other investigations[3-6] along the same lines. The agreement of the polarizable ion model, more commonly termed the ionic model, with experimental evidence was rather poor for the alkali halides. More recently, Street and co-workers[7-9] have modified and refined the polarizable ion model for the alkali halides by including several effects previously neglected. The success of their model was a primary motivation for this investigation of models for the alkaline earth dihalides.

Any polarizable ion model is only an approximate solution to the problem of interactions within a molecular system. Because the electrostatic and repulsive interactions are interrelated, a rigorous solution requires quantum mechanics. This is a very difficult problem. Instead, the polarizable ion model <u>separates</u> these two interactions: the electrostatic part is calculated classically while the repulsion term is empirically chosen. A comparison of values of molecular parameters predicted by a polarizable ion model with experimental data should give an indication of the validity of the "separation" approximation.

Two polarizable ion models for the <u>gas phase</u> alkaline earth dihalides are presented in this dissertation. The first of these is

based on a polarized metal cation and is used to calculate bending potential curves and bending frequencies for each of the alkaline earth dihalides. The bending potential curves, in turn, determine the geometry of these compounds. The geometries and bending frequencies are found to agree quite well with experimental data. This particular model is extended to include certain dihalides of Group II-b metals, Group IV-a metals, transition metals, and europium. The geometries and bending frequencies of most of these compounds are predicted and compared to experimental data, where available.

The second model for the alkaline earth dihalides is based on polarized halide anions. This model is applied primarily to linear molecules and is used to determine equilibrium internuclear bond lengths, stretching force constants, and stretching frequencies. Comparison between predicted values and experimental data indicates good agreement.

The importance of electric deflection spectroscopy in molecular structure determination is well documented.[10-12] This technique might be regarded as crude in light of today's sophisticated methods of spectroscopy. However, electric deflection has proven most useful in investigations of refractory high temperature systems. Significantly improved sensitivity is achieved with the electric deflection apparatus used for this study. The present work is partially a reinvestigation of certain alkaline earth dihalides and similar metal halides, since previous spectroscopic studies have led to conflicting geometries for some of these molecules. Original electric deflection studies of the europium dihalides (except europium fluoride) are presented, and the geometries of these molecules determined.

Experimental results are correlated with the polarizable ion model theory. The predicted trends in the geometries of groups of molecules are noted, and shown to support the observed data.

II. POLARIZABLE ION MODEL FOR THE ALKALINE EARTH DIHALIDES

A. Introduction

The alkaline earth dihalides are similar to the alkali halides with respect to formation of ionic-type bonds with various halide ligands. However, the ionic character of these bonds is not as pronounced as that of the alkali halides. Hence, a further test of the ionic model is obtained by appropriately modifying it to apply to the alkaline earth dihalides.

Models of this type have intrigued theorists and experimentalists alike for some time. Two early attempts by Pearson[13] and Berry[14] were severely limited by incomplete or incorrect experimental data. Berry's model was a rigorous one, but his calculations contained algebraic errors. The later model of Büchler *et al.*[15] was plagued by sketchy data, and these authors concluded that the ionic model was inappropriate to describe the alkaline earth dihalides.

Several recurrent problems appear in deriving an acceptable polarizable ion model for the alkaline earth dihalides: 1) The inclusion of all *pertinent* multipole interactions between individual ions while keeping the mathematical complexity of the problem to a minimum; 2) The choice of a suitable and consistent set of polarizabilities to describe all ions involved; and 3) The validity of the experimental data with which the model's predictions are to be compared. Our polarizable ion model has been developed after due consideration of the first two dilemmas. Since previous modeling attempts, there has been a vast increase in the amount of experimental data accumulated on these molecules.

B. Construction of the Model

The basis of the polarizable ion model for the gas phase alkaline earth dihalides is three ions arranged in the following configuration (see top drawing on following page). This essentially represents the system by three hard spheres in contact. Each ion is polarized in the field of each of the others. Hence, we attribute to each ion an induced dipole polarizability, an induced quadrupole polarizability, and higher multipole polarizabilities. The two internuclear bonds are assumed to be of equivalent lengths.[16]

A bending angle $\underline{\theta}$ is assigned as a measure of the geometry of the molecule. To determine the equilibrium value of this bending angle (and consequently the molecule's geometry), the potential energy $\underline{V}$ of the gaseous system must be calculated as a function of the bending angle. A stable equilibrium configuration requires a minimum potential energy. A potential energy minimum at the bending angle $\theta = 0^\circ$ denotes a linear molecule. On the other hand, a potential energy minimum at an angle greater than 0° with a significant hump at $\theta = 0^\circ$ indicates a bent molecule. The intermediate cases of small minimum angles and/or small humps are less definitive. For our purposes, a bent molecule is defined as one for which <u>at least</u> one energy level is caught below the hump.

The potential energy of the system is directly attributable to electrostatic and repulsive interactions within the molecule. The repulsive interactions can be further broken down into steric repulsions between the two anions and those between the cation and either anion. In reality, however, all of the various interactions are interrelated and

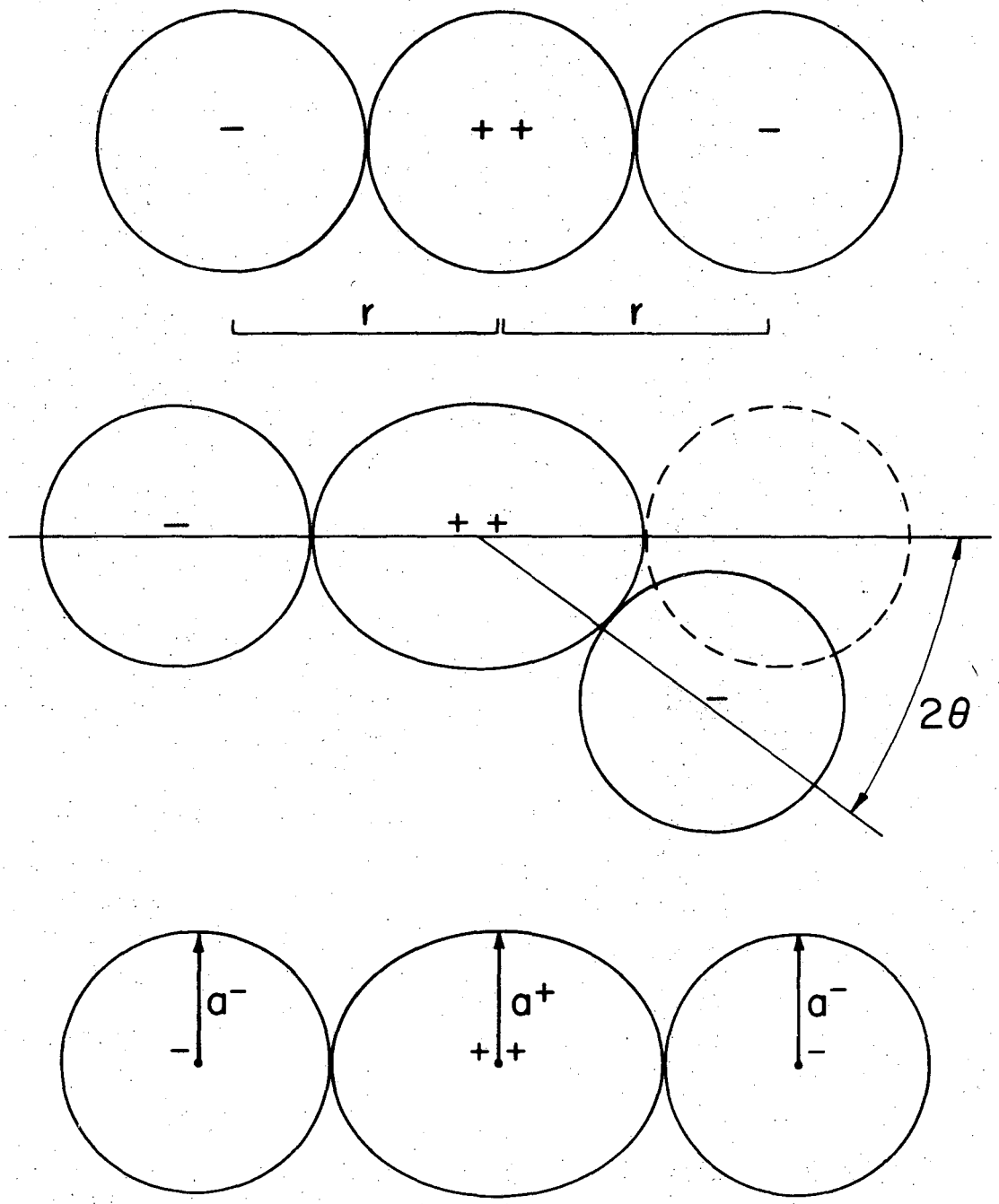

$$\alpha_D^- \equiv |a^-|^3 \qquad \alpha_D^+ \equiv |a^+|^3$$

XBL 735-2871

must be treated jointly using quantum mechanics. As was previously mentioned, the purpose of a polarizable ion model is to simplify this problem by using the approximation that interactions can be treated separately. Thus, the total potential energy can be expressed as the sum of the electrostatic interaction energy between ions $\underline{\phi_{ei}}$ and the repulsive energy between ions $\underline{\phi_r}$:

$$V = \phi_{ei} + \phi_r \quad . \tag{II-1}$$

A major difference between our model and previous attempts[14,15] is that we have incorporated the <u>cation-anion</u> part of the repulsive interaction into the so-called electrostatic interaction. This is accomplished by requiring the effective internuclear distance $\underline{r}$ to be a weak function of the bending angle $\underline{\theta}$ rather than a constant (see middle drawing on page 6). A deformation constant $\underline{k}$ determines the magnitude of the variation in $\underline{r}$:

$$r = \ell(1 - k \sin^2\theta) \quad , \tag{II-2}$$

where ℓ is the equilibrium internuclear distance. Physically, the deformation constant combined with the $\sin^2\theta$ functionality expresses the fact that the deformation of the cation due to the cation-anion repulsions is not spherical but elliptical. For the alkaline earth dihalides, the cation-anion repulsions are "softer" when both anions push on the cation from one side. $\underline{k}$ can be expressed as —

$$k = \frac{h\alpha_D}{\ell} (\alpha_D/\alpha_Q) \quad , \tag{II-3}$$

where $\underline{h}$ is a proportionality constant and $\underline{\alpha_D}$ and $\underline{\alpha_Q}$ are <u>cation</u> dipole and quadrupole polarizabilities, respectively. The direct proportionality of $\underline{k}$ to $\underline{\alpha_D}$ reflects the increased deformation of the cation with an increase in the dipole polarizability. On the other hand, the variation of $\underline{k}$ with (α_D/α_Q) indicates that an increase in the quadrupole polarizability relative to the dipole polarizability reduces the "dipole-like" deformation described above.

The magnitude of the deformation constant $\underline{k}$ is quite small (roughly 6% reduction in $\underline{r}$ at $\theta = 90°$ and on the order of 2 to 3% reduction at typical bending angles of 30°). However, the deformation constant allows certain alkaline earth dihalide molecules to assume bent equilibrium geometries; the alternative required to bend these molecules is an irrationally large metal dipole polarizability.

Although the deformation constant allows an angular dependence in the cation-anion repulsive interaction, the "electrostatic" interactions are still calculated using a system of electrically-charged hard "spheres" (ellipses). Therefore, the effective equilibrium internuclear distance, used in our calculations, varies as a function of the bending angle $\underline{\theta}$.

Any repulsive interaction can only be explained quantum mechanically, using the exclusion principle.[17] Unfortunately, no exact theoretical representation of this term is known. Previously, both exponential, $A\exp(-r/\rho)$, and inverse power, D/r^n, approximations have been used to represent experimental data.[18-22]

Because of the relatively short-range nature of the anion-anion repulsion, this interaction is undoubtedly quite small. For simplicity, we neglect this term:

$$\phi_r = 0 \quad . \tag{II-4}$$

Its deletion makes no drastic difference in the bending potential curves or their interpretation.

C. Derivation of the Electrostatic Potential Energy of the System

Using the approach of Klemperer et al.,[6] we replace the ions of the molecule MX_2 by an assembly of three spherical conductors carrying the appropriate charges and having radii corresponding to the cube root of the dipole polarizabilities of the ions involved (see bottom drawing on page 6). For consistency and rigor, a complete multipole expansion of the electrostatic potential energy ϕ_{ei} must be calculated.

Previous experience has shown that such a complete multipole expansion often diverges if the free ion polarizability values are used.[15] The problem of assigning reasonable values to polarizabilities of various ions within molecules has long troubled both experimentalists and theoreticians.[23] For the alkali halides, the dipole polarizabilities are effectively reduced from the free ion value by both a penetration effect of one ion into another,[24,25] and an environmental effect due to the repulsion of another polarized ion.[23] The penetration effect is most pronounced for small ions, while the environmental effect is most evident for large ions. Together, they constitute an approximately constant reduction in the dipole polarizability value. For quadrupole polarizabilities, these effects are only more pronounced.

Using this same approach for the alkaline earth dihalides, we can resolve both of the first two dilemmas mentioned in the Introduction to

this chapter: The drastically reduced higher multipole polarizabilities allow us to neglect any terms involving multipoles higher than quadrupole. Even the positive charge-negative induced quadrupole terms are suppressed. Moreover, using the reduced polarizabilities, the positive charge-negative induced dipole terms are approximately compensated for by the charge-dipole and charge-quadrupole terms between negative ions. These terms are neglected for simplicity. Thus, reasonable convergence is achieved by including:

1. Charge-charge interactions (3)
   - Positive charge-negative charge (2)
   - Negative charge-negative charge (1)
2. Negative charge-positive induced dipole interactions (2)
3. Negative charge-positive induced quadrupole interactions (2)

A schematic summary of the lower order multipole interactions and their status in the current calculations is given in Fig. II-1.

Since no negative multipole terms remain at this point, the anions can be replaced by point charges, and the problem reduces to the situation as drawn (top) on page 12. The electrostatic energy of this system can be obtained in a closed-form expression whose expansion yields the individual charge-multipole contributions. In turn, the resulting series can be rewritten in a form giving $\underline{\phi_{ei}}$ in terms of the arbitrary isotropic multipole polarizabilities of the cation.[6] For a spherical conductor, the required substitutions are

$$\alpha_D = a^3$$

$$\alpha_Q = a^5 \quad ,$$

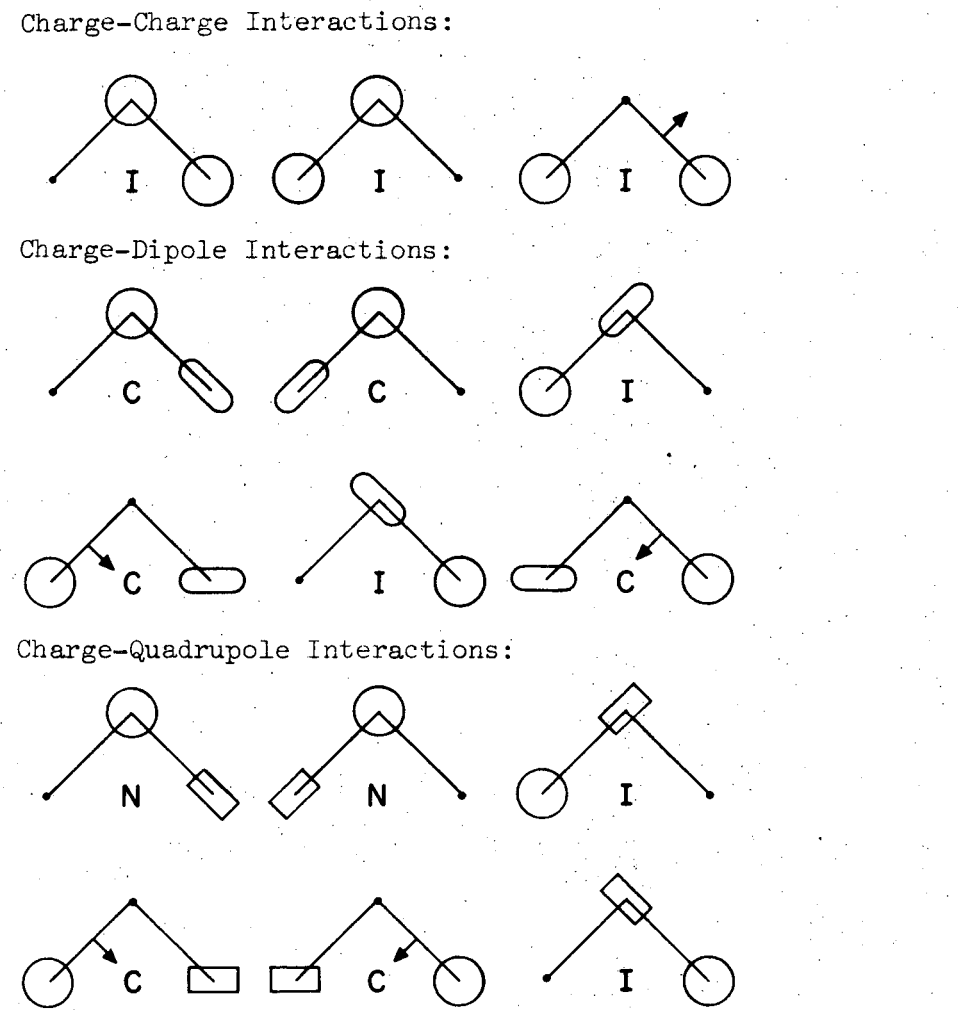

: Charge

: Dipole, induced in the elongated direction

: Quadrupole, induced in the elongated direction

→ : Direction in which force tends to move bond

I : Interaction included in model

C : Interaction compensated for by other interaction(s)

N : Interaction neglected

XBL735-2869

Fig. II-1. Lower order multipole interactions.

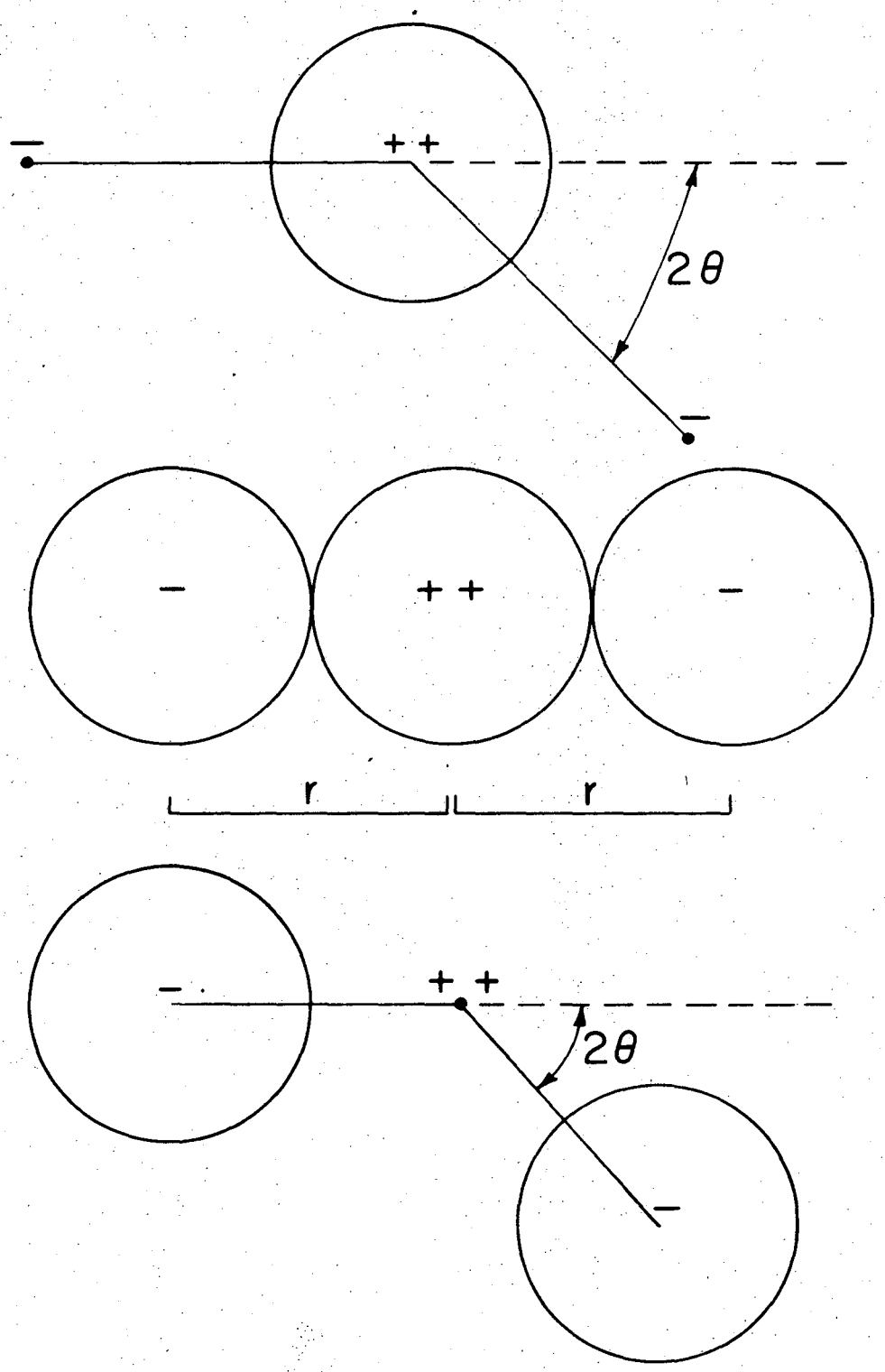

XBL735-2870

so that

$$\alpha_Q = \alpha_D^{5/3} \quad . \tag{II-5}$$

Using the method of images,[26] we derive an explicit form for the electrostatic potential energy of this system. Consider two equivalent point charges each carrying a negative charge $-e$, and each located at a distance d from the center of a spherical conductor of radius a and charge $+2e$. The angle between the bonds is $(180° - 2\theta = 2\alpha)$. To take account of the polarization of the conductor by the negative point charges, we replace the conductor by the image charges q_a' and the image charge q_b', both at distances a^2/d from the charge q_c at the conductor's center. A detailed schematic of this "image" system appears in Fig. II-2.

The potential energy of a system of charges and charged conductors is given by[27]

$$\phi_{ei} = \frac{1}{2} \sum_i q_i U_i \quad , \tag{II-6a}$$

where U_i is the potential at the location of the charge q_i. For our "image" system, we obtain:

$$\phi_{ei} = \frac{1}{2}(q_a U_a + q_b U_b + q_c U_c)$$

$$= \frac{1}{2}((-e)U_a + (-e)U_b + (+2e)U_c) \quad , \tag{II-6b}$$

where U_a is the potential at point charge A, U_b the potential at point charge B, and U_c the potential at the surface of the spherical conductor.

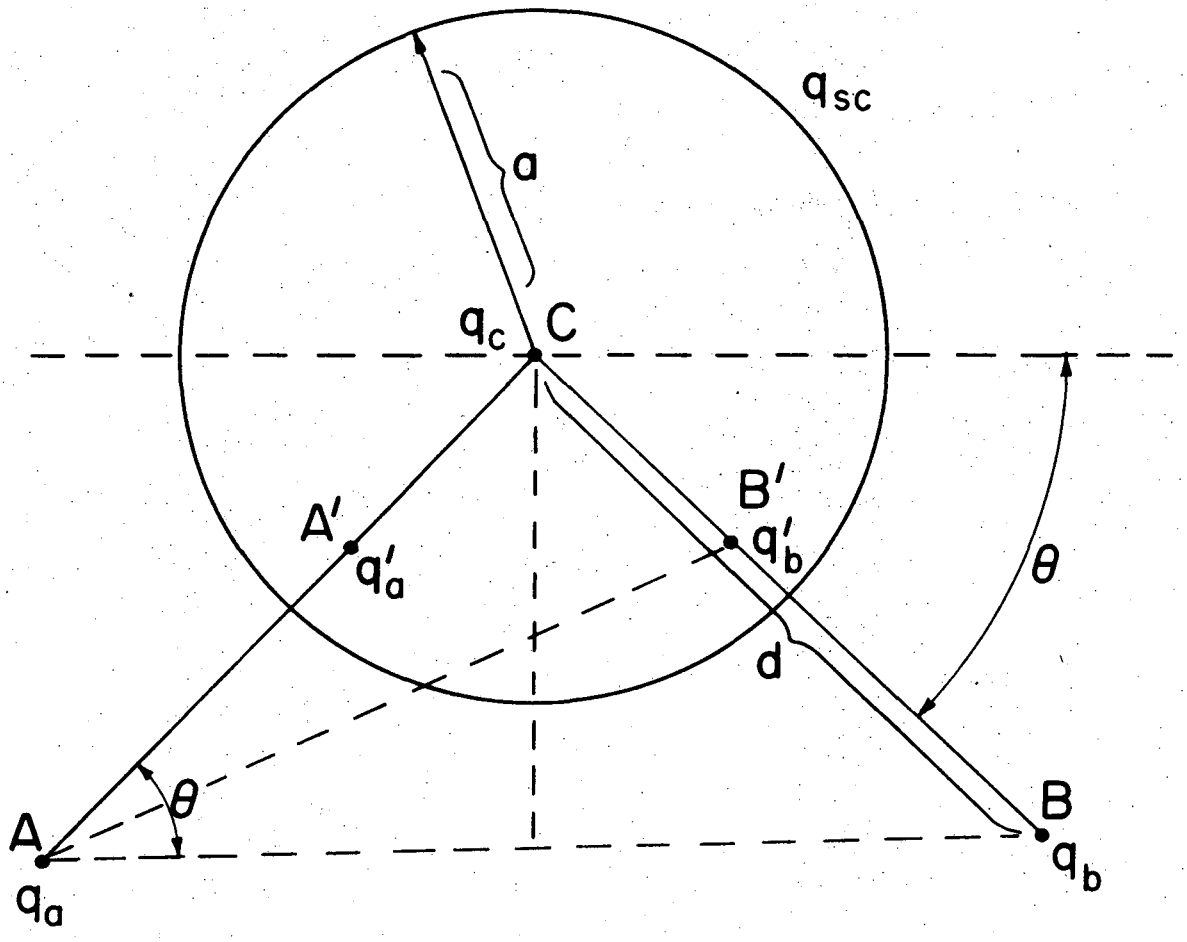

XBL735-2868

Fig. II-2. Image Charge System for MX_2 molecules (Polarized Cation).

Charges:

$$q_a = q_b = -e$$
$$q_{sc} = +2e$$
$$q'_a = q'_b = ea/d$$
$$q_c = +2e - 2(ea/d)$$
$$= +2e(1 - \frac{a}{d})$$

Distances:

$$\overline{AB} = 2d \cos \theta$$
$$\overline{CA'} = \overline{CB'} = a^2/d$$
$$\overline{AA'} = \overline{BB'} = d - (a^2/d)$$
$$\overline{AB'} = \overline{BA'}$$
$$= d(1 + \frac{a^4}{d^4} + \frac{2a^2 \cos 2\theta}{d^2})^{1/2}$$

The definition of the potential[28] due to a collection of point charges at distances d_i is:

$$U = \sum_i q_i/d_i \quad . \tag{II-7}$$

The potential U_c is due to the charge q_c alone since the potentials due to a point charge and its image cancel at the surface of the spherical conductor:

$$U_c = \frac{q_c}{a} = \frac{2e(1 - \frac{a}{d})}{a} = 2e/a - 2e/d \quad , \tag{II-8}$$

where the value of q_c given in Fig. II-2 has been substituted into Eq. (II-8).

Since A and B are equivalent, so are U_a and U_b. The expression for U_a is derived by summing the potential terms due to q'_a, q'_b, q_b and q_c:

$$U_a = \frac{q'_a}{(d - \frac{a^2}{d})} + \frac{q_b}{2d\cos\theta} + \frac{q'_b}{(\overline{AB'})} + \frac{q_c}{d}$$

$$= \frac{ea/d}{(d - \frac{a^2}{d})} - \frac{e}{2d\cos\theta} + \frac{ea/d}{(\overline{AB'})} + \frac{2e(1 - \frac{a}{d})}{d} \quad , \tag{II-9}$$

where the values of the point charges have been substituted into Eq. (II-9) from Fig. II-2. $\overline{AB'}$ is the distance from A to B' in Fig. II-2. To evaluate $\overline{AB'}$ we use the cosine law ($X^2 = Y^2 + Z^2 - 2YZ\cos X$) and the trignometric identity, $\cos(180° - 2X) = -\cos 2X$. Thus, from Fig. II-2

$$(\overline{AB'})^2 = (d)^2 + (a^2/d)^2 - 2(d)(a^2/d)\cos(180° - 2\theta)$$

$$= d^2(1 + \frac{a^4}{d^4} + \frac{2a^2}{d^2}\cos 2\theta) \qquad \text{(II-10a)}$$

and

$$(\overline{AB'}) = d(1 + \frac{a^4}{d^4} + \frac{2a^2}{d^2}\cos 2\theta)^{\frac{1}{2}} \quad . \qquad \text{(II-10b)}$$

Substituting Eq. (II-10b) into Eq. (II-9):

$$U_a = \frac{ea}{d^2(1 - \frac{a^2}{d^2})} - \frac{e}{2d\cos\theta} + \frac{ea}{d^2}(1 + \frac{a^4}{d^4} + \frac{2a^2}{d^2}\cos 2\theta)^{-\frac{1}{2}} + \frac{2e}{d} - \frac{2ea}{d^2}$$

$$= \frac{e}{d}(2 - \frac{1}{2\cos\theta}) + \frac{ea}{d^2}[-2 + (1 - \frac{a^2}{d^2})^{-1} + (1 + \frac{a^4}{d^4} + \frac{2a^2}{d^2}\cos\theta)^{-\frac{1}{2}}] \quad .$$

(II-11)

To simplify this expression, we expand $(1 - \frac{a^2}{d^2})^{-1}$ as the binomial series $(1 + x)^{-1}$ with $x = -\frac{a^2}{d^2}$, and obtain

$$(1 - \frac{a^2}{d^2})^{-1} = 1 + \frac{a^2}{d^2} + \frac{a^4}{d^4} + \ldots$$

Similarly, expanding $(1 + \frac{a^4}{d^4} + \frac{2a^2}{d^2}\cos 2\theta)^{-\frac{1}{2}}$ as $(1 + x)^{-\frac{1}{2}}$ with $x = \frac{a^4}{d^4} + \frac{2a^2}{d^2}\cos 2\theta$, we obtain

$$\left(1 + \frac{a^4}{d^4} + \frac{2a^2}{d^2}\cos 2\theta\right)^{-\frac{1}{2}} = 1 - \frac{a^2}{d^2}\cos 2\theta - \frac{a^4}{2d^4} + \frac{3a^4}{2d^4}\cos^2 2\theta$$

$$+ \frac{3a^6}{2d^6}\cos 2\theta + \frac{3a^8}{8d^8} + \ldots$$

where henceforth only terms up to a^5 will be retained. (The validity of these binomial series expansions rests on the assumption that $\underline{a} < \underline{d}$.) Substituting these expressions into Eq. (II-11), we derive:

$$U_a = \frac{e}{d}\left(2 - \frac{1}{2\cos\theta}\right) + \frac{ea}{d^2}\left[-2 + \left(1 + \frac{a^2}{d^2} + \frac{a^4}{d^4} + \ldots\right)\right.$$

$$\left. + \left(1 - \frac{a^2}{d^2}\cos 2\theta - \frac{a^4}{2d^4} + \frac{3a^4}{2d^4}\cos^2 2\theta + \ldots\right)\right]$$

$$U_a = \frac{2e}{d} - \frac{e}{2d\cos\theta} - \frac{2ea}{d^2} + \frac{ea}{d^2} + \frac{ea^3}{d^4} + \frac{ea^5}{d^6} + \frac{ea}{d^2} +$$

$$- \frac{ea^3}{d^4}\cos 2\theta - \frac{ea^5}{2d^6} + \frac{3ea^5}{2d^6}\cos^2 2\theta$$

$$= \frac{e}{d}\left(2 - \frac{1}{2\cos\theta}\right) + \frac{ea^3}{d^4}(1 - \cos 2\theta) + \frac{ea^5}{d^6}\left(\frac{1}{2} + \frac{3}{2}\cos^2 2\theta\right) \quad . \tag{II-12}$$

Thus, the electrostatic interaction can be determined from Eq. (II-6b), using Eqs. (II-8) and (II-12):

$$\phi_{ei} = -eU_a + eU_c$$

$$= -\frac{e^2}{d}\left[\left(2 - \frac{1}{2\cos\theta}\right) + \frac{a^3}{d^3}(1 - \cos 2\theta)\right.$$

$$\left. + \frac{a^5}{d^5}\left(\frac{1}{2} + \frac{3}{2}\cos^2 2\theta\right)\right] + \frac{e^2}{d}\left(\frac{2d}{a} - 2\right)$$

$$= \frac{2e^2}{a} - \frac{e^2}{d}\left[\left(4 - \frac{1}{2\cos\theta}\right) + \frac{a^3}{d^3}(1 - \cos 2\theta)\right.$$

$$\left. + \frac{a^5}{d^5}\left(\frac{1}{2} + \frac{3}{2}\cos^2 2\theta\right)\right] \quad . \qquad \text{(II-13a)}$$

The initial constant term $2e^2/a$ will be neglected subsequently since we are only interested in <u>relative</u> energy determinations. Thus, the spherical conductor potential energy reduces to

$$\phi_{ei} = -\frac{e^2}{d}\left[\underbrace{\left(4 - \frac{1}{2\cos\theta}\right)}_{\text{charge-charge}} + \underbrace{\frac{\alpha_D}{d^3}(1 - \cos 2\theta)}_{\text{charge-dipole}}\right.$$

$$\left. + \underbrace{\frac{\alpha_Q}{d^5}\left(\frac{1}{2} + \frac{3}{2}\cos^2 2\theta\right)}_{\text{charge-quadrupole}}\right] \quad , \qquad \text{(II-13b)}$$

where the expression has been generalized through the introduction of the cationic polarizabilities.

As can readily be seen, Eq. (II-13b) is a summation of the three basic types of interactions. Using the trignometric identities

$$\cos 2\theta = 1 - 2 \sin^2\theta$$

and

$$\cos^2 2\theta = 1 - 4 \sin^2\theta + 4 \sin^4\theta \quad ,$$

Eq. (II-13b) can be rewritten as the following:

$$\phi_{ei} = - \frac{e^2}{d} [4 - \frac{1}{2 \cos\theta} + \frac{\alpha_D}{d^3}(2 \sin^2\theta)$$

$$+ \frac{\alpha_Q}{d^5}(2 - 6 \sin^2\theta + 6 \sin^4\theta)] \quad . \qquad \text{(II-13c)}$$

In order to simulate the molecule, the parameter $\underline{d}$ in the expression above must be replaced by the effective internuclear distance $\underline{r}$, as given in Eq. (II-2). Since $k \sin^2\theta << 1$ (i.e., the contraction of $\underline{r}$ is small), we can expand the terms involving $(1/r)$ using the binomial series

$$\frac{1}{r} = \frac{1}{\ell(1 - k \sin^2\theta)} \sim \frac{1}{\ell}(1 + k \sin^2\theta) \quad ,$$

where only the first two series terms are retained.

Similarly:

$$\frac{1}{r^4} \sim \frac{1}{\ell^4}(1 + 4k \sin^2\theta)$$

and

$$\frac{1}{r^6} \sim \frac{1}{\ell^6}(1 + 6k \sin^2\theta) \quad .$$

Substituting these expressions into Eq. (II-13c), we obtain, after collecting terms,

$$\phi_{ei} = \frac{e^2}{\ell} [(4 + 4k \sin^2\theta) - (\frac{1}{2 \cos\theta} + \frac{k \sin^2\theta}{2 \cos\theta})$$

$$+ \frac{\alpha_D}{\ell^3}(2 \sin^2\theta + 8k \sin^4\theta) + \frac{\alpha_Q}{\ell^5} \{2 + (12k - 6)\sin^2\theta$$

$$+ (6 - 36k)\sin^4\theta + 36k \sin^6\theta\}] \quad . \qquad \text{(II-13d)}$$

D. Calculation of the Bending Potential Energy Curves

By addition of Eqs. (II-13d) and (II-4) we obtain the total potential energy of the system:

$$V = \phi_{ei} + \phi_r = \phi_{ei}$$

We developed a computer program (see Appendix A-1a) to generate these potential energy curves for a preset selection of bending angles. Not only is the total potential energy calculated for each angle, but also the individual contributions of the repulsion term, charge-charge term, charge-dipole term, and charge-quadrupole term are given.

The only input data (other than fundamental constants) necessary for calculation of the alkaline earth dihalide curves are

ℓ = equilibrium internuclear distance

α_D = cationic dipole polarizability

α_Q = cationic quadrupole polarizability

k = deformation constant

The bond lengths ℓ given in Table II-1 come from the electron diffraction work of Akishin and co-workers.[29,30] The dipole polarizabilities listed in Table II-1 are derived from Edlen's spectroscopic data[31] or from Pauling's crystal refractivity data.[32] The quadrupole polarizabilities are derived in turn from these dipole polarizabilities using Eq. (II-5). As is explained in Chapter VI, according to experimental data strontium chloride ($SrCl_2$) is bent, while strontium bromide ($SrBr_2$) is linear. To obtain appropriate bending potential curves for these two molecules, the proportionality constant h equals approximately 0.172. Then, the deformation constant k is determined using Eq. (II-3).

A complete compilation of the alkaline earth dihalide bending potential curves appears in Appendix A-2. A summary of the predicted gas phase geometries of these molecules is given in Table II-2. Table II-3 compares the bending angle (defined here as $2\alpha \equiv 180° - 2\theta$) calculated in this work with experimental values from infrared absorption spectroscopy. The agreement is good.

E. Physical Constants Derived from the Model

To obtain the energy levels, force constants, and bending frequencies for these molecules, it is necessary to solve the Schröedinger equation using the above potential energy function, V.

$$\mathcal{H}\Psi = E\Psi$$

or

$$-\frac{\hbar^2}{2\mu}\nabla^2\Psi + V\Psi = E\Psi \quad , \qquad \text{(II-14)}$$

Table II-1. Model Input Data for the Alkaline Earth Dihalides

Compound (MX_2)	Equilibrium Internuclear Distance (ℓ)[a]	Deformation Constant (k)[b]	Dipole Polarizability of Metal (α_D)[c,d]	Quadrupole Polarizability of Metal (α_Q)[e]
BeF_2	1.40 Å	0.0241	0.00767 Å^3 (0.0079)	0.000299 Å^5
$BeCl_2$	1.75	0.0193		
$BeBr_2$	1.91	0.0177		
BeI_2	2.10	0.0161		
MgF_2	1.77	0.0398	0.0696 (0.094)	0.0118
$MgCl_2$	2.18	0.0323		
$MgBr_2$	2.34	0.0301		
MgI_2	2.52	0.0280		
CaF_2	2.10	0.0644	0.490 (0.47)	0.305
$CaCl_2$	2.51	0.0539		
$CaBr_2$	2.67	0.0506		
CaI_2	2.88	0.0470		
SrF_2	2.20	0.0743	0.866 (0.86)	0.787
$SrCl_2$	2.67	0.0612		
$SrBr_2$	2.82	0.0580		
SrI_2	3.03	0.0540		

(continued)

Table II-1 (continued)

Compound (MX_2)	Equilibrium Internuclear Distance (ℓ)[a]	Deformation Constant (k)[b]	Dipole Polarizability of Metal (α_D)[c,d]	Quadrupole Polarizability of Metal (α_Q)[e]
BaF_2	2.32	0.0843	1.48 (1.56)	1.922
$BaCl_2$	2.82	0.0694		
$BaBr_2$	2.99	0.0654		
BaI_2	3.20	0.0611		

[a]See Refs. 29 and 30.

[b]Values calculated using Eq. (II-3).

[c]Values used taken from Edlén's spectroscopic data (see Ref. 31).

[d]Values given in parentheses taken from Pauling's data (see Ref. 32).

[e]Values calculated using Eq. (II-5).

Table II-2. Predicted Alkaline Earth Dihalide Geometries

BeF_2	$BeCl_2$	$BeBr_2$	BeI_2
MgF_2	$MgCl_2$	$MgBr_2$	MgI_2
CaF_2	$CaCl_2$	$CaBr_2$	CaI_2
SrF_2	$SrCl_2$	$SrBr_2$	SrI_2
BaF_2	$BaCl_2$	$BaBr_2$	BaI_2

= bent molecule

= linear molecule

Table II-3. Bending Angles for the Alkaline Earth Dihalides

Compound	Bending Angle* (Theory-Polarizable Ion Model)	Bending Angle* (Experimental)
BeF_2	180°	180°[a,b,c]
$BeCl_2$	180	180[a,b,c]
$BeBr_2$	180	180[a]
BeI_2	180	180[a]
MgF_2	180	180[b],158[d],150-155[e]
$MgCl_2$	180	180°[c,f]
$MgBr_2$	180	180[f]
MgI_2	180	
CaF_2	140	140[d]
$CaCl_2$	180	180[g]
$CaBr_2$	180	
CaI_2	180	
SrF_2	120	108[d]
$SrCl_2$	148	130[h]
$SrBr_2$	164	
SrI_2	180	
BaF_2	104	100[d]
$BaCl_2$	128	120[h],< 135[i]
$BaBr_2$	136	
BaI_2	150	

(continued)

Table II-3 (continued)

*All angles are converted to list the smaller X-M-X angle.

[a]See Ref. 33.

[b]See Ref. 34.

[c]See Ref. 35.

[d]See Ref. 36.

[e]See Ref. 37.

[f]See Ref. 38.

[g]See Ref. 39.

[h]See Ref. 40.

[i]See Ref. 41.

where $\mathcal{H}$ is the system Hamiltonian, E the system energy, Ψ the wavefunction, $\hbar$ Planck's constant, μ the reduced mass of the system, and ∇ the del operator. Obviously, no exact solution to the above equation is possible using our complex potential energy expression. Therefore, we resort to perturbation theory. As a first approximation to the calculated potential energy function, we chose a two-dimensional cylindrical potential well:

$$V'(y,z) = 0 \quad \text{for} \quad y^2 + z^2 < \ell^2 \qquad \text{(II-15a)}$$

$$V'(y,z) = \infty \quad \text{for} \quad y^2 + z^2 > \ell^2 \qquad \text{(II-15b)}$$

This type of potential energy function has been shown to be physically reasonable by Barrow.[42] Using Eqs. (II-15a) and (II-15b), the solutions of the Schröedinger equation are spherical Bessel functions of order m. The complete solution to the problem is given in Appendix A-3a. Using existing library subroutines, we devised a program to calculate the necessary Bessel functions (see Appendix A-1b). This approximation is quite good for linear molecules, but less satisfactory for the bent molecules where the central hump is neglected. Figure II-3 illustrates this point.

A better fit to the calculated potential energy curves is achieved using a harmonic potential curve with a Gaussian perturbation hump:

$$V' = \frac{1}{2} k_b x^2 + H \exp(-\Lambda x^2) \quad , \qquad \text{(II-15c)}$$

where k_b is the bending force constant, x a displacement coordinate ($x = r\theta$), and H and Λ are adjustable constants. A complete mathematical

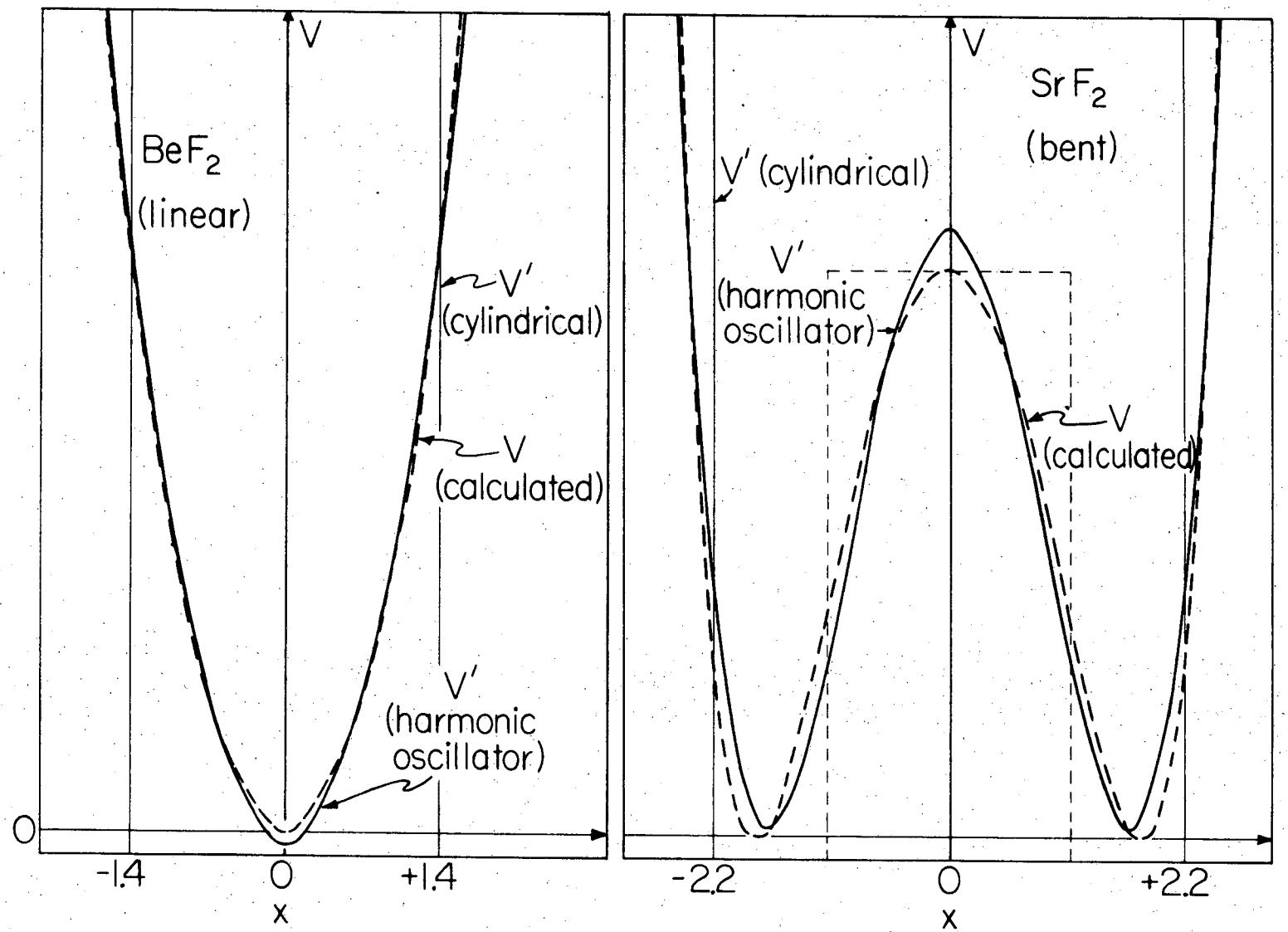

XBL735-2872

Fig. II-3. Comparison of calculated, cylindrical, and harmonic oscillator potential wells for typical bent and linear molecules.

explanation of the use of this form of a potential energy function is given by Shaffer[43] and references therein. Numerous previous attempts[44-46] to apply this concept to describe simple molecules have met with reasonable success. Our solution of the Schröedinger equation using Eq. (II-15c) is given in Appendix A-3b, and closely resembles the treatments described by Dixon[47] and Chan and Stelman.[48] The computer program developed to calculate directly energy levels and bending frequencies is detailed in Appendix A-1c. The resultant bending frequencies for all the alkaline earth dihalides are given in Table II-4 along with the experimental values obtained from infrared absorption spectroscopy.

For linear molecules with reasonably harmonic bending potential curves, the bending frequency is straightforward. However, for very anharmonic bending potential curves the "bending frequency" is more ambiguous. For the sake of comparison with experimental data, we have calculated two specific sets of "bending frequencies" in these cases.

In matrix-isolation infrared absorption studies conducted at very low temperatures, the reported "bending frequency" should correspond to the lowest vibrational transition (ground state to first excited state) since essentially only the ground vibrational state is populated. We have thus used the transition between our calculated energy levels corresponding to the ground state and the first excited vibrational state to determine an appropriate vibrational frequency for comparison to matrix-isolation values. The experimental frequencies are generally higher than our predicted frequencies for these molecules. The effect of the matrix on these very weak bending frequencies is highly uncertain.

Table II-4. Bending Frequencies for the Alkaline Earth Dihalides*

Compound	Bending Frequency (ν_2) Predicted	Experimental
BeF_2	[333.0][a]	345[b] cm^{-1}
		345[c,d]
$BeCl_2$	[176.6][a]	250[d]
		(240)[c]
$BeBr_2$	[140.2][a]	220[d]
BeI_2	[111.5][a]	(175)[d]
MgF_2	167.0	270[c]
		240[e,f]
		165[b]
$MgCl_2$	77.2	
$MgBr_2$	58.8	
MgI_2	49.7	
CaF_2	69.1, 93.6-162.2	162[f]
		120[b]
$CaCl_2$	51.0	122?[g]
$CaBr_2$	37.1	
CaI_2	30.7	
SrF_2	103.6, 88.5-133.9	105[b]
		82[f]
$SrCl_2$	33.6, 45.3-86.8	(60±15)[h]
$SrBr_2$	17.4, 28.7-52.6	
SrI_2	21.5	

(continued)

Table II-4 (continued)

Compound	Bending Frequency (ν_2) Predicted	Experimental
BaF_2	104.8,<u>85.9-130.8</u>	100±10[b] (64)[f]
$BaCl_2$	38.8,<u>43.5-75.5</u>	60[h]
$BaBr_2$	22.7,<u>27.5-61.0</u>	
BaI_2	14.7,<u>20.6-38.5</u>	

[a]The predicted bending frequencies in brackets for the beryllium dihalides are calculated using a deformation constant <u>k</u> equal to <u>zero</u>. Neglecting the deformation constant can be justified on the basis that beryllium ions are relatively very small and, hence, may not deform at all.

[b]See Ref. 49.

[c]See Ref. 34.

[d]See Ref. 33.

[e]See Ref. 37.

[f]See Ref. 36.

[g]See Ref. 39.

[h]See Ref. 40.

*Predicted and experimental bending frequency values which are underlined apply to the vibrational absorption band observed in high temperature infrared spectroscopic data. Where two predicted values are listed, the single number applies to the lowest vibrational transition observed in matrix-isolation infrared spectroscopy. For linear molecules only a single predicted number is listed which corresponds to the true bending frequency $\underline{\nu_2}$.

When infrared absorption studies are conducted on the gas phase of the alkaline earth dihalides, temperatures several hundred degrees in excess of the melting point are not uncommon. In these cases, many excited vibrational states are highly populated and a broad vibrational absorption band is observed[49] corresponding to the numerous vibrational transitions which can occur between these excited states. To simulate these data, vibrational transitions between our calculated energy levels, which are roughly KT above the ground state energy (where K is the Boltzmann constant and T is 1.3 times the melting point temperature), are used to calculate the "bending frequency". As expected, these transitions create a broad band of vibrational absorption frequencies similar to the experimental observations. We assign only a range of frequencies appropriate to the most intense part of the infrared absorption band. In these cases, the agreement with experimental data is quite good.

F. Extension of the Model to Other Triatomics

1. Transition Metal and Group II-b Dihalides

Because of their similarity to the alkaline earth dihalides, certain other metal dihalides presumably can be represented by our polarizable ion model with minor modifications. Specifically, the dihalides of the metals of the first transition series and those of zinc (Zn), cadmium (Cd), and mercury (Hg) lend themselves to this type of description. Due to the paucity of experimental information, we have restricted ourselves to investigating only titanium difluoride (TiF_2) and the difluorides and dichlorides of manganese (Mn), iron (Fe), cobalt (Co), nickel (Ni), and copper (Cu) among the transition metal dihalides.

Two striking differences between the above compounds and analogous alkaline earth dihalides are evident: 1) There is a significant contraction in the equilibrium internuclear distance (ℓ) as the transition series is traversed; and 2) The quadrupole polarizability is proportionally much larger for these metals which have outer d-shell electrons than for the alkaline earths which have none.

Although the gas phase equilibrium internuclear distances are unknown for the metals of the first transition series, values have been extrapolated from solid-state equilibrium internuclear distances for the difluorides and the dichlorides of interest. The contraction mentioned above is directly reflected in these estimates. Since the equilibrium internuclear distance is employed as a variable in our model, there is no difficulty in incorporating the contraction directly.

As was mentioned above, the "filling-in" of the d-shell electrons contributes more to the quadrupole polarizability than to the dipole polarizability of the cation. Since, in our model, the quadrupole polarizability is calculated directly from the dipole polarizability using the spherical conductor model (see Eq. (II-5)), some modification must be made to account for this effect. As a guideline, the only documentation for the ratio (q) of the quadrupole to dipole polarizability for a full d-shell compared to an empty d-shell

$$q = \frac{(\alpha_Q/\alpha_D)_{\text{full d-shell}}}{(\alpha_Q/\alpha_D)_{\text{empty d-shell}}} \qquad \text{(II-16)}$$

gives the value q = 2.2 for the copper (Cu^+): potassium (K^+) case.[50] Thus, a value of q = 2.2 is assigned to the Group II-b metals where the

d-shell is wholly filled. For the transition metals, the value of q is assumed to increase with a linear proportionality to the number of d-shell electrons from the empty d-shell value of q = 1. to the full d-shell value of q = 2.2. Thus,

Cation	No. d-shell Electrons	q
Ti^{++}	2	1.2
Mn^{++}	5	1.6
Fe^{++}	6	1.7
Co^{++}	7	1.8
Ni^{++}	8	2.0
Cu^{++}	9	2.1

These values are employed in two places in our model. The quadrupole polarizability calculated from a spherical conductor is multiplied by the value of q to reflect increased d-shell quadrupole polarizability. Moreover, the deformation constant k is modified by an additional multiplicative factor (2 - q).

$$k \propto (2 - q)$$

Since q = 1. for the alkaline earth dihalides, the deformation constant k remains unchanged for these molecules. However, since q > 1. for the transition metals, the value of k is significantly reduced. For copper and the Group II-b metals q > 2., so the deformation constant becomes negative. Physically, this reduction of the deformation with the increased quadrupole polarizability of the d-shell electrons is indicative of a decreased tendency for the molecule to bend. The "elliptical" central

metal ion becomes more nearly spherical (less deformable) up to q = 2., after which the ellipticity increases though the deformation is perpendicular to the original one.

A complete list of the values of ℓ, k, α_D, α_Q, and q is given in Table II-5, along with the sources of information. All of the transition metal and Group II-b dihalides are predicted to have a linear gas phase geometry from their bending potential curves (see Appendix A-2). A summary of these geometries is given in Table II-6; Table II-7 lists the corresponding bending angles. Table II-8 gives a complete comparison between theoretical and experimental bending frequencies for the transition metal and Group II-b metal dihalides. The predicted values of the bending frequencies of these molecules (especially the Group II-b dihalides) are in good agreement with the literature values — even though the cation polarizabilities are far from precisely known. This in turn increases our confidence in the bending frequencies predicted for the alkaline earth dihalides, where much better input data is available.

2. Europium Dihalides

The solid state equilibrium internuclear distances and the ionic radii of the fluorides of strontium and europium are nearly identical.[‡] Other known chemical properties of europium and its compounds are similar to those exhibited by their strontium analogs. Therefore, it is of interest to use the polarizable ion model to predict the geometries, bending angles, and bending frequencies of the europium dihalides and compare these predictions to experimental data.

[‡] The solid state bond lengths are 2.50 Å and 2.51 Å, respectively, for SrF_2 and EuF_2, while the cationic radii are 1.13 Å and 1.12 Å for Sr^+ and Eu^+, respectively.

Table II-5. Model Input Data for the Metal Dihalides

Compound (MX_2)	Equilibrium Internuclear Distance (ℓ)[a]	Deformation Constant (k)[b]	Dipole Polarizability of Metal (α_D)[c]	Quadrupole Polarizability of Metal (α_Q)[d]	d-Shell Electron Constant of Metal (q)[e]
ZnF_2	1.81 Å	0.0624	0.285 $Å^3$ (0.21)[f]	0.272 $Å^5$	2.0
$ZnCl_2$	2.05	0.0551			
$ZnBr_2$	2.21	0.0511			
ZnI_2	2.38	0.0474			
CdF_2	1.97	0.0896	1.09 (0.400)[g] (0.46)[f]	2.540	2.0
$CdCl_2$	2.21	0.0799			
$CdBr_2$	2.37	0.0745			
CdI_2	2.55	0.0692			
HgF_2	(2.08)[f]	0.0887	1.244 (0.500)[g] (0.55)[f]	3.165 (0.500)[f]	2.0
$HgCl_2$	2.29	0.0806			
$HgBr_2$	2.41	0.0765			
HgI_2	2.59	0.0716			

(continued)

Table II-5 (continued)

Compound (MX_2)	Equilibrium Internuclear Distance (ℓ)[a]	Deformation Constant (k)[b]	Dipole Polarizability of Metal (α_D)[c]	Quadrupole Polarizability of Metal (α_Q)[d]	d-Shell Electron Constant of Metal (q)[e]
TiF_2	(1.99)[h]	0.0544	0.49	0.366	1.2
MnF_2	(1.87)[h]	0.0647	0.36 (0.26)[f]	0.292	1.5
$MnCl_2$	(2.11)[h]	0.0573			
FeF_2	(1.85)[h]	0.0627	0.309 (0.23)[f]	0.243	1.6
$FeCl_2$	(2.09)[h]	0.0555			
CoF_2	(1.81)[h]	0.624	0.285 (0.21)[f]	0.227	1.7
$CoCl_2$	(2.05)[h]	0.0551			
NiF_2	(1.80)[h]	0.0611	0.263 (0.19)[f]	0.217	1.8
$NiCl_2$	(2.04)[h]	0.0539			

(continued)

Table II-5 (continued)

Compound (MX_2)	Equilibrium Internuclear Distance (ℓ)[a]	Deformation Constant (k)[b]	Dipole Polarizability of Metal (α_D)[c]	Quadrupole Polarizability of Metal (α_Q)[d]	d-Shell Electron Constant of Metal (q)[e]
CuF_2	(1.81)[h]	0.0616	0.274	0.240	1.9
$CuCl_2$	(2.05)[h]	0.0544			
EuF_2[i]	2.20	0.0743	0.866	0.787	1.0
$EuCl_2$[i]	2.67	0.0612			
$EuBr_2$[i]	2.82	0.0580			
EuI_2[i]	3.03	0.0540			
GeF_2	(1.95)[h]	0.1070	1.80[j] (1.60)[f]	2.663	1.0
$GeCl_2$	2.22	0.0940			
$GeBr_2$	2.36	0.0884			
GeI_2	2.55	0.0818			
SnF_2	(2.08)[h]	0.1209	3.15[j]	6.768	1.0
$SnCl_2$	2.42	0.1040			
$SnBr_2$	2.55	0.0987			
SnI_2	2.73	0.0921			

(continued)

Table II-5 (continued)

Compound (MX_2)	Equilibrium Internuclear Distance (ℓ)[a]	Deformation Constant (k)[b]	Dipole Polarizability of Metal (α_D)[c]	Quadrupole Polarizability of Metal (α_Q)[d]	d-Shell Electron Constant of Metal (q)[e]
PbF_2	(2.13)[h]	0.1265	3.87[k]	9.537	1.0
$PbCl_2$	2.45	0.1095			
$PbBr_2$	2.60	0.1036			
PbI_2	2.79	0.0966			

[a]See Refs. 29, 30, 51, and 52.

[b]Values calculated using Eq. (II-3).

[c]Values from Ref. 32 for Group II-b metals.
Values for transition metals extrapolated from zinc value using spherical conductor model.

[d]Values calculated using Eq. (II-5).

[e]Values from relationship $q = 1.0 + \left(\frac{\text{no. d-shell electrons}}{10.}\right)1.2$, if d-shell partially or wholly occupied; $q = 1.0$, otherwise.

[f]Estimated values.

[g]Estimated values based on Ref. 14.

[h]Estimated values based on essentially constant ratio of solid state to gas phase equilibrium internuclear distance (=1.1574) for metal dihalides known.

(continued)

Table II-5 (continued)

[i]Estimated values for all europium dihalide constants equal to similar values for strontium dihalides. This assumption based on nearly equivalent values for known solid state internuclear distances and ionic radii for the two cases.

[j]Estimated values based on value of lead ion using spherical conductor model.

[k]See Ref. 53.

Table II-6. Predicted Metal Dihalide Geometries

ZnF_2	$ZnCl_2$	$ZnBr_2$	ZnI_2
CdF_2	$CdCl_2$	$CdBr_2$	CdI_2
HgF_2	$HgCl_2$	$HgBr_2$	HgI_2
TiF_2			
MnF_2	$MnCl_2$		
FeF_2	$FeCl_2$		
CoF_2	$CoCl_2$		
NiF_2	$NiCl_2$		
CuF_2	$CuCl_2$		
EuF_2	$EuCl_2$	$EuBr_2$	EuI_2
GeF_2	$GeCl_2$	$GeBr_2$	GeI_2
SnF_2	$SnCl_2$	$SnBr_2$	SnI_2
PbF_2	$PbCl_2$	$PbBr_2$	PbI_2

= bent molecule

= linear molecule

Table II-7. Bending Angles for the Metal Dihalides

Compound	Bending Angle* (Theory-Polarizable Ion Model)	Bending Angle* (Experimental)
ZnF_2	180	160-170°[a],180°[b]
$ZnCl_2$	180	180[b]
$ZnBr_2$	180	180[b]
ZnI_2	180	180[b]
CdF_2	180	180[c]
$CdCl_2$	180	180[c]
$CdBr_2$	180	180[c]
CdI_2	180	180[c]
HgF_2	180	180[c]
$HgCl_2$	180	180[c]
$HgBr_2$	180	180[c]
HgI_2	180	180[c]
TiF_2	170	130[d]
MnF_2	180	
$MnCl_2$	180	180[e]
FeF_2	180	180±8[f]
$FeCl_2$	180	180[e]
CoF_2	180	
$CoCl_2$	180	180[e]
NiF_2	180	154-167[a],165±8[f]
$NiCl_2$	180	180[e],150[g]

(continued)

Table II-7 (continued)

Compound	Bending Angle* (Theory-Polarizable Ion Model)	Bending Angle* (Experimental)
CuF_2	180	163-170[a]
$CuCl_2$	180	
EuF_2	120	110±15[h,i]
$EuCl_2$	148	130±10[h,i]
$EuBr_2$	164	
EuI_2	180	
GeF_2	82	95±2[f],94±4[j]
$GeCl_2$	88	
$GeBr_2$	96	
GeI_2	108	
SnF_2	66	
$SnCl_2$	72	
$SnBr_2$	80	
SnI_2	92	
PbF_2	62	
$PbCl_2$	68	96±3[h]
$PbBr_2$	76	
PbI_2	84	

*All angles are converted to list the smaller X-M-X angle.

[a]See Ref. 54.

[b]See Ref. 55.

[c]See Ref. 56.

[d]See Ref. 57.

[e]See Ref. 58.

[f]See Ref. 59.

[g]See Ref. 39.

[h]See Ref. 40.

[i]See Ref. 60.

[j]See Ref. 61.

Table II-8. Bending Frequencies for the Metal Dihalides*

Compound	Bending Frequency (ν_2) Predicted	Experimental
ZnF_2	150.6	150.5[a] cm^{-1}
		157±30[b]
$ZnCl_2$	99.2	102[a]
$ZnBr_2$	62.9	74[a]
ZnI_2	49.4	62[a]
CdF_2	174.4	123[c]
$CdCl_2$	95.4	88.5[c]
$CdBr_2$	57.9	62[c]
CdI_2	42.3	(50.5)[c]
HgF_2	156.7	171.5[c]
$HgCl_2$	89.2	107[c],70[d],73[e,f]
$HgBr_2$	54.8	73[c],41[d],53[f]
HgI_2	38.6	63[c],33[d],46[f]
TiF_2	90.5,164.8-189.3	180±8[g]
MnF_2	103.3	125-132[h]
$MnCl_2$	69.9	83[i]
FeF_2	114.6	141-149[h]
$FeCl_2$	75.4	88[i]
CoF_2	125.4	151-158[h],(151±30)[b]
$CoCl_2$	84.2	94.5[i]
NiF_2	139.5	140-143[h],(142±30)[b]
$NiCl_2$	90.1	85[i]

(continued)

Table II-8 (continued)

Compound	Bending Frequency (ν_2) Predicted	Experimental
CuF_2	144.3	183-188[h],(155±30)[b]
$CuCl_2$	91.6	
EuF_2	101.5,<u>89.5-128.6</u>	114±5[j]
$EuCl_2$	38.4,<u>42.1-82.9</u>	64±10[j]
$EuBr_2$	18.1,<u>27.2-58.7</u>	
EuI_2	19.8	

[a]See Ref. 55.

[b]See Ref. 54.

[c]See Ref. 56.

[d]See Ref. 62.

[e]See Ref. 63.

[f]See Ref. 64.

[g]See Ref. 57.

[h]See Ref. 59.

[i]See Ref. 58.

[j]See Ref. 40.

*Predicted and experimental bending frequency values which are underlined apply to the vibrational absorption band observed in high temperature infrared spectroscopic data. Where two predicted values are listed, the single number applies to the lowest vibrational transition observed in matrix-isolation infrared spectroscopy. For linear molecules only a single predicted number is listed which corresponds to the true bending frequency $\underline{\nu_2}$. Values in parentheses are estimated.

Since no experimental data is available on the gas phase equilibrium internuclear distances and dipole polarizabilities, the values of these parameters for the europium compounds are taken to be identical with those of their strontium analogs (see Tables II-1 and II-5). The metal quadrupole polarizabilities are calculated from the dipole polarizabilities using the spherical conductor model.

Similarly to the strontium compounds, the bending potential curves (see Appendix A-2) indicate a bent geometry for EuF_2 and $EuCl_2$, and a linear geometry for $EuBr_2$ and EuI_2. Table II-6 gives a summary of these predictions. The predicted values of the bending angles and bending frequencies appear in Table II-7 and II-8. In the limited cases where prior experimental data are available, agreement with predicted values seems quite good.

3. Group IV-a Dihalides

By stretching a point, the polarizable ion model can be applied to the Group IV-a dihalides of germanium (Ge), tin (Sn), and lead (Pb). The metal dipole and quadrupole polarizabilities are extrapolated from a known solid state lead value[53] using the spherical conductor model. The internuclear distance values for the difluorides of these molecules are extrapolated from the electron diffraction data[29,30,51,52] for the other dihalides of these molecules (see Table II-5).

Since the bonding in the Group IV-a dihalides is not appreciably ionic (especially for the germanium compounds), any predictions of our polarizable ion model must be viewed with some skepticism. All of these molecules are predicted to be strongly bent (see Appendix A-2); these

results are corroborated by infrared and ultraviolet studies. A summary of the predicted geometries and bending angles appears in Table II-6 and II-7, respectively. No reliance is placed on the bending angles quoted because of the large extrapolations involved therein. For the same reason, no attempt is made to predict bending frequencies for these compounds. Nevertheless, the qualitative trends in the geometries of these molecules seem reasonable.

G. Concluding Remarks

Since any polarizable ion model is indeed just a model of the actual quantum mechanical situation, the validity of the model depends on the accuracy of the approximations inherent in it. The most crucial approximation in our polarizable ion model is that the bonding within these molecules is "ionic". Certainly, this approximation can be justified for the alkali halides. In general, the alkaline earth dihalides and the europium dihalides compare quite favorably with the alkali halides with respect to "ionic-type" bonding. Our polarizable ion model is a good representation of this bonding. The other metal dihalides described are less ionic; consequently, ionic model predictions for these molecules must be viewed with a greater degree of skepticism. The Group IV-a dihalides are an extreme case in point. On the whole, the predictions of our ionic model are even more accurate than one could expect using the "ionic-bonding" criterion.

The input data required for the polarizable ion model calculations place restrictions on the molecules which can be described. Where the data is incomplete, we have tried to make intelligent estimates of these

quantities from known information. Where the data is contradictory, as with many of the metal dipole polarizabilities, we have tried to chose the most accurate values.

Recent publications add measurably to the input data necessary for future polarizable ion model calculations. Among these are papers listing the ionic radii of all elements currently appearing in the Periodic Table[65] and certain postulated superheavy elements.[66] Also, recent publication[67] of the dipole polarizabilities of the lanthanide and actinide ions encourages us about the possibility of extending our model to include the appropriate lanthanide and actinide dihalides.

Undoubtedly, our model makes over-simplifications of some terms such as the repulsion energy and the polarizability functionalities. However, our polarizable ion model as explained previously gives good agreement with experimentally known data for "ionic" metal dihalides in the gas phase. The predictions of this model await further experimental verification.

III. THE "LINEAR" POLARIZABLE ION MODEL

A. Introduction

The polarizable ion model described in Chapter II allows us to predict unknown or uncertain gas phase bending frequencies ν_2. It is also of interest to be able to predict the two stretching frequencies for symmetric triatomics. The symmetric stretching frequency ν_1 of the linear symmetric triatomics is particularly important since it is infrared inactive.[68]

The most important parameter of the system is the internuclear bond length r for stretching interactions (as contrasted to the bending angle's importance for bending frequencies). At equilibrium, the net force on each of the internuclear bonds must vanish:

$$\sum_i F_i = 0 \qquad \text{(III-1)}$$

B. Construction of the Model

The basis of the "linear" polarizable ion model for gas phase metal dihalides is three ions arranged as appears in the middle drawing on page 12. In considering the stretching interactions, the polarization of the halide ions is more important than that of the metal cation. Thus, the polarization of the central metal ion will be neglected for simplicity. The problem then reduces to the situation shown in the bottom drawing on page 12. Each of the halide ions is assigned a dipole polarizability (β_D). Higher multipole polarizabilities on these ions are neglected for simplicity. Only three types of electrostatic interactions are considered:

1. Charge-charge interactions (3)

   Positive-negative (2)

   Negative-negative (1)

2. Negative charge-negative induced dipole interaction (1)

3. Positive charge-negative induced dipole interactions (2)

The electrostatic potential energy of this system can be obtained directly in a closed-form expression.

C. Derivation of the Repulsion Interaction Energy

A repulsion interaction term (between the negative and the positive ions) must be included for stability. The present treatment employs the best single term empirical representation[7] for this interaction,

$$\phi_r = A\, r^n \exp(-r/\rho) \quad , \qquad \text{(III-2)}$$

where n is a constant for a given halide ligand. For the alkali halides the repulsion constants A and ρ are determined directly by the use of the familiar relationships,

$$(\partial V/\partial r)_{r=\ell} = 0. \quad , \qquad \text{(III-3)}$$

and

$$(\partial^2 V/\partial r^2)_{r=\ell} = k_b \qquad \text{(III-4)}$$

where k_b can be determined experimentally. For the alkali halides, the decay constant ρ depends mainly on the size of the anion, but does show a small linear variation with the cation to anion size ratio. To obtain ρ for the metal-halide repulsion in the alkaline earth dihalides, we extrapolate to the ionic radius (r_+) of that particular metal (see Fig. III-1). The best fitting line for a ρ vs. metal cation plot, from which alkaline earth dihalide model values of ρ are determined, is:

$$\text{for fluorides:} \quad \rho = 0.391 + 0.036(r_+/r_-)\ \text{Å} \qquad \text{(III-5a)}$$

$$\text{for other halides:} \quad \rho = 0.050 + 0.142(r_-) + 0.036(r_+/r_-)\ \text{Å} \ . \qquad \text{(III-5b)}$$

Two separate equations are required because the exponential n equals two for the fluorides and zero for the other halides. This choice of values reflects the best fits obtained using various n in the alkali halide model.[69] The alkali halide equations describing the repulsion constant A's are

$$\text{for fluorides:} \quad A = 150 + 400(r_+)^3\ \text{eV} - \text{Å}^2 \qquad \text{(III-6a)}$$

$$\text{for other halides:} \quad A = 850 + 900(r_+)^3\ \text{eV} \ . \qquad \text{(III-6b)}$$

The corresponding values of the pre-exponential A's for the alkaline earth dihalides are obtained by substituting the appropriate alkaline earth $(r_+)^3$ value into either Eq. (III-6a) or (III-6b), and solving for A (see Fig. III-2). However, the increased charge on the alkaline earth ions (relative to the alkali metal ions) increases the polarization of the

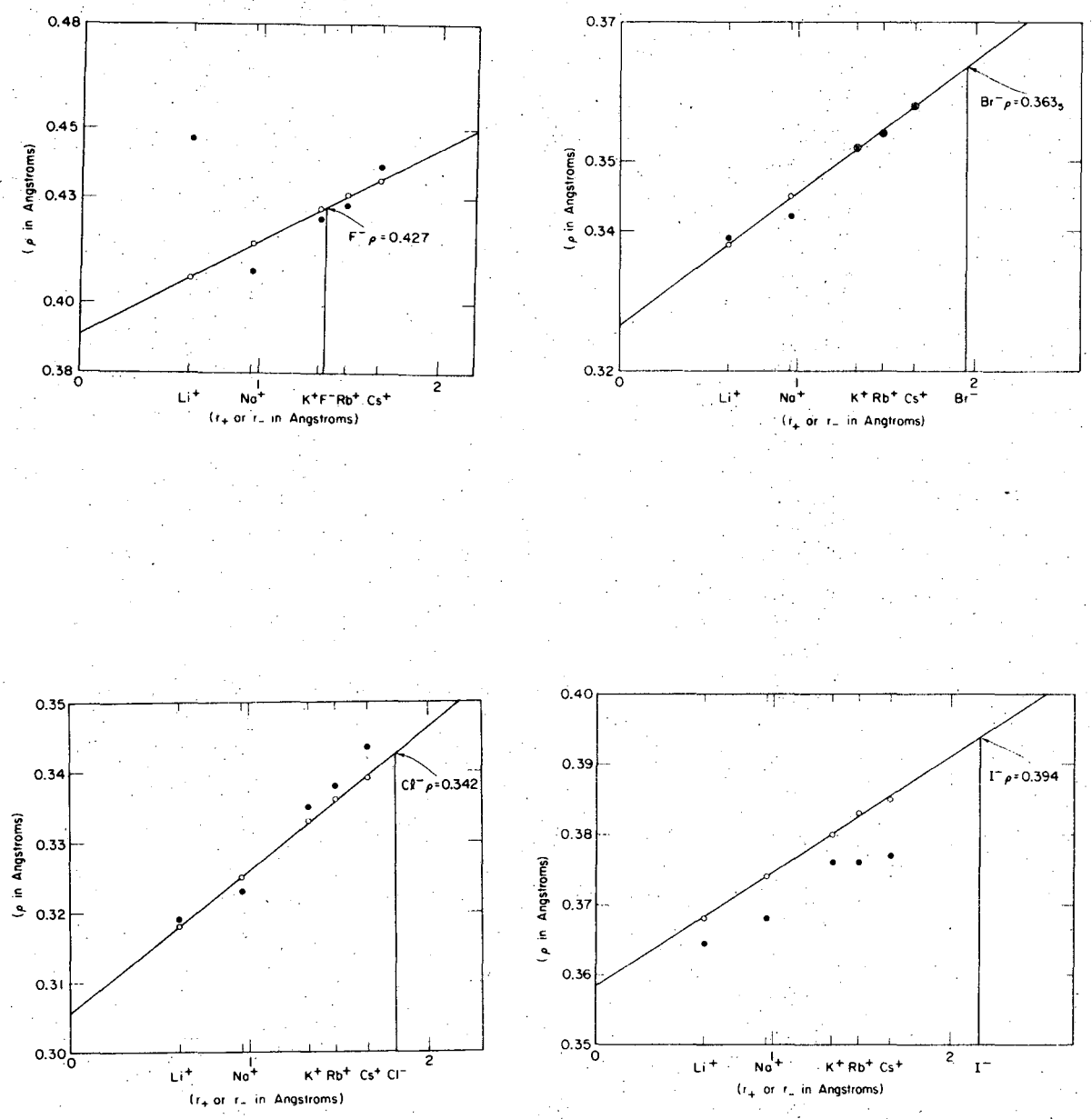

XBL 737-3524A

Fig. III-1. Derivation of the repulsive decay constant $\underline{\rho}$ for the "linear" polarizable ion model.

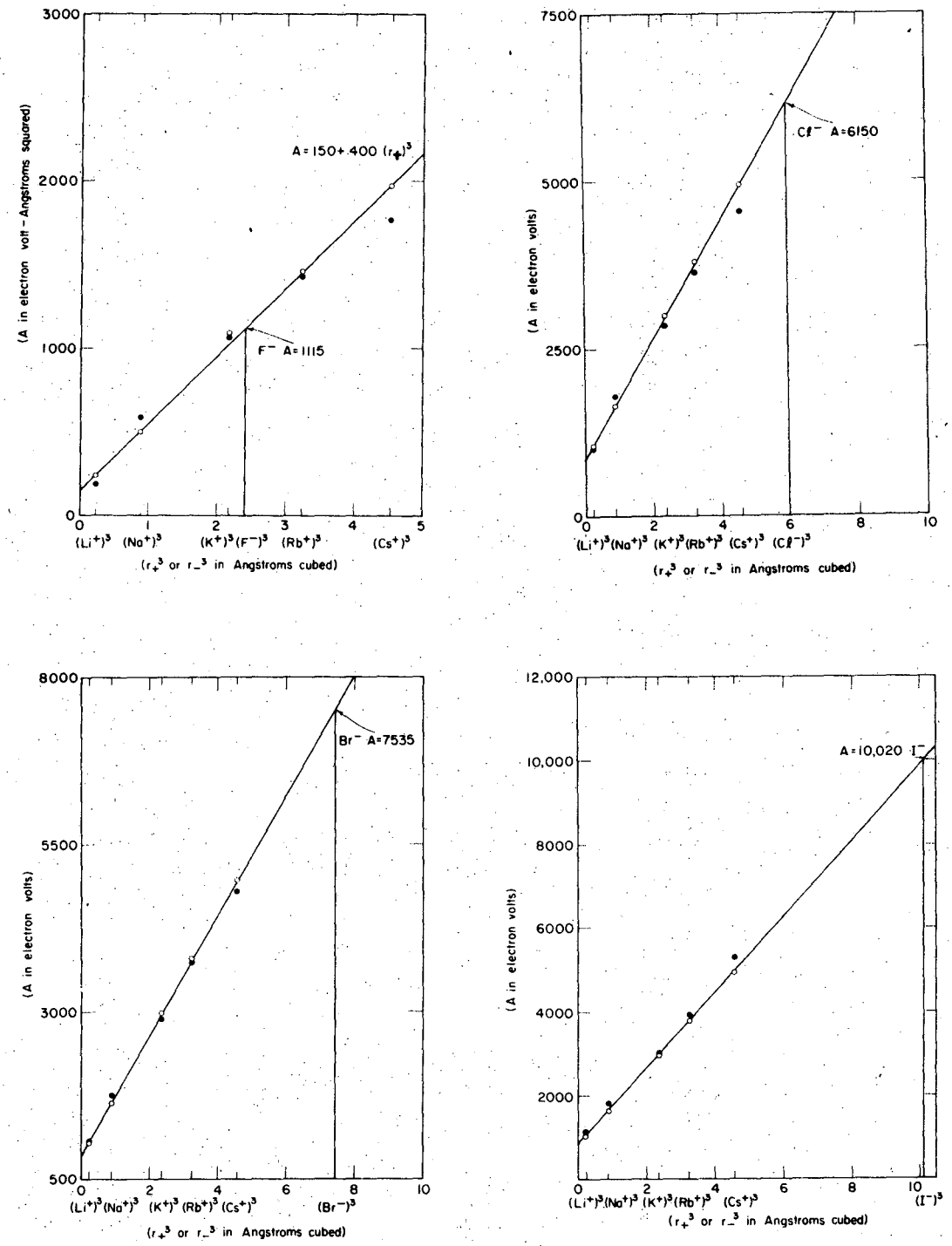

XBL 737-3520A

Fig. III-2. Derivation of the repulsive pre-exponential constant A for the "linear" polarizable ion model ($A = 850 + 900\ (r_+)^3$ eV, unless otherwise noted).

anion, and consequently the electron density on that part of the anion close to the cation. Therefore, a larger repulsion results for the interaction between a given anion and an alkaline earth ion than an alkali metal ion of the same size and at the same distance. To account for this, the values of A obtained from Eqs. (III-6a) or (III-6b) must be multiplied by a factor of 2.6 to apply to our "linear" model repulsion term. This value was chosen to give the best agreement between predicted and experimental values for the equilibrium internuclear distances of $CaCl_2$ and $CaBr_2$, two typical linear alkaline earth dihalide molecules. The complete set of A's, ρ's, and n's used in our model are given in Table III-1.

D. Derivation of the Force on a Bond

At this point, we could calculate directly the potential energy of the system (analogously to our method of Chapter II). However, in this instance we are primarily interested in the force on a given bond. From electrostatics,[28] force F_s and potential energy V_s are related in the following simple manner:

$$V_s = - \int_{\infty}^{P} F_s ds \quad . \qquad \text{(III-7)}$$

P is the point at which evaluation of the potential is to be made. Since the condition that the force vanish at infinity (ions no longer interact) must be met, Eq. (III-7) can be differentiated to obtain directly the force on each bond.

Table III-1. "Linear" Model Input Data

Compound (MX_2)	Dipole Polarizability of Halide (β_D)[a]	Repulsive Pre-Exponential (A)[b]	Repulsive Decay Constant (ρ)[c]	Repulsive Exponent (n)[d]
BeF_2	0.504 Å^3	421. eV - Å^2	0.399 Å	2.
$BeCl_2$	2.11	2280. eV	0.312	0.
$BeBr_2$	3.02	2280.	0.332	0.
BeI_2	4.84	2280.	0.363	0.
MgF_2	0.586	676. eV - Å^2	0.408	2.
$MgCl_2$	2.27	2852. eV	0.319	0.
$MgBr_2$	3.22	2852.	0.339	0.
MgI_2	5.08	2852.	0.369	0.
CaF_2	0.668	1399. eV - Å^2	0.417	2.
$CaCl_2$	2.43	4481. eV	0.326	0.
$CaBr_2$	3.42	4481.	0.345	0.
CaI_2	5.32	4481.	0.375	0.
SrF_2	0.701	1890. eV - Å^2	0.421	2.
$SrCl_2$	2.49	5586. eV	0.329	0.
$SrBr_2$	3.51	5586.	0.348	0.
SrI_2	5.42	5586.	0.377	0.
BaF_2	0.754	2948. eV - Å^2	0.427	2.
$BaCl_2$	2.59	7968. eV	0.333	0.
$BaBr_2$	3.64	7968.	0.352	0.
BaI_2	5.58	7968.	0.380	0.

[a]See Ref. 7.

[b]A = 2.6 A from Eq. (III-6a) or (III-6b), or from Fig. III-2.

[c]See Eq. (III-5a) or (III-5b), or Fig. III-1.

[d]See Ref. 69.

$$\frac{\partial}{\partial s}[V_s] = \frac{\partial}{\partial s}\left[-\int_{\infty}^{P} F_s ds\right]$$

$$= -F_s \qquad \text{(III-8a)}$$

or

$$F_s = -\nabla V_s \qquad \text{(III-8b)}$$

Since we already have a general expression for the repulsion potential energy $\underline{\phi_r}$, the "repulsive" force can be readily obtained by application of Eq. (III-8b).

$$F_r = -\nabla\phi_r = -\frac{\partial}{\partial r}[Ar^n \exp(-r/\rho)]$$

$$= -Ar^{n-1} \exp(-r/\rho)\ [n - r/\rho] \qquad \text{(III-9)}$$

To calculate the "attractive" force due to the electrostatic interactions we first calculate the potential energy. Then the resultant potential energy expression is differentiated (using Eq. (III-8b)) to obtain the corresponding force.

In Fig. III-3, consider point charges at <u>A</u> and <u>C</u>, and a spherical conductor with its center at <u>B</u> and carrying a negative charge <u>-e</u>. The radius <u>b</u> of the spherical conductor is given by the cube root of the dipole polarizability of the <u>anion</u> ($\underline{\beta_D}$). This model gives all the charge-charge interactions, but only <u>one-half</u> of the charge-dipole terms. Hence, all derived charge-dipole terms need to be doubled.

Charges: $q_a = q_{sc} = -e$

$q_c = +2e$

$q_a' = +eb/2r \cos\theta$

$q_c' = -2eb/r$

$q_b = -e(1 - \frac{2b}{r} + \frac{b}{2r\cos\theta})$

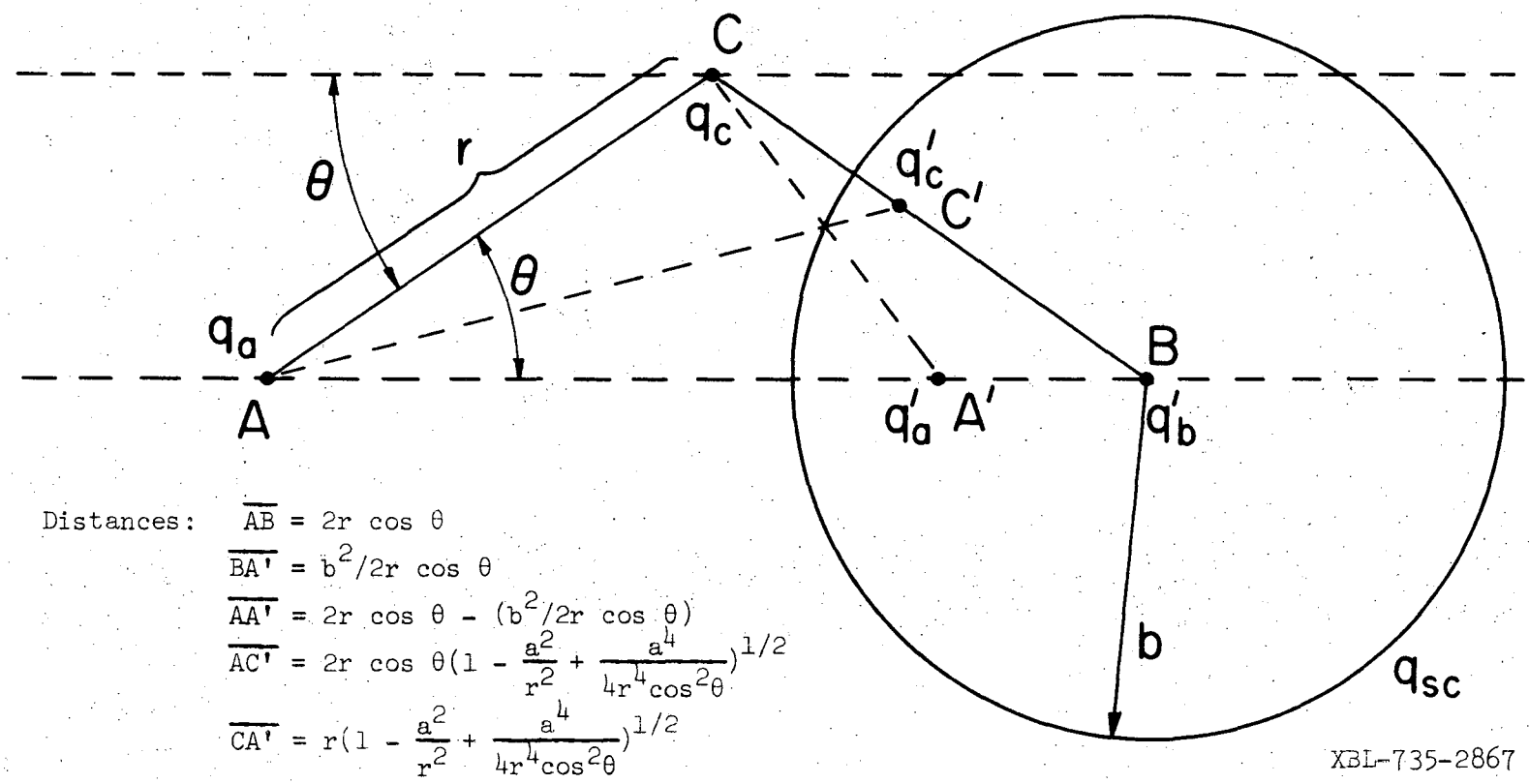

Distances: $\overline{AB} = 2r\cos\theta$

$\overline{BA'} = b^2/2r\cos\theta$

$\overline{AA'} = 2r\cos\theta - (b^2/2r\cos\theta)$

$\overline{AC'} = 2r\cos\theta(1 - \frac{a^2}{r^2} + \frac{a^4}{4r^4\cos^2\theta})^{1/2}$

$\overline{CA'} = r(1 - \frac{a^2}{r^2} + \frac{a^4}{4r^4\cos^2\theta})^{1/2}$

$\overline{BC'} = b^2/r$

$\overline{CC'} = r - (b^2/r)$

Fig. III-3. Image Charge System for MX_2 molecules (Polarized Anions).

Once again the method of electrostatic images[26] is used to evaluate the potential energy of the system. The spherical conductor is replaced by the image charges q_A' at A' and q_C' at C' and the charge q_B at B. Using Eq. (II-6a), the potential energy becomes

$$\phi_{ei} = \frac{1}{2}\left[(-e)U_a + (+2e)U_c + (-e)U_b\right] \quad . \tag{III-10}$$

U_a and U_c are the potentials at A and C, respectively, while U_b is the potential at the surface of the spherical conductor.

The various potentials are evaluated in a manner entirely analogous to that in Chapter II (pp. 13-17). Initially, we assume a general angle θ, which later is set to zero for the linear case.

$$U_a = \frac{q_c}{AC} + \frac{q_c'}{AC'} + \frac{q_a}{AA'} + \frac{q_b}{AB}$$

$$= \frac{(+2e)}{r} + \frac{(-2eb/r)}{(2r\cos\theta)\left(1 - \frac{a^2}{r^2} + \frac{a^4}{4r^4\cos^2\theta}\right)^{\frac{1}{2}}}$$

$$+ \frac{(eb/2r\cos\theta)}{\left(2r\cos\theta - \frac{b^2}{2r\cos\theta}\right)} + \frac{\left(-e\left(1 - \frac{2b}{r} + \frac{b}{2r\cos\theta}\right)\right)}{2r\cos\theta} \tag{III-11a}$$

$$U_c = \frac{q_a}{AC} + \frac{q_a'}{A'C} + \frac{q_c'}{CC'} + \frac{q_b}{BC}$$

$$= \frac{(-e)}{r} + \frac{(eb/2r\cos\theta)}{r\left(1 - \frac{a^2}{r^2} + \frac{a^4}{4r^4\cos^2\theta}\right)} + \frac{(-2eb/r)}{\left(r - \frac{b^2}{r}\right)}$$

$$+ \frac{\left(-e\left(1 - \frac{2b}{r} + \frac{b}{2r\cos\theta}\right)\right)}{r} \tag{III-11b}$$

$$U_b = \frac{q_b}{b} = \frac{-e(1 - \frac{2b}{r} + \frac{b}{2r\cos\theta})}{b} \quad . \qquad \text{(III-11c)}$$

Applying the binomial series expansion ($b < r$ in all cases) where appropriate and collecting terms, we obtain,

$$U_a = \frac{e}{r}\left[2 - \frac{1}{2\cos\theta}\right] + \frac{eb^3}{r^4}\left[\frac{-1}{2\cos\theta} + \frac{1}{16\cos^4\theta}\right] \qquad \text{(III-12a)}$$

$$U_c = -\frac{2e}{r} + \frac{eb^3}{r^4}\left[\frac{1}{4\cos\theta} - 2\right] \qquad \text{(III-12b)}$$

$$U_b = -\frac{e}{b} + \frac{e}{r}\left[2 - \frac{1}{2\cos\theta}\right] \quad , \qquad \text{(III-12c)}$$

where only the terms up to and including charge-dipole interactions are retained. Remembering to double all charge-dipole terms, we substitute Eqs. (III-12a), (III-12b), and (III-12c) into Eq. (III-10), and obtain

$$\phi_{ei} = \frac{1}{2}\left[-\frac{e^2}{r}\left(2 - \frac{1}{2\cos\theta}\right) - \frac{e^2b^3}{r^4}\left(\frac{-1}{\cos\theta} + \frac{1}{8\cos^4\theta}\right) + \right.$$

$$\left. - \frac{4e^2}{r} + \frac{e^2b^3}{r^4}\left(\frac{1}{\cos\theta} - 8\right) + \frac{e^2}{b} - \frac{e^2}{r}\left(2 - \frac{1}{2\cos\theta}\right)\right]$$

$$= \frac{e^2}{2b} - \frac{e^2}{r}\left(4 - \frac{1}{2\cos\theta}\right) - \frac{e^2b^3}{r^4}\left(4 - \frac{1}{\cos\theta} + \frac{1}{16\cos^4\theta}\right) \quad . \qquad \text{(III-13)}$$

Using Eqs. (III-8b) and (III-13), we obtain for the total "attractive" electrostatic force,

$$F_{ei} = -\frac{e^2}{r^2}\left(4 - \frac{1}{2\cos\theta}\right) - \frac{e^2\beta_d}{r^5}\left(16 - \frac{4}{\cos\theta} + \frac{1}{4\cos^4\theta}\right) \quad , \qquad \text{(III-14)}$$

where b^3 is replaced by $\underline{\beta_d}$. Since we wish to consider only the electrostatic force which is applied to <u>one</u> of the two equivalent internuclear bonds, the appropriate single-bond force $\underline{F_b}$ is

$$F_b = \frac{1}{2} F_a = -\frac{e^2}{r^2}\left(2 - \frac{1}{4\cos\theta}\right) - \frac{e^2\beta_d}{r^5}\left(8 - \frac{2}{\cos\theta} + \frac{1}{8\cos^4\theta}\right) \quad . \qquad \text{(III-15)}$$

Then by summing this "attractive" single-bond force and the repulsive force (Eq. (III-9)), we obtain the total force exerted on a given bond:

$$F = F_b + F_r = -\frac{e^2}{r^2}\left(2 - \frac{1}{4\cos\theta}\right) - \frac{e^2\beta_d}{r^5}\left(8 - \frac{2}{\cos\theta} + \frac{1}{8\cos^4\theta}\right)$$

$$+ Ar^{n-1}\exp(-r/\rho)\left[\frac{r}{\rho} - n\right] \quad . \qquad \text{(III-16)}$$

Using the equilibrium condition stated in Eq. (III-1) (for a more familiar form, consult Eq. (III-3)) and remembering that $r = \ell$ at equilibrium, we obtain

$$0 = -\frac{e^2}{\ell^2}\left(2 - \frac{1}{4\cos\theta}\right) - \frac{e^2\beta_d}{\ell^5}\left(8 - \frac{2}{\cos\theta} + \frac{1}{8\cos^4\theta}\right)$$

$$+ A\ell^{n-1}\exp(-\ell/\rho)\left[\frac{\ell}{\rho} - n\right] \quad . \qquad \text{(III-17a)}$$

For linear geometry Eq. (III-17a) simplifies to

$$0 = -\frac{e^2}{\ell^2}(7/4) - \frac{e^2\beta_d}{\ell^5}(49/8) + A\ell^{n-1}\exp(-\ell/\rho)\left[\frac{\ell}{\rho} - n\right] \quad . \tag{III-17b}$$

E. Derivation of the Stretching Force Constant

At equilibrium, the restoring force on a bond can be expressed as

$$F = -k_1\ell \quad , \tag{III-18a}$$

where k_1 is the stretching force constant; conversely,

$$k_1 = -\partial F/\partial \ell \quad . \tag{III-18b}$$

Since we already have a general expression for the force F (Eq. (III-16)), the stretching force constant for the linear case is readily obtained:

$$k_1 = -\frac{2e^2}{\ell^3}(7/4) - \frac{e^2\beta_d}{\ell^6}(245/8) +$$

$$- \left[-\frac{\ell^n}{\rho^2} + \frac{2n\ell^{n-1}}{\rho} - n(n-1)\ell^{n-2}\right] A\exp(-\ell/\rho) \quad . \tag{III-19}$$

Remembering the simple harmonic nature of this restoring force,[17] we can relate the stretching force constant to the symmetric stretching frequency ν_1 in a simple manner:

$$\nu_1 = \frac{1}{2\pi}\sqrt{k_1/m_x} \quad , \tag{III-20a}$$

where m_x is the mass of the halide. In our case, the specific form of ν_1 is

$$\nu_1 = \frac{1}{2\pi} \left[\frac{1}{m_x} \left\{- \frac{2e^2}{\ell^3}(7/4) - \frac{e^2\beta_d}{\ell^6}(245/8) + \right.\right.$$

$$\left.\left. - \left(- \frac{\ell^n}{\rho^2} + \frac{2n\ell^{n-1}}{\rho} - \frac{n(n-1)\ell^{n-2}}{1}\right) A \exp(-\ell/\rho)\right\}\right]^{\frac{1}{2}} . \qquad \text{(III-20b)}$$

F. Derivation of the Stretching Frequencies

Actually, the above derivation of the symmetric stretching frequency is an oversimplification. We have assumed that there is a strong restoring force along each bond and opposing a change of the internuclear distance. In addition, there is a strong restoring force opposing a change of the angle between the two bonds of the triatomic molecule. These two valence force assumptions were postulated by Bjerrum.[70] A complete treatment of the stretching frequencies given below can be found in Herzberg.[71]

1. Non-Linear Symmetric MX_2 Molecules

$$\nu_3 = \frac{1}{2\pi} \left[\left(1 + \frac{2m_x}{m_m} \sin^2 2\alpha\right) \frac{k_1}{m_x}\right]^{\frac{1}{2}} , \qquad \text{(III-21)}$$

where ν_3 is the asymmetric stretching frequency and m_m is the mass of the metal. The symmetric stretching frequency ν_1 of the normal vibration cannot be determined without prior knowledge of the bending force constant k_b and the bending frequency ν_2. As was illustrated in Chapter II, these

quantities are extremely difficult to accurately predict or experimentally determine. Thus, we have only calculated the asymmetric stretching frequencies for the non-linear cases.

2. Linear Symmetric MX_2 Molecules

$$\nu_1 = \frac{1}{2\pi} [(k_1/m_x)]^{\frac{1}{2}} \qquad \text{(III-22a)}$$

and

$$\nu_3 = \frac{1}{2\pi} [(1 + \frac{2m_x}{m_m}) \frac{k_1}{m_x}]^{\frac{1}{2}} \quad . \qquad \text{(III-22b)}$$

These equations are just limiting cases ($2\alpha = 180°$) of the non-linear symmetric MX_2 molecule. Comparing Eqs. (III-22a) and (III-20a), we notice that they are identical; our original derivation is perfectably acceptable for linear molecules. Thus, the name "linear" is given to this model, although, through the use of Eq. (III-21), certain non-linear molecules are considered as well.

G. Calculation of Molecular Constants

The equilibrium internuclear distance can be determined by solving Eq. (III-17a). Because of the complexity of the equation, no exact solution is available. By modification of an existing LBL library subroutine, designed to optimize the value of one variable in terms of others, we obtain a highly accurate approximate solution using a high speed digital computer. A detailed explanation of this computer program (NEWTON) appears in Appendix A-1. The only input data needed for this computation consists of

$\beta_d = b^3$ = dipole polarizability of the anion

A, ρ, n = anion-cation repulsion constants

2α = bending angle

for each of the alkaline earth dihalides of interest. The dipole polarizabilities of the anions are linear extrapolations from the alkali halide polarizable ion model (see Table III-1). These values are not the "free-ion" values, but the reduced values as discussed in Hollowell's Ph.D. thesis.[7] The specific values of the repulsion constants also appear in Table III-1. Table III-2 gives a comparison between the calculated equilibrium internuclear distances and experimental values taken from electron diffraction data.[29,30] The agreement is excellent except for the barium and beryllium dihalides. The barium dihalide values would be reduced ~ 2 to 6% if the known bending in these molecules were accounted for (see discussion on the deformation constant in Chapter II). The beryllium dihalide values are considerably high, presumably because of the long extrapolation that must be made to the small beryllium ion.

Using Eq. (III-19), we calculate the stretching force constants. These values are given in Table III-3, along with experimental values from infrared absorption spectroscopy. Then, treating this calculated value of $\underline{k_1}$ as a known quantity, we determine a stretching frequency. For non-linear molecules Eq. (III-21) is used in conjunction with the bending angle values from Table II-3 to calculate the asymmetric stretching frequency $\underline{\nu_3}$. For the linear compounds, Eq. (III-21) simplifies to Eq. (III-22b) in evaluating $\underline{\nu_3}$. We calculate the symmetric stretching frequency $\underline{\nu_1}$ using Eq. (III-22a). For the sake of comparison, calculations

Table III-2. Equilibrium Internuclear Distances

Compound (MX_2)	Equilibrium Internuclear Distance (ℓ) "Linear" Model[a]	Experimental[b]	Percent Deviation[c]
BeF_2	1.49_1	1.40	+6.5%
$BeCl_2$	1.99_5	1.75	+14.0
$BeBr_2$	2.10_4	1.91	+10.2
BeI_2	2.27_8	2.10	+8.5
MgF_2	1.72_9	1.77	-2.3
$MgCl_2$	2.19_7	2.18	+0.8
$MgBr_2$	2.34_5	2.34	+0.2
MgI_2	2.51_9	2.52	-0.04
CaF_2	2.08_4	2.10	-0.8
$CaCl_2$	2.51_7	2.51	+0.3
$CaBr_2$	2.66_0	2.67	-0.4
CaI_2	2.89_4	2.88	+0.5
SrF_2	2.23_3	2.20	+1.5
$SrCl_2$	2.66_2	2.67	-0.3
$SrBr_2$	2.81_4	2.82	-0.2
SrI_2	3.05_3	3.03	+0.8
BaF_2	2.45_4	2.32	+5.8
$BaCl_2$	2.88_0	2.82	+2.1
$BaBr_2$	3.04_7	2.99	+1.9
BaI_2	3.29_6	3.20	+3.0

[a]See Eq. (III-17b).

[b]Values accurate to ±0.03 Å, see Refs. 29 and 30.

[c]Deviation of "linear" model values from experimental values.

Table III-3. Stretching Force Constants

Compound (MX_2)	Stretching Force Constant (k_1) "Linear" Model[a]	Experimental
BeF_2	5.68_0 mdynes/Å	4.96±0.10[b] mdynes/Å 5.0[c] 5.15[d,e] 5.18[f]
$BeCl_2$	2.89_4	2.92±0.08[b] 2.9[c] 3.28[d,e]
$BeBr_2$	2.53_8	2.53[d] (2.35)[b]
BeI_2	2.08_4	1.96[d] (1.85)[b]
MgF_2	4.04_4	2.97±0.07[b] 3.0[e] 3.06[f] 2.74[g] 2.81[h]
$MgCl_2$	2.39_9	1.90±0.06[b,c] 1.83[i]
$MgBr_2$	2.09_6	2.34±0.03[b] 1.48[i]
MgI_2	1.73_3	(1.18)[b]
CaF_2	2.61_9	1.90[b] 2.49[f] 2.20[h]

(continued)

Table III-3 (continued)

Compound (MX_2)	Stretching Force Constant (k_1) "Linear" Model[a]	Experimental
$CaCl_2$	1.81_6	1.18[b]
$CaBr_2$	1.59_5	1.03[b]
CaI_2	1.30_0	0.86[b]
SrF_2	2.22_9	1.62±0.05[b]
		2.22[f]
		1.97[h]
$SrCl_2$	1.60_9	1.04±0.05[b]
		1.37[j]
$SrBr_2$	1.41_0	(0.89)[b]
SrI_2	1.15_8	(0.74)[b]
BaF_2	1.78_7	1.51[b]
		2.49[f]
		2.20[h]
$BaCl_2$	1.35_7	0.97[b]
		1.33[j]
$BaBr_2$	1.18_5	(0.77)[b]
BaI_2	0.97_8	(0.65)[b]

*All stretching force constants have been converted to units of millidynes per Ångstrom for convenience. Values in parentheses are estimated.

[a]See Eq. (III-19).

[b]See Ref. 72.

[c]See Ref. 33.

[d]See Ref. 36.

[e]See Ref. 35.

[f]See Ref. 34.

[g]See Ref. 38.

[h]See Ref. 37.

[i]See Ref. 39.

[j]See Ref. 40.

are sometimes made for both a linear and a non-linear configuration of the same molecule. All the stretching frequencies are summarized in Table III-4 along with experimental data from infrared absorption spectroscopy.

H. Concluding Remarks

Our "linear" polarizable ion model predicts the equilibrium internuclear distances, stretching force constants, and stretching frequencies quite accurately for the alkaline earth dihalides. This is very useful, especially since both the symmetric stretching frequencies and the stretching force constants are difficult to obtain experimentally with great accuracy.

This model, like the model detailed in Chapter II, exhibits some obvious oversimplifications (such as the neglect of the cation polarizability). Unfortunately, a more complete version is mathematically unwieldy. However, as a first approximation to certain fundamental molecular constants, our "linear" model should prove quite useful.

Table III-4. Stretching Frequencies*

Compound (MX_2)	Symmetric Stretching Frequency (ν_1) "Linear" Model Linear[a]	Non-linear[b]	Experimental	Asymmetric Stretching Frequency (ν_3) "Linear" Model Linear[c]	Non-linear[d]	Experimental	Bending Angle (2α)[e]
BeF_2	712.4 cm^{-1}		(668.)[f] cm^{-1} (680.)[g,h]	1627.0 cm^{-1}		1555.[g,h] cm^{-1} 1520.[i]	180°
$BeCl_2$	372.3		(373.)[f] (390.)[h] (380.)[j]	1108.5		1135.[h,j] 1113.[i]	180
$BeBr_2$	232.2		(223.)[f] (230.)[h]	1005.0		(966.)[f] 1010.[h]	180
BeI_2	166.9		(157.)[f] (160.)[h]	901.5		(850.)[f] 873.[h]	180
MgF_2	601.1		(515.)[f] 477.[k,l] (510.)[g] (540.)[j]	962.3		825.[f] 875.[g,j] 840.[k] 827.[l]	180
$MgCl_2$	338.9		(297.)[f,m]	670.7		597.[i] 588.[m]	180
$MgBr_2$	211.0		(178.)[f,m]	580.7		490.[m]	180
MgI_2	152.2		(125.)[f]	514.9		(424.)[f]	180

(continued)

Table III-4 (continued)

Compound (MX_2)	Symmetric Stretching Frequency (ν_1) "Linear" Model: Linear[a]	Symmetric Stretching Frequency (ν_1) "Linear" Model: Non-linear[b]	Symmetric Stretching Frequency (ν_1) Experimental	Asymmetric Stretching Frequency (ν_3) "Linear" Model: Linear[c]	Asymmetric Stretching Frequency (ν_3) "Linear" Model: Non-linear[d]	Asymmetric Stretching Frequency (ν_3) Experimental	Bending Angle (2α)[e]
CaF_2	483.7		(412.)[f] (520.)[g] 520.[j] 483.[l]	675.1	655.7	575.[f] (595.)[g] 595.[j] 545.[l]	140
$CaCl_2$	294.9		(238.)[f]	490.7		395.[f] 394.[n]	180
$CaBr_2$	184.1		(148.)[f]	411.1		330.[f]	180
CaI_2	131.9		(107.)[f]	357.1		290.[f]	180
SrF_2	446.2		(380.)[f] (485.)[g] 485.[j] 441.[l]	534.4	513.7	455.[f] (490.)[g] 490.[j] 443.[l]	120
$SrCl_2$	277.6		(223.)[f] 285.[o]	373.3	366.9	300.[f] 318.[o]	148
$SrBr_2$	173.1		(137.)[f]	290.9	289.0	(231.)[f]	164
SrI_2	124.5		(100.)[f]	245.7		(187.)[f]	180

(continued)

Table III-4 (continued)

Compound (MX_2)	Symmetric Stretching Frequency (ν_1) "Linear" Model: Linear[a]	Symmetric Stretching Frequency (ν_1) "Linear" Model: Non-linear[b]	Symmetric Stretching Frequency (ν_1) Experimental	Asymmetric Stretching Frequency (ν_3) "Linear" Model: Linear[c]	Asymmetric Stretching Frequency (ν_3) "Linear" Model: Non-linear[d]	Asymmetric Stretching Frequency (ν_3) Experimental	Bending Angle (2α)[e]
BaF_2	399.5		(367.)[f] (450.)[g] 450.[j] 413.[l]	451.4	432.5	415.[f] (430.)[g] 430.[j]	104
$BaCl_2$	254.9		(215.)[f] 279.[o]	313.9	303.4	265.[f] 285.[o]	128
$BaBr_2$	158.6		(128.)[f]	233.3	224.4	(188.)[f]	136
BaI_2	114.4		(93.)[f]	193.1	188.8	(157.)[f]	150

*Values in parentheses are estimated.

[a]See Eq. (III-22a).

[b]Not calculated.

[c]See Eq. (III-22b).

[d]See Eq. (III-21).

[e]See Table II-3, (used in Eq. (III-21) only).

[f]See Ref. 72.

[g]See Ref. 49.

[h]See Ref. 33.

[i]See Ref. 35.

[j]See Ref. 34.

[k]See Ref. 37.

[l]See Ref. 36.

[m]See Ref. 38.

[n]See Ref. 39.

[o]See Ref. 40.

IV. ELECTRIC DEFLECTION SPECTROSCOPY

A. Introduction

In order to further test our polarizable ion models, we need to perform gas phase geometry experiments on the metal dihalides. There exist several experimental techniques for determining molecular structures, each capable of high precision. However, the high temperatures and low pressures commonly necessary to vaporize the refractory metal dihalides place severe restrictions on the feasible forms of spectroscopic study. The bulk of the information on the geometry of these molecules comes from electron diffraction, matrix-isolation infrared absorption, or electric deflection spectroscopy. Each form of spectroscopy has its weaknesses. Using the electron diffraction technique, highly precise bond lengths can be ascertained, but often the bending angle (2α) is in doubt by as much as 30°. The matrix itself and the low temperatures necessary to perform the experiment play an uncertain role in infrared absorption spectroscopy. The validity of the electric deflection results depends critically on the sensitivity for detecting a low intensity beam of molecules. We have chosen the electric deflection method to attack the problem of molecular structure because of the availability of the component equipment and because of the background knowledge of this technique accumulated in this laboratory.

The technique of electric deflection can also be applied to numerous other problems.[73] Among these are determination of molecular structure, determination of polarizabilities and dipole moments, measurements of rotational temperatures in a molecular beam, analysis of

fragmentation patterns of mass spectrometry, and characterization of ground state and low-lying electronic levels of molecules. We have confined ourselves primarily to obtaining inferences as to the structures and bonding of numerous gas-phase metal halide molecules. Secondary consideration is given to the determination of fragmentation patterns where they are of interest.

B. Theory

Using the electric deflection technique, a thermally populated beam of the molecule to be studied is directed through a strong inhomogeneous electric field. Polar molecules are deflected by this field in both positive and negative directions (relative to the gradient of the electric field $\nabla\mathcal{E}_s$); a beam of centrosymmetric molecules is deflected only in the positive direction. As was shown in Eq. (III-8b), the force F_s acting on a molecule with potential energy V_s in an electric field $\mathcal{E}_s$ equals the negative gradient of the potential energy,

$$F_s = -\nabla V_s = -(\partial V_s/\partial \mathcal{E}_s)\nabla\mathcal{E}_s \quad . \qquad \text{(IV-1)}$$

For a thermal distribution, $\partial V_s/\partial \mathcal{E}_s$ can be both positive and negative for polar molecules, but only negative for non-polar molecules. Expressing Eq. (IV-1) in another way,

$$F_s = \mu_e \nabla\mathcal{E}_s \quad , \qquad \text{(IV-2)}$$

where μ_e is the effective dipole moment of the molecule in the direction of the field. For a centrosymmetric molecule, μ_e is equal to $\alpha\mathcal{E}$, where α is the polarizability of the molecule. Therefore, μ_e is necessarily positive if $\partial V_s/\partial \mathcal{E}_s$ is to be negative.

For polar molecules, the situation is considerably more complex. Depending on the type of polar molecule involved, $\underline{\mu_e}$ may depend on various rotational and vibrational quantum numbers, the moment of inertia, and the permanent dipole moment and its derivatives, as well as on the polarizability and field strength. These complicated relationships allow the effective dipole moment to assume both positive and negative values.

Further consideration of electric moments in connection with the Stark effect,[74-76] is beyond the scope of this work. The point here is that molecules possessing permanent dipole moments can be differentiated from centrosymmetric molecules by use of an inhomogeneous electric field.

C. Deflection System

The inhomogeneous electric field used to determine whether molecules possess a permanent dipole moment is created by four alternately charged rods (quadrupole) placed at the corners of a square. The beam of molecules is aimed directly along the axis of this array. In electric quadrupoles,[77] the gradient of the absolute value of the electric field points radially outward. The array is made optically opaque by a stopwire (see Fig. IV-1), which prevents molecules that interact weakly (or not at all) from reaching the detector. Thus, the only molecules to travel directly from source to detector are those that interact strongly with the electric fields. As is illustrated in Fig. IV-1, all molecules for which $\partial V_s/\partial \mathcal{E}_s$ is negative are deflected away from the axis of the beam path and will never strike the detector. On the other hand, a significant fraction of the molecules for which $\partial V_s/\partial \mathcal{E}_s$ is positive follow paths (solid lines in Fig. IV-1) that curve around the stopwire and reach the

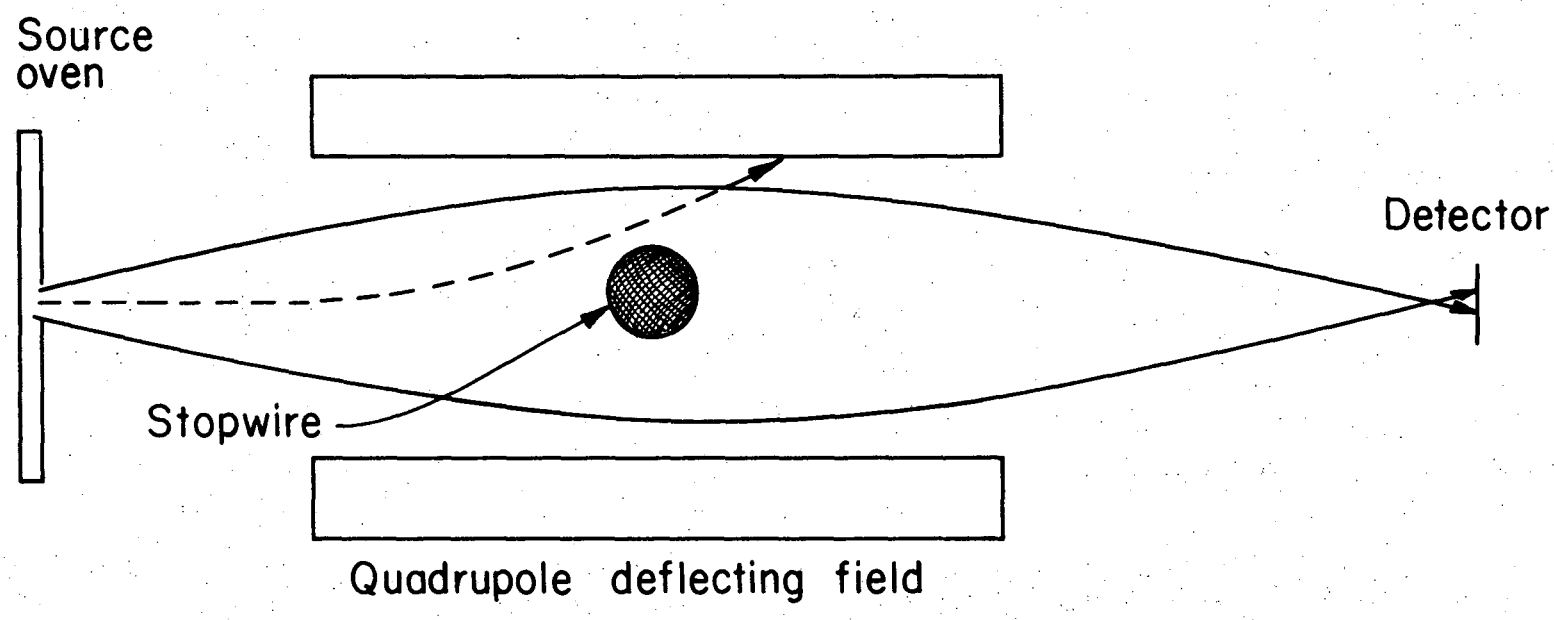

XBL 735-2866

Fig. IV-1. Deflection system.

detector. In essence, we can detect the presence of molecules possessing permanent dipole moments, since beams of these molecules undergo "refocusing". Moreover, as the voltage applied to this quadrupole is increased, the transmission through the electric field also increases. Thus, a larger flux of molecules reaches the detector.

V. EXPERIMENTAL APPARATUS AND PROCEDURES

A. Introduction

We have constructed a high sensitivity electric deflection apparatus by modifying an existing molecular beam spectrometer. This spectrometer was originally designed by Alvin Hebert and was initially used by Carlos Melendres to perform mass spectroscopic studies. The basic apparatus, shown in Fig. V-1, is described briefly in this chapter; a more detailed account is available in Melendres' Ph.D. thesis.[78]

A quadrupole assembly designed to electrically deflect and refocus a beam of molecules has been added to the basic apparatus. High sensitivity is achieved by placing the quadrupole deflecting field close to the beam source to give a large acceptance aperture. Another major advantage of our system over those of earlier experimenters[12,79] is the incorporation of a pulsed-voltage, continuous time-averaging data acquisition system.[80] Such signal averaging provides significant improvement in the signal-to-noise ratio; consequently, much smaller experimental effects can be observed. In addition, phase-sensitive detection is employed to allow easy discrimination between beam components and residual background gases. (Kaufman and Kolb have recently used these techniques to investigate reactive intermediates.[81,82])

B. Apparatus[†]

The basic apparatus consists of three sections: the oven chamber (OC), the buffer chamber (BC), and the detection chamber. The oven

[†]The capital letters in parentheses following various pieces of apparatus in this chapter refer to Fig. V-1.

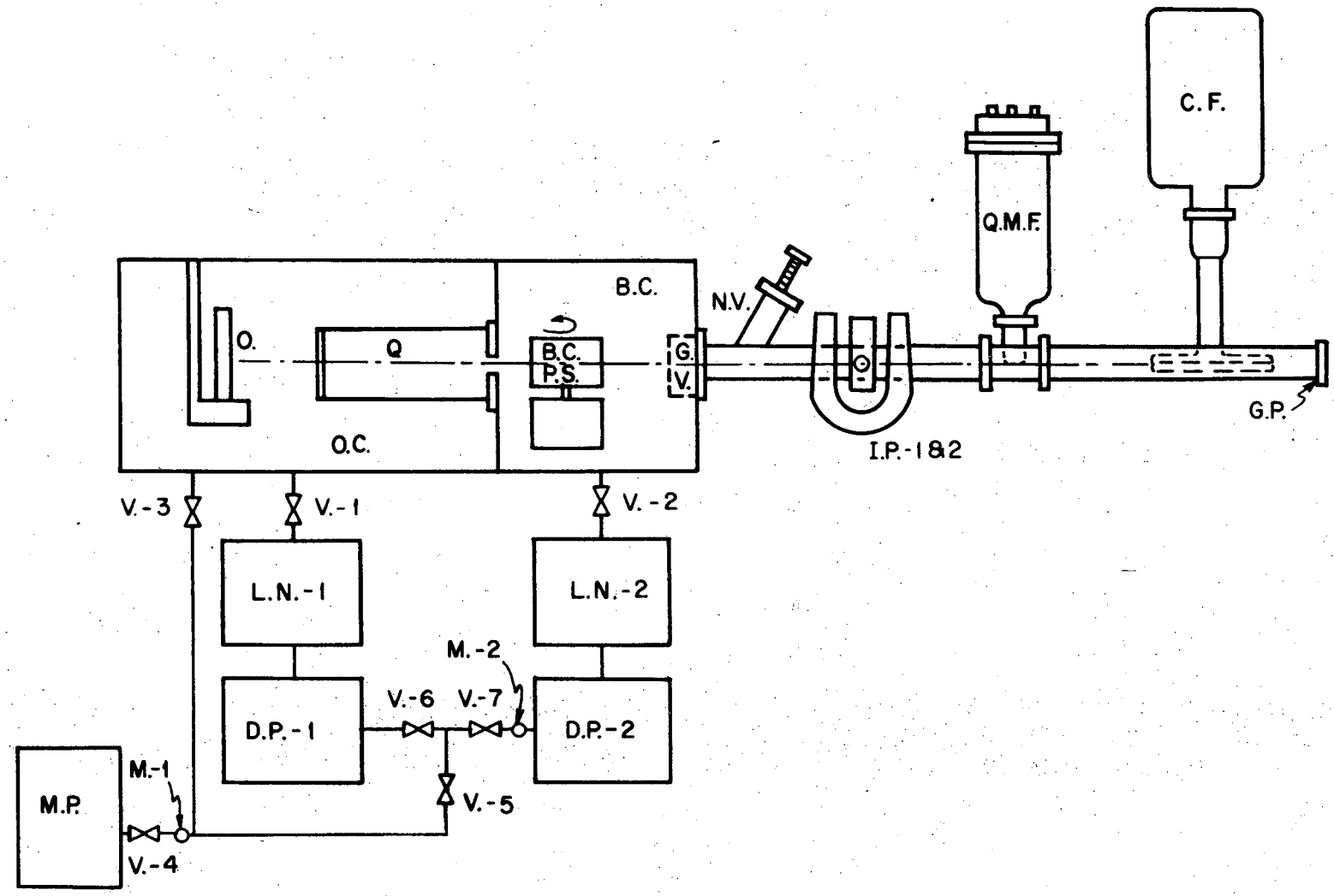

Fig. V-1. Electric Deflection Apparatus

XBL731-2188

chamber was constructed primarily to house the beam source - an effusive oven (O). A quadrupole assembly (Q) designed to electrically deflect the resultant beam of molecules has been added to this chamber.

The oven and buffer chambers, though directly connected, are separately pumped to high vacuum by oil diffusion pumps (DP-1 & 2). This differential pumping of the oven and buffer chambers maintains pressures of approximately 5×10^{-7} and 2×10^{-7} torr, respectively, as measured by ion gauges. The pressures measured by these gauges are only a relative indication of pressure due to obvious gradients inside the apparatus. A mechanical pump (MP) is used to "pump down" these chambers from atmospheric pressure to a pressure at which the diffusion pumps work acceptably. An electrical protection system is provided to shut off the diffusion pumps in case of increases in pressure or temperature above preset standards, or failure of the water cooling system. An automated liquid nitrogen fill system designed by Alvin Hebert maintains all liquid nitrogen traps. A complete listing of the vacuum equipment appears in Appendix A-4, Table V-1.

The buffer chamber contains a beam modulator (BCPS) which readily can be removed from the beam path. This chopper is necessary to differentiate trace components of a molecular beam from the residual background gases. A gate valve shutter device (GV) is mounted within the detection chamber for ease in monitoring the presence or absence of a beam of molecules.

The detection chamber is connected to the buffer chamber by a needle valve (NV). When this valve is closed two ion pumps (IP-1 & 2)

each with 8 liters per second pumping speed maintain a vacuum of 10^{-8} torr or less. The quadrupole mass filter assembly[83,84] (QMF) is mounted perpendicularly to the beam path, thereby increasing the collision probability between the beam and the bombarding electrons. A thoriated iridium filament,[85] a grid to control electron energy, and a series of electrodes act to extract the ions formed from the beam and focus them on the quadrupole entrance. A dc voltage and a superimposed rf voltage applied to the pole pieces of the quadrupole create an electrostatic field between the rods. The equations of motion of an ion in such a field[86] show that only ions with specific charge to mass ratios can transverse the field at a given rf frequency and a given ratio of rf voltage to dc voltage. This filtering action allows one to selectively discriminate, as to mass, ions with a given charge. Transmitted ions are detected by an electron multiplier with copper-beryllium dynodes. This quadrupole mass filter system permits analyses of masses of 1 amu to 500 amu. The ion energy can be manually controlled from 5 to 45 electron volts, whereas the electron energy is variable between 10 and 90 electron volts. A concentric stainless steel cylinder (CF) filled with liquid nitrogen acts as a cryogenic pump in the area beyond the filament. The glass port (GP) allows viewing of the filament for the purpose of beam alignment.

C. Details of Modifications for Electric Deflection Experiments

1. Molecular Beam Source Oven

The ovens used as a beam source in this experiment are 20% iridium-80% platinum alloy tubes with a 0.953 centimeter outer diameter

and a 0.0254 centimeter wall thickness. A variety of apertures was tested for suitability. The necessary criteria were: 1) sufficient beam intensity for the purposes of detection, 2) effusive[87-90] as opposed to hydrodynamic flow, and 3) sufficient collimation on the quadrupole entrance. Obviously the first two conditions tend to work against one another so some compromise must be reached. Experience in this laboratory[78,91] combined with theoretical arguments[92] yielded the following guideline: The width and thickness of the effusion orifice must be much smaller than the mean free path of the gas molecules at operating temperatures and pressures, the so-called "ideal slit" condition.[93]

Initially, attempts were made to use the tube with a long narrow slit (0.635 centimeters × 0.0127 centimeters) traditionally used in beam studies by experimenters in this laboratory.[8] The third criterion, however, was not satisfied so several alternatives were tested: the slit was shortened (length = 0.3125 centimeters), the slit was made into a circle (diameter = 0.0762 centimeters), and, finally, the circle was made smaller (diameter = 0.0381 centimeters). The smaller circular orifice satisfied all the necessary conditions, so tubes with these specifications were machined in the LBL Precision Shop. Certain improvements were made in these ovens during the course of the experiments. (These changes are detailed in Chapter VI under SrI_2.) The oven temperature is regulated by resistance heating controlled by a Variac. The temperature of the oven (and presumably the molecular vapor) at the point of effusion is measured with a micro optical pyrometer through a glass port in the oven chamber. The range of temperatures measured varies from 1020° Kelvin (the low end

of optical visibility) to approximately 1800° Kelvin (the high temperature extreme of durability of Pt-Ir ovens). Temperature observations should be considered as relative, not absolute, measurements due to the temperature gradients inherent in this type of oven.

2. Electric Deflecting Field

Originally, the quadrupole field was provided by four stainless steel rods 0.250 inches in diameter and 3.0 inches in length mounted parallel to each other in a rectangular array. In order to increase the quadrupole field effect, 0.0625 inch diameter pieces of stainless steel were welded to the inside of each pole piece. This reduced the separation between pole pieces from 0.250 inches to 0.125 inches, which effectively quadrupled the electric field. (The electric field is proportional to $1/r_o^2$ where r_o is the separation of the pole pieces.) The whole quadrupole assembly is housed in an alumina insulator which in turn is bolted, along with the two "ground" pole pieces, to the partition separating the oven and buffer chambers. Holes have been drilled in the alumina to allow the escape of the gases; a gas build-up could lead to an electrical discharge during operation. The two "hot" pole pieces are bolted to a cover plate containing a 0.3125 inch center-tapped hole (as does the alumina insulator) for passage of the beam. This assembly is held in place by a stainless steel ring of adjustable size equipped with an electrical connection to the high voltage source. A schematic diagram and cross sectional views of the quadrupolar assembly appear in Fig. V-2.

The electric field on the quadrupole is initiated by an unregulated high voltage power supply. This high voltage source is turned on by a

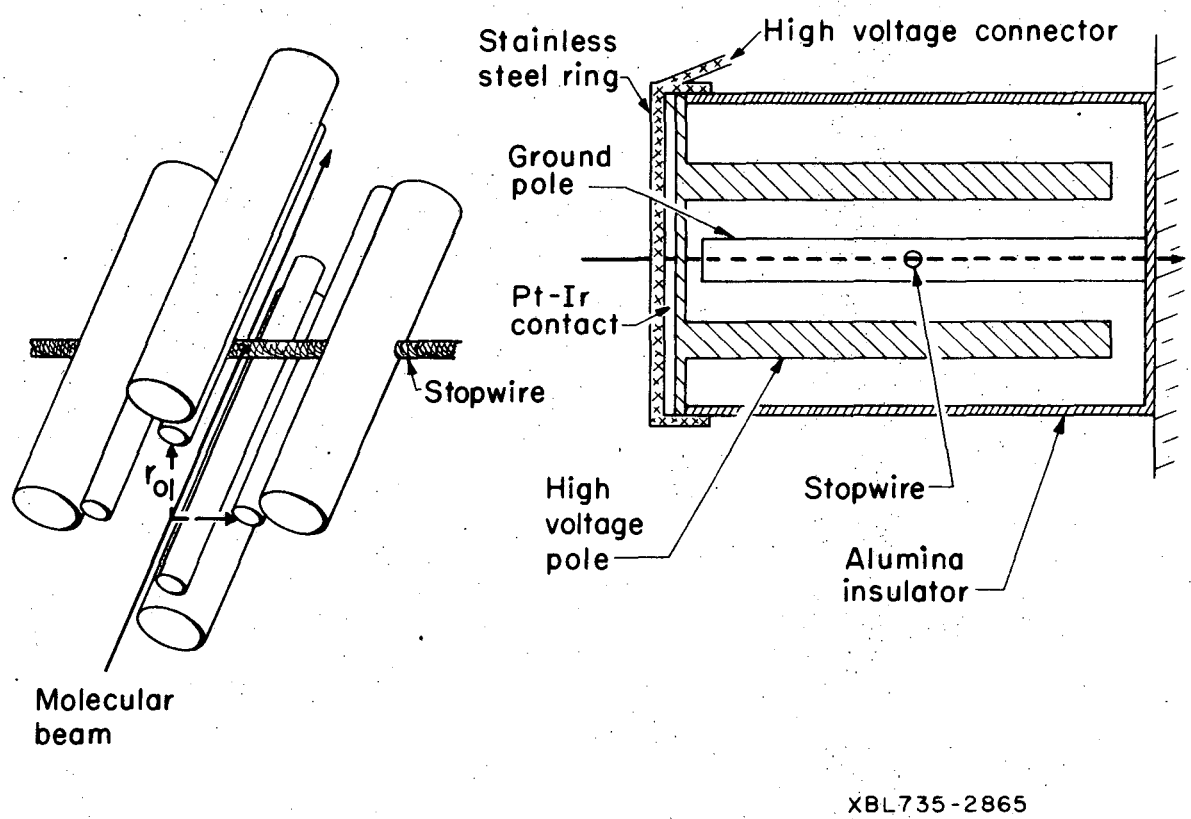

Fig. V-2. Quadrupole assembly.

filament and remains on during the course of the experiment. However, it is desirable to pulse the current supplied to the quadrupole itself. We accomplish this by means of a relay connected to the primary of the high voltage supply. The relay in turn is pulsed by a commercial pulse generator. The pulse generator actually amplifies a pulse which is produced by a 50 volt power supply, and is routed via the multi-channel analyzer (for synchronous timing). The relay system was chosen over a simpler high voltage switching mechanism because of the inherent difficulties in operating the latter.

A Variac is used to allow continuous variation of the deflection voltage from 0. to 30. kilovolts. Actually, electrical breakdown generally occurs between 19. and 23. kilovolts. An internal resistor "bleeder string" allows gradual voltage decay when the relay contact is broken. This bleeder string also provides a means of monitoring the output voltage on a standard oscilloscope. These monitored deflection voltages are presumed accurate to ±5%.

The ground potential pole pieces serve to hold the 0.125 inch diameter stopwire (SW) which prevents undeflected molecules from reaching the detector. A cross section of the stopwire is shown in Fig. V-3. The position designated "hole" is used to locate the straight-through molecular beam. The positions labelled "thin rod", "small ball", "large ball", and "full rod", respectively, obscure more and more of the straight through beam. From outside the oven chamber, without breaking the vacuum, the stopwire assembly can be moved (perpendicularly to the beam flow) to any given position during an experiment. Each position has been carefully

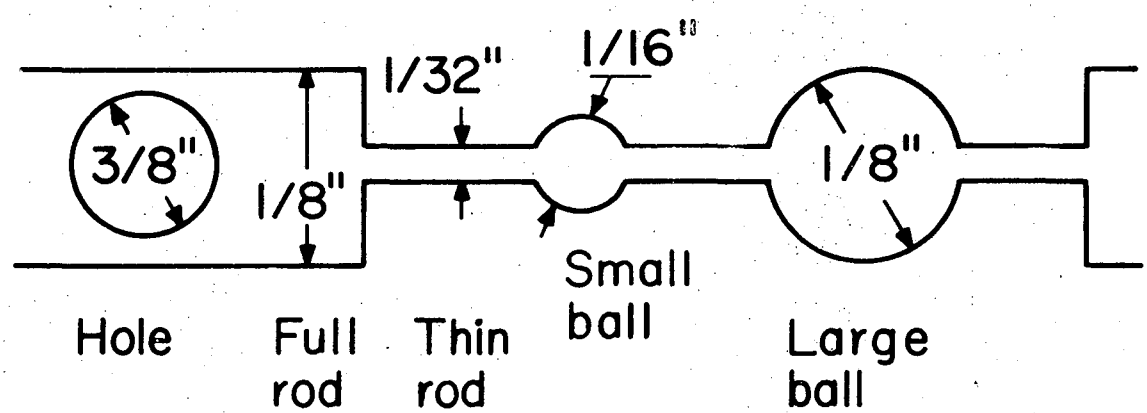

XBL735-2864

Fig. V-3. Stopwire cross section.

calibrated for reproducibility. The stopwire and the stainless steel portions of the quadrupole itself have been electropolished to avoid electrical breakdown due to sharp edges.

3. Phase Sensitive Detection System

The beam chopper consists of a commerical synchronous hystersis motor on which is mounted a paddlewheel for modulation. This motor is driven by a stereo amplifier controlled by a 50 volt power supply and a voltage-to-frequency converter. The frequency of the paddlewheel (normally about 50 cycles per second) can be continuously varied to provide the desired modulation. A light bulb and a photodiode mounted on opposite sides of the chopper provide a reference signal for tuning a lock-in amplifier. Part of the electrometer signal directly drives one pen on a 2-pen recorder. The other part of the signal is used as input first into an impedance matching transformer, then into a low-noise pre-amplifier which enhances the signal-to-noise ratio of the mass spectrum. From the pre-amplifier, the signal passes through a lock-in amplifier, whose output drives the second pen of the recorder. Thus, a spectrum of the modulated beam components is superimposed on a complete spectrum of electrometer signals including mass peaks from residual background gases. For major beam components no modulation is necessary; however, an inherent difficulty in detection sensitivity of minor components of the beam (similar to that mentioned by Melendres[78]) is observed without modulation. With the chopper even large background signals interfere very little with detection of minor constituents of the beam. This detection system is diagrammed in Fig. V-4. A list of components and their specifications is given in Appendix A-4, Table V-2.

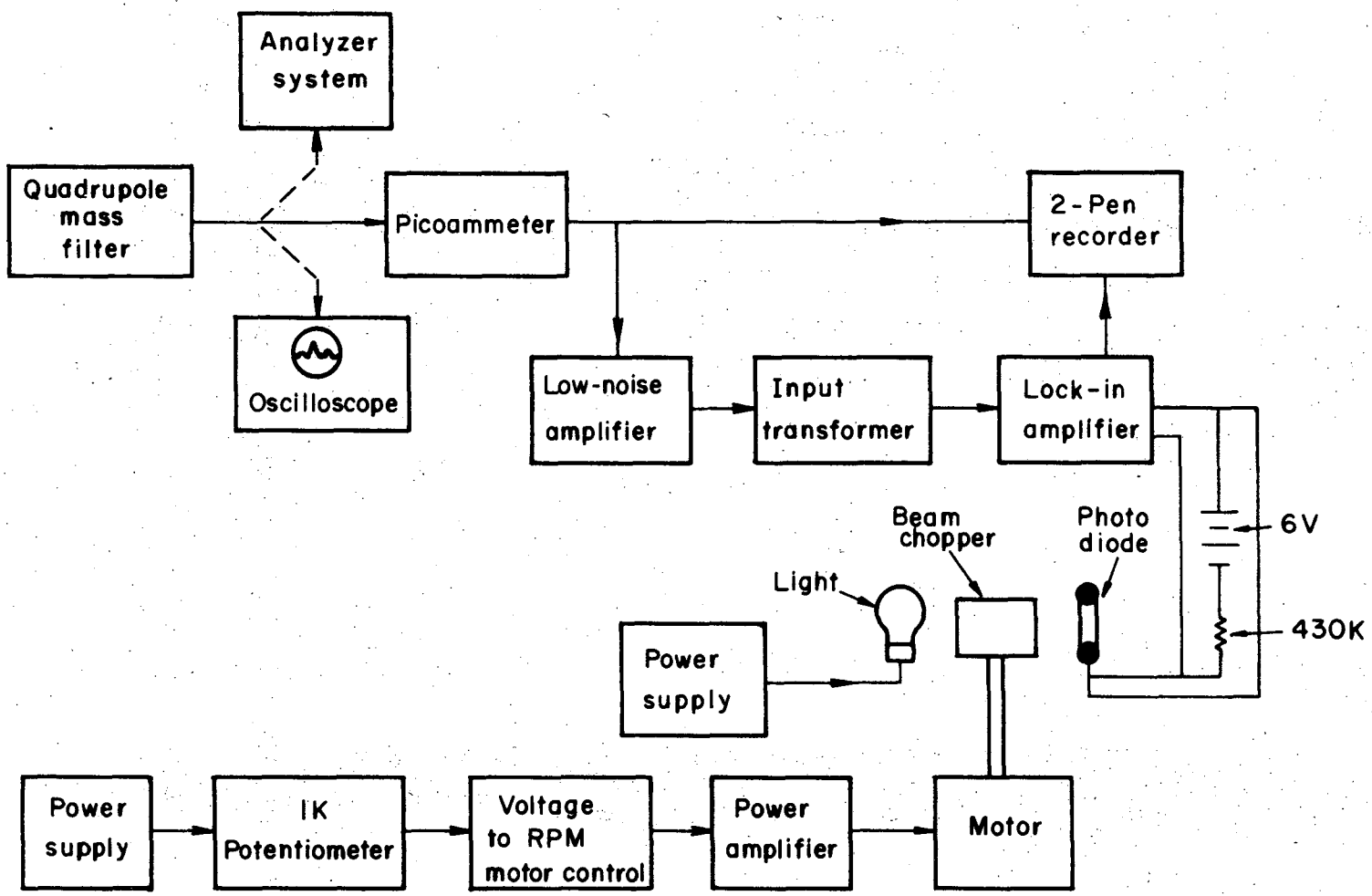

Fig. V-4. Beam Detection System

XBL731-2186

D. Multichannel Analyzer Data Retrieval System

The detection system previously outlined is extremely sensitive to source pressure and ambient vacuum pressure fluctuations. Since reproducibility of results is of prime importance, repetition and storage of signal intensities in the multichannel analyzer over a period of many hours is highly desirable. Moreover, significant improvement in the signal to noise ratio (compared to previous systems[8]) is obtained using a multichannel analyzer: The signal accumulates in direct proportion to the number of counts, while noise is proportional to the square root of the number of counts.

The signal from the electrometer can be switched to pass through a rf filter, a pulse amplifier, and a pulse discriminator before being visually displayed by an electronic counter. (The rf filter removes spurious signals caused by the mass spectrometer rf generator.) The signal is then fed into a switch programmed time based oscillator. A start pulse serves to trigger the 4 Quad multiplexer, frequency synchronizer, and time based oscillator (TIBO). The TIBO in turn starts the multichannel analyzer by programming the analyzer's "live", or count accepting, time per channel and "dead", or advance and memory storage, time per channel. The dead time for the Northern Scientific analyzer used is 3×10^{-5} seconds per channel, or $\sim$ 7.6 milliseconds for the 256 channels of one quadrant. The analyzer has four quadrants which can be selected for use individually or jointly by virtue of the 4 Quad multiplexer. The resultant "intensity versus time" sweep is designed to store and accumulate the spectrometer signal in the form of counts in the multichannel analyzer. This data may

be displayed visually on its oscilloscope from which Polaroid photographs can be taken, and/or can be read out directly on paper tape by means of a printer. A block diagram of the data acquisition system is given in Fig. V-5, and a list of the electronic components and their specifications can be found in Appendix A-4, Table V-3.

A 50 volt power supply and the 4-Quad multiplexer provide a pulse at the start of a sweep of a specific quadrant. This triggering pulse is then relayed directly to the pulse generator as mentioned previously. The purpose is to make the voltage pulse causing electric deflection coincide reproducibly with the sweep position in a given quadrant of the analyzer.

E. Experimental Procedures

1. Operational Checks

A check on the sensitivity of the quadrupole mass filter is made by taking the spectrum of residual background gases of low atomic mass (less than 50 amu). This spectrum[8] is well established and has been used as an easy spot check on the operation of the mass spectrometer throughout the experiments. This residual spectrum also gave a rough calibration standard for the mass scale, which later assisted in locating sample peaks.

A preliminary test of procedures and equipment was made on sodium cyanide (NaCN). These experiments were easily confirmed by studies performed on a velocity selector in this laboratory.[94] The results suggested some minor apparatus adjustments which were made to improve subsequent experiments.

2. Experimental Modifications

Initially a heat shield consisting of two 2. inch diameter discs and a 3. inch diameter outer "mushroom-like" cap (all made of 0.010 inch

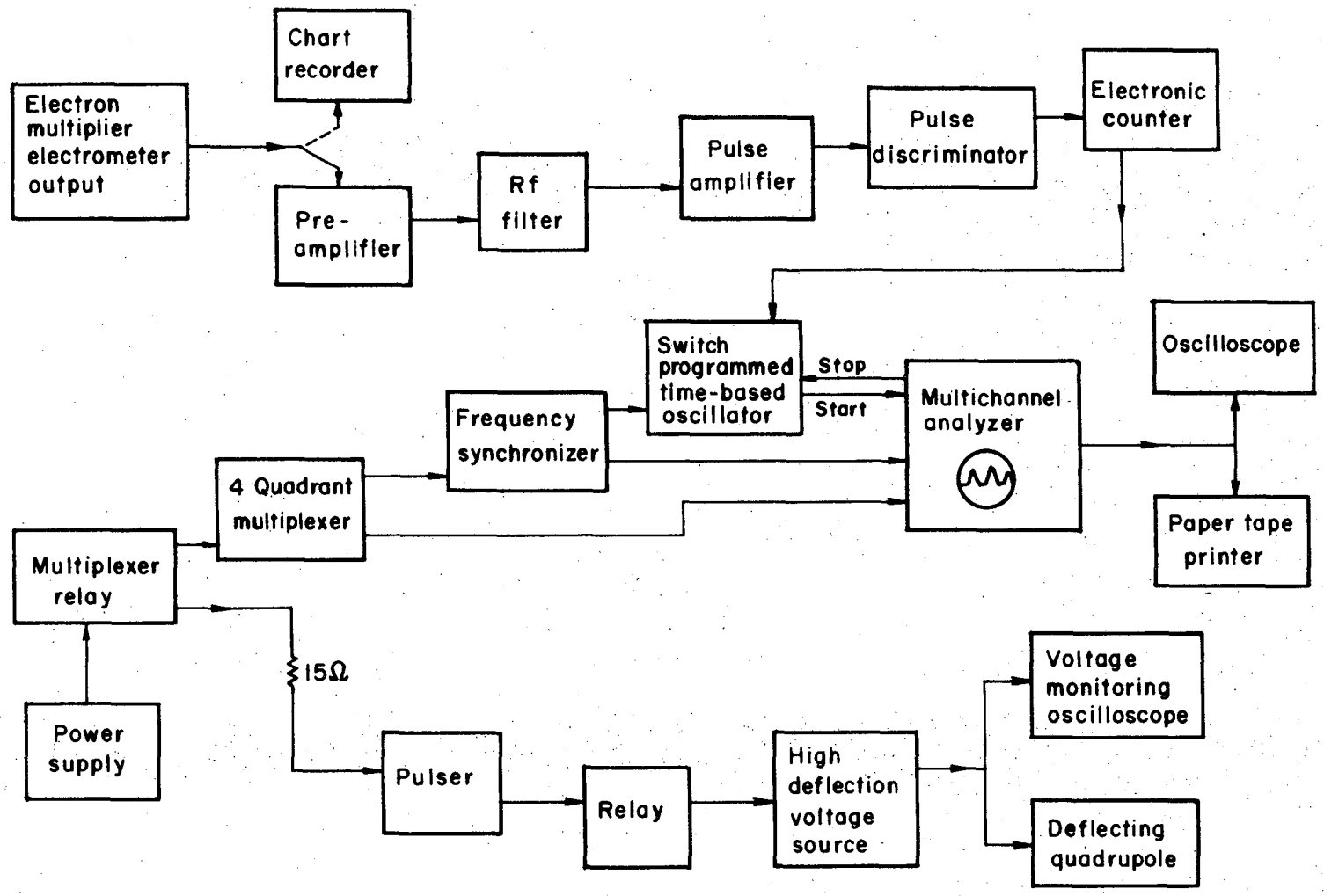

Fig. V-5. Signal Averaging and Synchronous Voltage Pulse Production Systems

XBL 731-2187

tantalum foil) was bolted to the "hot" end of the quadrupole. Individual pieces were separated by 0.125 inch thick stainless steel spacers. A 0.3125 inch hole was center tapped for beam passage. The purpose of the heat shield was to protect the quadrupole apparatus, particularly the hard solder joints, from the intense heat radiated from the oven. The oven was only 0.750 inch from the mouth of the quadrupole so space was at a premium.

The most persistent operational obstacle encountered has been the "shorting out" of the deflection system. Each component of the high voltage system was individually tested, and the problem was localized to the quadrupolar structure. The pumping speed inside the quadrupolar structure was insufficient to prevent a pressure build-up, and hence a gas discharge.[95] To this end, the heat shield was removed and the problem has been greatly alleviated.

3. Experimental Techniques

The chemicals used in these experiments are high purity commercially available compounds. Single crystals are preferable, though anhydrous salts are also quite satisfactory. Hydrated salts are generally baked overnight in an oven at approximately 110°C to remove the water. Water causes oven "bursts" which clog the orifice. Because of the hygroscopic nature of many metal halides, these compounds are constantly maintained under vacuum.

To avoid contamination by impurities, the sample ovens are scrubbed with an abrasive, washed with distilled water, dried, and then rewashed using ethyl alcohol prior to each experimental test. The interior of the oven chamber is also cleansed with ethyl alcohol between experiments. We

have discovered by experience that quadrupole pole pieces which have a thick deposit of beam material contribute to the gas discharge problem. Consequently, the quadrupole assembly is dismantled and washed with ethyl alcohol between experiments.

Each compound has been run under the following positions of the stopwire: large ball, small ball, thin rod, full rod, hole, full blockage. The change in signal with stopwire position acts as a check on beam deflection and refocusing, as opposed to simple scattering from quadrupole pole pieces.[96]

Each compound also has been run with a series of different deflecting voltages for various stopwire positions. Deflection voltages are systematically increased to the point where electrical breakdown occurs (~ 20 KV). Obviously a null deflecting voltage gives an indication of scattering. If the molecule has a permanent dipole moment, increasing the voltage yields an increased refocused signal for the beam.

Each compound has been studied over a range of temperature. Equilibrium conditions favor different vapor species at different temperatures.

Refocusing is always checked for the ionized species MX^+ as well as MX_2^+. The MX_2^+ signal is of the most interest as it is highly improbable that it could result from MX, the alkaline earth monohalide, which naturally has a dipole moment and deflects. The probable origin of the MX_2^+ ion is

$$MX_2 + e^- \longrightarrow MX_2^+ + 2e^- \quad ,$$

whereas the origin of MX^+ is much more in doubt. For example,

$$MX + e^- \longrightarrow MX^+ + 2e^-$$

or

$$MX_2 + e^- \longrightarrow MX^+ + X + 2e^- \quad .$$

All runs have been made with several thousand sample counts per second being fed to the multichannel analyzer. The total accumulated counts in the analyzer are at least 100,000 per channel. Each run lasts from 3 to 12 hours, depending on beam intensity. Periodic monitoring of the beam signal is made during each experiment. The hole position is used as a standard at all times, while the full blockage sliding beam stop is used as the null position.

Experiments involve adding counts alternately to two quadrants of the multichannel analyzer. In the first quadrant (sweep time 512 milliseconds) no deflection voltage is applied - this is the "control group". The second quadrant also has a sweep time of 512 milliseconds. A voltage pulse, 58 milliseconds in duration, is applied simultaneously with the start of the second quadrant sweep. During the remainder of that sweep, the voltage decays exponentially to the base line. By combining the counts collected in the two quadrants in a single picture, we obtain visual evidence of whether the applied voltage causes an increase in counts as is expected from deflection and subsequent refocusing of the beam.

VI. EXPERIMENTAL RESULTS

A. Introduction

A total of sixteen metal halide compounds have been studied using electric deflection. Lithium bromide (LiBr), zinc fluoride (ZnF_2), and cadmium bromide ($CdBr_2$) have been chosen as standards for these experiments. The nine alkaline earth dihalides (BaF_2, $BaCl_2$, $SrCl_2$, $SrBr_2$, SrI_2, CaF_2, $CaCl_2$, MgF_2, and $MgCl_2$) chosen for investigation are the borderline cases (between bent and linear gas phase structures) of this group. Lanthanum fluoride (LaF_3) is representative of a rare-earth trihalide to which our polarizable ion model could be readily applied. The europium dihalides ($EuCl_2$, $EuBr_2$, EuI_2) are quite similar to the alkaline earths and have not previously been studied using electric deflection spectroscopy.

The focusing data from the electric deflection experiments are presented in two different formats. The usual form is a table summarizing the changes in beam intensity when a deflection voltage is applied to the quadrupole electrostatic field. For our purposes,

$$I = \frac{(I_v - I_o)(10^2)}{I_t} \quad . \qquad \text{(VI-1)}$$

$\underline{I}$ is the percentage of the molecules refocused (or defocused); $\underline{I_v}$ is the beam intensity at voltage $\underline{V}$ for a given stopwire position; $\underline{I_o}$ is the beam intensity at a null voltage for the same stopwire position; and $\underline{I_t}$ is the "straight-through" beam intensity used for normalization. The second format is a visual display which is obtained from the oscilloscope trace output of individual experiments.

It is extremely difficult to assess focusing data quantitatively. Many variables contribute to discrepancies between measurements (e.g., varying source geometry, differing stopwire position, and nonreproducible deflection voltages and temperatures). An indication of the severity of this problem is the variation of as much as 50% in the normalized refocusing during successive experiments on a given mass fragment. Even less reproducibility occurs when experiments are not consecutive. Thus, we consider changes by more than a factor of 2 significant, and not just due to systematic errors. However, we are most interested in the distinction between polar and non-polar molecules as evidenced by refocusing or defocusing. The trend that the geometries of these molecules follow within a given series of compounds is important as it relates to our polarizable ion model.

We use different stopwire positions to ensure a proper focusing pattern. The positions which give the most characteristic patterns are the hole and the $1/16^{th}$ inch ball, so these are commonly used in our experiments.

The mass fragmentation patterns arising from molecular beams are given where pertinent. If several of the observed mass fragments originate solely from one parent species, nearly identical focusing characteristics are expected. Moreover, since most of these fragmentation patterns have already been observed in vaporization studies on these molecules, reproducibility indicates a similar beam composition and thus assists in identifying the parent species.

Each set of experiments has been performed over a temperature range. The lower temperature is that at which the minimum acceptable

beam intensity is available. The higher temperature often reflects the temperature at which the electric field begins to break down due to gas discharge. Although the refocusing pattern depends on temperature ($I \propto T^{2.0}$) as well as voltage, generally no correction is made for operating temperature. Our chief concern is the general trend, not the absolute deflection percentages, which are quite difficult to obtain.

B. Calibration Standards

1. Lithium Bromide (LiBr)

Lithium bromide has been used as the primary calibration standard because--1) it possesses a large permanent dipole moment[97] and thus can be used to determine the ability of the quadrupole electric field to deflect and refocus a polar molecule, and 2) both a polar parent species (LiBr) and a non-polar parent species (planar Li_2Br_2) are obtained from the same beam of molecules.[12] Consequently, the quadrupole electric field can be tested under a variety of operating conditions without varying other parameters. The LiBr molecule was studied after each experimental modification to ensure reproducible results.

Reagent grade lithium bromide was obtained from Mallinckrodt Chemical Works, Saint Louis, Missouri. LiBr is strongly deliquescent; samples were maintained under vacuum at all times. Prior to each experiment the LiBr was heated slowly to 100°C in a vacuum oven and held at that temperature overnight.

Over the mass range 20 amu to 100 amu, the four observed primary mass fragments are attributed to Li^+, Br^+, $LiBr^+$, and Li_2Br^+. The relative intensities of these fragments are 88:32:50:100. These ratios compare quite favorably with those given by Büchler *et al.*[12] (henceforth called BSK).

Thirty-two separate deflection experiments have been performed on LiBr over a temperature range of 1116°K to 1190°K. A typical spectrum of the $LiBr^+$ fragment is shown in Fig. VI-1. Figure VI-2 gives the refocusing percentage of the $LiBr^+$ fragment as a function of deflection voltage. These data agree quite well with the expected theoretical functionality ($I \propto V^{1.5}$). As the electric deflection experiments by Wharton, et al.[79] (henceforth called WBK) have shown, the monomeric LiBr molecule is highly polar and thus readily deflected and refocused. However, by extrapolating the curve in Fig. VI-2 and comparing the percentage refocused at a deflection voltage equivalent to that cited by BSK, we expect at least a 3-1/2 fold increase in refocusing with our system. We attribute this improvement to greater sensitivity as a result of our system geometry.

Both the fragments Li^+ and $LiBr^+$ deflect and refocus even at low deflection voltages; both arise from the polar parent molecule LiBr. On the other hand, Li_2Br^+ shows no tendency to refocus even at an applied voltage of 20 KV. Presumably the Li_2Br^+ fragment originates from the planar dimer Li_2Br_2. All the above conclusions are in qualitative agreement with the previous study of LiBr by BSK; thus the system is assumed to operate acceptably.

2. Zinc Fluoride (ZnF_2) and Cadmium Bromide ($CdBr_2$)

Originally, we chose the linear molecule zinc fluoride as a calibration standard. Using high sensitivity electric deflection spectroscopy, BSK studied ZnF_2 and reported no indication of refocusing. Lowenschuss et al.[55] later confirmed the linearity of ZnF_2 using

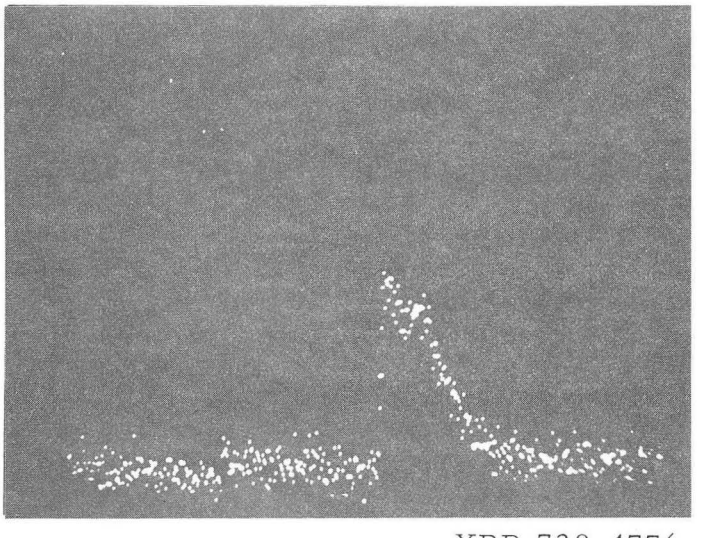

XBB 738-4776

Fig. VI-1. Compound: LiBr
Ionized Species: $LiBr^+$
Deflection Voltage: 12.0 KV
Stopwire: 1/8" ball

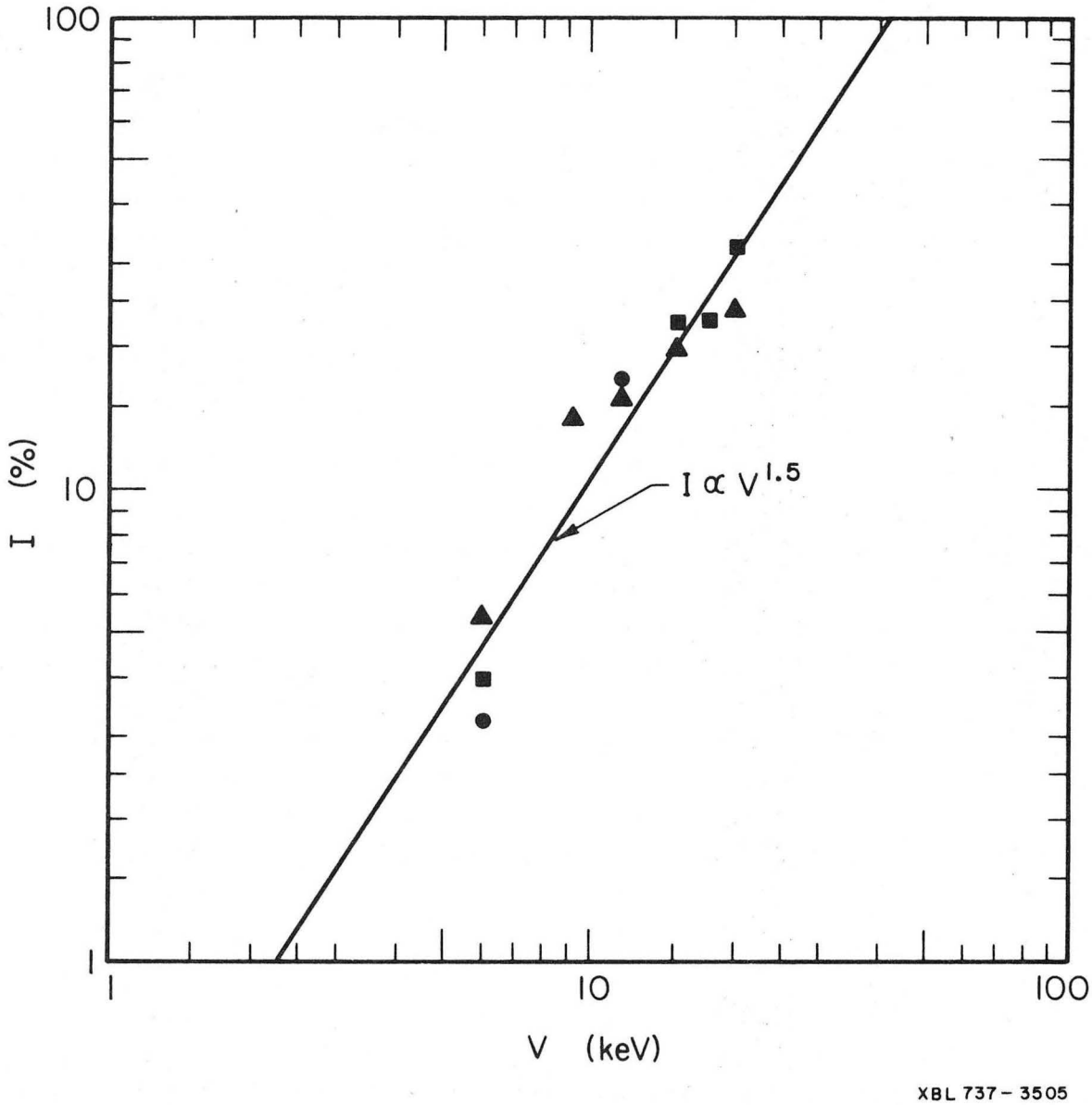

Fig. VI-2. Beam refocusing as a function of deflection voltage for LiBr.

matrix-isolation infrared absorption spectroscopy. However, using this same method to re-examine ZnF_2, Hastie et al.[54] interpreted their data as indicative of a slightly bent gas phase configuration (2α = 160 - 170°). Because of the latter study, cadmium bromide ($CdBr_2$) was then selected as a linear calibration standard in lieu of ZnF_2. $CdBr_2$ is definitely linear in the gas phase.[58]

We obtained anhydrous zinc fluoride powder, of 99% listed purity, from City Chemical Corporation, New York, New York, and bought anhydrous cadmium bromide crystals, of 99.9% listed purity, from Research Organic/Inorganic Chemical Corporation of Sun Valley, California. Since both compounds are highly hygroscopic, they were maintained under vacuum continuously. Approximately twenty-four hours prior to loading each sample oven, the compound was heated to $\sim$ 100°C.

In the infrared study of Hastie et al.,[54] no polymeric species of ZnF_2 were observed. Over the mass range of 30 amu to 420 amu, we find only the fragments Zn^+, ZnF^+, and ZnF_2^+, with relative intensities of < 1:100:15. The relative abundances of these fragments are in qualitative agreement with those of BSK. Similarly, no dimeric species are observed for $CdBr_2$ up to 500 amu. Only the fragments $CdBr^+$ and $CdBr_2^+$ are observed (relative intensities 40:100). Hence, both ZnF_2 and $CdBr_2$ are assumed to be monomeric within our experimental temperature range. The actual oven temperature could not be measured for either compound due to their high volatility. (The micro optical pyrometer has a low temperature limit of $\sim$ 1000°K.)

The eighteen separate deflection experiments performed on ZnF_2 can be divided into two distinct groups. The second of these was

necessitated by a major geometry change (replacement of the thoriated iridium filament). Voltages up to 18 KV give no indication of refocusing. Consequently, we conclude the F-Zn-F molecule is indeed linear in the gas state.

Fourteen deflection experiments were conducted using $CdBr_2$. No refocusing or defocusing is observed using deflecting voltages up to 20 KV, for either the hole or any of the ball positions. Typical spectra for $CdBr_2^+$ appear in Fig. VI-3. Thus, like ZnF_2, Br-Cd-Br has a linear geometry in the gas phase.

C. Alkaline Earth Dihalides

1. Barium Dihalides (BaF_2 and $BaCl_2$)

Of all the alkaline earths, barium fluoride (BaF_2) and barium chloride ($BaCl_2$) are certainly two of the most highly bent molecules. Two previous electric deflection studies by Klemperer and co-workers[12,79] have shown strongly refocused beams of both BaF_2 and $BaCl_2$. We have reinvestigated these molecules, not in the hope of gleaning any new structural information, but as a further test of the sensitivity of our apparatus.

Single crystals of barium fluoride (optical quality) were purchased from Optovac, Inc., North Brookfield, Massachusetts. Barium chloride was obtained as anhydrous crystals (reagent grade) from Allied Chemical Corp., Morristown, New Jersey. Prior to each experiment, the $BaCl_2$ was heated slowly to $\sim 150°C$ in an oven, and maintained at this temperature overnight. The BaF_2 crystals were broken into useable size chips and loaded directly into the source oven.

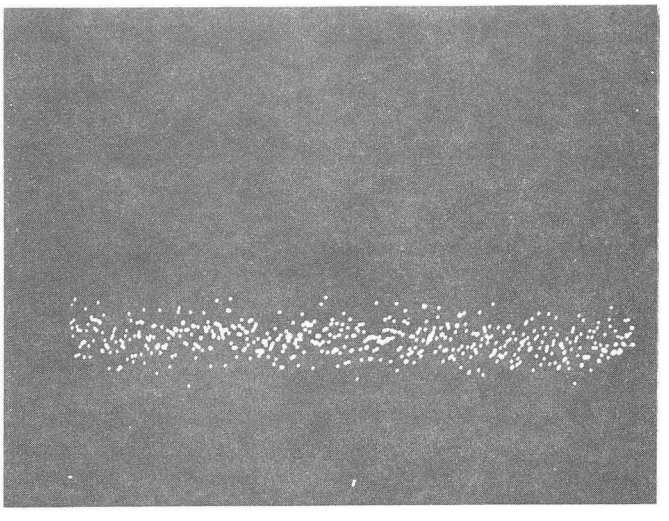

Fig. VI-3. Compound: $CdBr_2$
Ionized Species: $CdBr_2^+$
Deflection Voltage: 18.0 KV
Stopwire: Hole

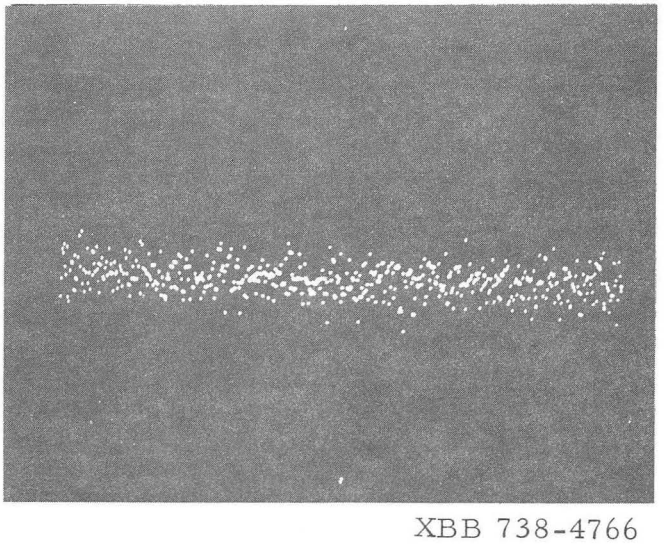

XBB 738-4766

Compound: $CdBr_2$
Ionized Species: $CdBr_2^+$
Deflection Voltage: 18.0 KV
Stopwire: 1/16" ball

Under Knudsen conditions, previous vaporization studies using mass spectrometry indicate that BaF_2 is a monomer over the temperature range 1232°K to 1505°K.[98,99] A similar situation has been postulated for $BaCl_2$ by Brewer et al.[100] Over the mass range 15 amu to 450 amu we have observed no evidence of polymeric fragments for either BaF_2 or $BaCl_2$. For BaF_2, the only observed fragments are Ba^+ and BaF^+ (their relative intensities are ∿ 40:100). These observations agree with the results of previous investigations.[12,98] Similarly, no parent fragment ($BaCl_2^+$) has been observed for $BaCl_2$. The Ba^+ and $BaCl^+$ peaks also show relative intensities of approximately 40:100.

Forty-two separate deflection experiments have been run on BaF_2 over the temperature range 1564°K - 1624°K. Both ionized species (BaF^+ and Ba^+) show sizable deflection and refocusing. The maximum applied voltage without arcing is 10 KV. For the BaF^+ species, a summary of the results appears in Table VI-1. A typical spectrum of BaF^+ is given in Fig. VI-4. The Ba^+ fragment shows a similar, although weaker, pattern. Obviously, this molecule deflects and refocuses quite strongly, even using relatively weak electric fields.

We have studied $BaCl_2$ in thirty separate deflection experiments over the temperature range 1457°K to 1532°K. The maximum deflection voltage used to investigate this molecule's behavior is 8.0 KV. As with BaF_2, the ionized species Ba^+ and $BaCl^+$ both exhibit sizable deflection and refocusing. A summary of the results for $BaCl^+$ appears in Table VI-2. A typical spectrum of $BaCl^+$ is given in Fig. VI-4. The Ba^+ fragment gives a nearly identical refocusing pattern. Hence, the $BaCl_2$ molecule is

Table VI-1. Focusing characteristics of BaF_2 (BaF^+ only)

Temperature (°K)	Stopwire Position	Percent Refocused (%)	Deflection Voltage (KV)
1570 ± 10	hole	0.00 ± 0.50	4.5
1620 ± 10	1/8" ball	14.75 ± 1.00	6.8
1620 ± 10	1/16" ball	11.10 ± 1.00	6.8
1570 ± 10	1/16" ball	8.29 ± 0.75	6.8
1595 ± 10	hole	0.00 ± 0.50	2.5
1620 ± 10	1/16" ball	22.00 ± 1.00	10.0
1595 ± 10	1/8" ball	9.10 ± 0.50	4.4
1570 ± 10	1/16" ball	4.50 ± 0.50	4.5
1595 ± 10	thin rod	4.00 ± 0.50	4.0
1620 ± 10	1/16" ball	5.50 ± 0.50	4.0

0 0 3 0 4 0 0 0 5 0 1

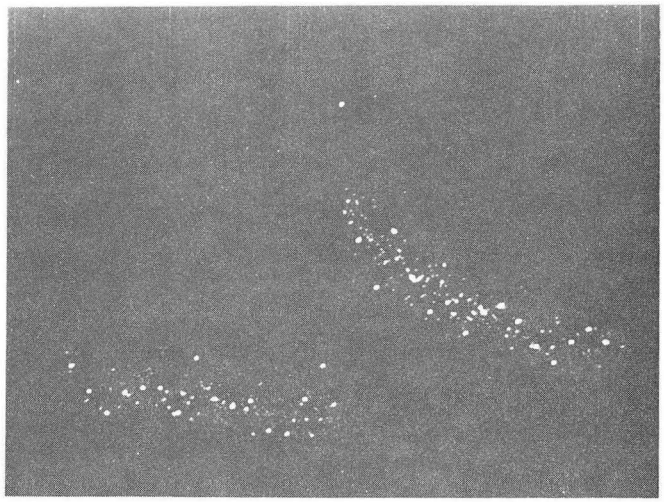

Fig. VI-4. Compound: BaF_2
Ionized Species: BaF^+
Deflection Voltage: 6.8 KV
Stopwire: 1/16" ball

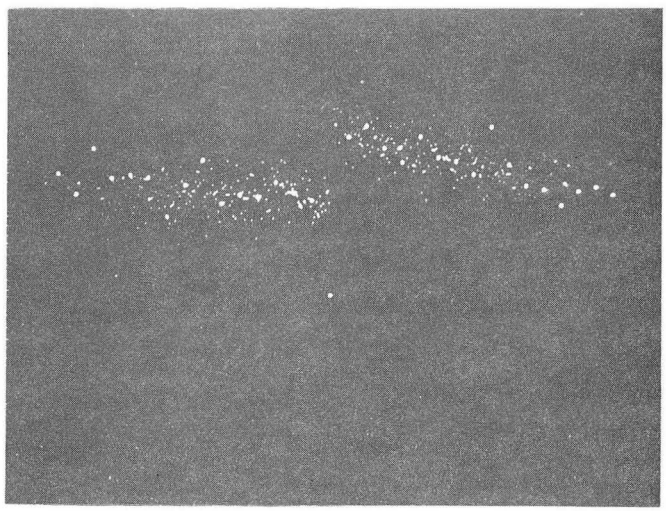

XBB 738-4767

Compound: $BaCl_2$
Ionized Species: $BaCl^+$
Deflection Voltage: 7.6 KV
Stopwire: 1/16" ball

Table VI-2. Focusing characteristics of $BaCl_2$ ($BaCl^+$ only)

Temperature (°K)	Stopwire Position	Percent Refocused (%)	Deflection Voltage (KV)
1480 ± 10	1/16" ball	24.00 ± 1.00	8.0
1460 ± 10	hole	0.00 ± 0.50	2.0
1460 ± 10	1/16" ball	21.15 ± 1.00	7.0
1460 ± 10	1/16" ball	7.32 ± 0.75	1.6
1460 ± 10	1/8" ball	7.50 ± 0.75	1.6
1480 ± 10	hole	0.00 ± 0.50	1.6
1510 ± 10	1/16" ball	15.64 ± 1.00	4.5
1510 ± 10	1/16" ball	14.02 ± 1.00	5.3
1480 ± 10	1/16" ball	16.93 ± 1.00	4.0

strongly polar. A large increase in sensitivity is indicated when these results are compared with those of WBK.

2. Strontium Dihalides ($SrCl_2$, $SrBr_2$, and SrI_2)

Previous experimental results[12,79] for the strontium dihalide geometries are surprising. BSK claim strontium chloride ($SrCl_2$) is bent, while strontium bromide ($SrBr_2$) is linear. These conclusions have broad ramifications for our polarizable ion model: To give the appropriate bending potential curves, the fitting parameter h must be chosen carefully. Therefore, the strontium dihalides, except the fluoride, have been studied to determine more definitively which are bent and which are indeed linear.

We obtained anhydrous strontium chloride crystals, anhydrous strontium bromide powder, and anhydrous strontium iodide powder (all of 99% listed purity) from Research Organic/Inorganic Chemical Corp. of Sun Valley, California. All of these compounds are highly hygroscopic, and, in addition, SrI_2 is uv photosensitive. Therefore, the samples were maintained under vacuum at all times. Twenty-four hours prior to each experiment the sample was heated slowly to $\sim 200°C$ in a vacuum oven.

Because of its photosensitivity, SrI_2 presented special problems. During sample preparation and oven loading this compound was exposed to a certain amount of light. It is unknown to what degree decomposition occurred as a result. On heating, relatively rapid decomposition is observed with I_2 gas as the major reaction product (I_2^+ is the primary fragment). SrI_2 is also seen; originally, the beam was quite weak. To alleviate this problem, the source oven was modified. The modified ovens

are identical to those previously described in Chapter V, except for a single 0.125 inch long channel welded behind the orifice. This type of directional oven is similar to those designed by Lovas.[8] Their purpose is to conserve source material while maintaining a steady beam intensity for several weeks. This type of oven has been used throughout subsequent experiments.

Previous sublimation studies have shown the monomer to be the principal vapor species over the strontium dihalide solids.[101,102] Over the mass range 30 amu to 500 amu, no fragments of polymeric origin have been observed for any of these molecules. For $SrCl_2$ and $SrBr_2$, both SrX^+ and SrX_2^+ are observed. In both cases, the SrX^+ ion is much more intense than the SrX_2^+ ion.

Twenty six separate deflection experiments have been performed on $SrCl_2$ over a range of 1481°K - 1738°K. Deflection voltages have ranged up to 7.2 KV. Both observed ionized species ($SrCl^+$ and $SrCl_2^+$) undergo deflection and refocusing. Typical spectra for $SrCl^+$ are given in Fig. VI-5. A summary of the results appears in Table VI-3. The small deflection for the "hole" position is believed due to arcing within the quadrupole and not to actual physical effects. The "shorting-out" problem was a persistent one, especially for the strontium dihalide compounds. Nevertheless, the deflection and refocusing pattern indicates that $SrCl_2$ is a bent molecule in the gas phase. This conclusion is in agreement with that of WBK, although we found it necessary to work at considerably higher temperatures than they did.

Sixty-two separate deflection experiments have been performed on $SrBr_2$ over a temperature range of 1222°K - 1732°K and a voltage

0 0 0 0 4 0 0 0 5 0 3

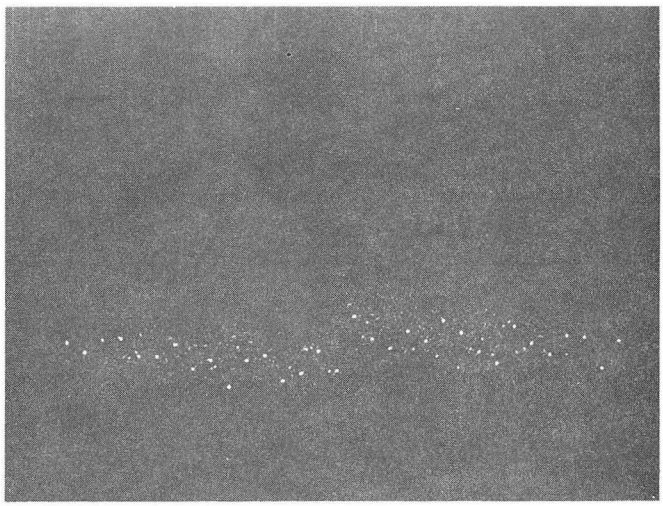

Fig. VI-5. Compound: $SrCl_2$
Ionized Species: $SrCl^+$
Deflection Voltage: 4.4 KV
Stopwire: 1/16" ball

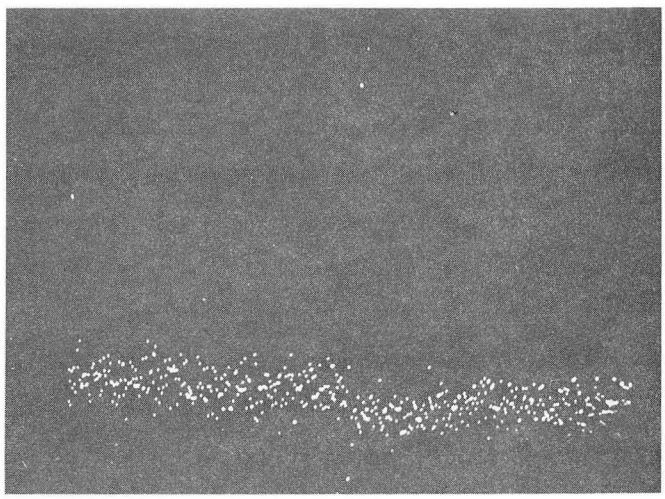

XBB 738-4768

Compound: $SrCl_2$
Ionized Species: $SrCl^+$
Deflection Voltage: 7.2 KV
Stopwire: Hole

Table VI-3. Focusing characteristics of $SrCl_2$

Mass Fragment	Temperature (°K)	Stopwire Position	Percent Refocused (%)	Deflection Voltage (KV)
$SrCl^+$	1565 ± 10	hole	-0.50 ± 0.50	4.8
"	1610 ± 10	hole	-1.09 ± 0.50	7.2
"	1610 ± 10	thin rod	2.75 ± 0.75	3.2
"	1565 ± 10	1/16" ball	1.99 ± 0.75	4.4
"	1565 ± 10	1/16" ball	2.38 ± 0.75	4.8
"	1610 ± 10	1/8" ball	4.21 ± 0.75	4.4
"	1565 ± 10	1/8" ball	2.31 ± 0.75	4.8
"	1565 ± 10	full rod	3.46 ± 0.75	3.6
$SrCl_2^+$	1481 ± 10	hole	-1.15 ± 0.50	6.6
"	1738 ± 10	1/16" ball	2.03 ± 0.75	4.2
"	1692 ± 10	1/16" ball	4.33 ± 0.75	4.9
"	1692 ± 10	1/8" ball	1.36 ± 0.50	3.4

range of 0. to 20.2 KV. Many of the earlier data, which were taken at higher temperatures than later data, have been discarded because of the arcing problem and the resultant extraneous signals in the spectra. Typical spectra of the $SrBr^+$ ion are given in Fig. VI-6. A summary of the results appears in Table VI-4. The validity of the small refocusing observed at 18 KV for the $SrBr^+$ fragment is uncertain. No arcing was detected at this voltage. Because of the higher temperatures necessary to form a suitable intensity of $SrBr_2^+$, 6.5 KV was the maximum voltage attainable without arcing. A weak defocused signal was observed at the "hole" position for both fragments.

Due to the difficulty in producing a beam of SrI_2 of reasonable intensity, only six separate deflection experiments were performed (over a temperature range of 1213°K - 1313°K and an applied voltage range of 0. to 10.5 KV). The fragment I_2^+ shows no refocusing or defocusing and hence implies a non-polar parent (presumably I_2 gas). On the other hand, SrI^+ shows no refocusing, but very slight defocusing at the "hole" position. Thus, SrI_2 is presumably linear.

3. Calcium Dihalides (CaF_2 and $CaCl_2$)

Previous experiments indicate that calcium fluoride (CaF_2) is slightly bent, while calcium chloride ($CaCl_2$) is linear.[12] We have examined these results with our increased sensitivity to determine if these two molecules do indeed have different gas phase structures.

We purchased single crystals of calcium fluoride (optical grade) from Research Organic/Inorganic Corp., Sun Valley, California. Anhydrous calcium chloride (reagent grade) was obtained from Matheson, Coleman, and

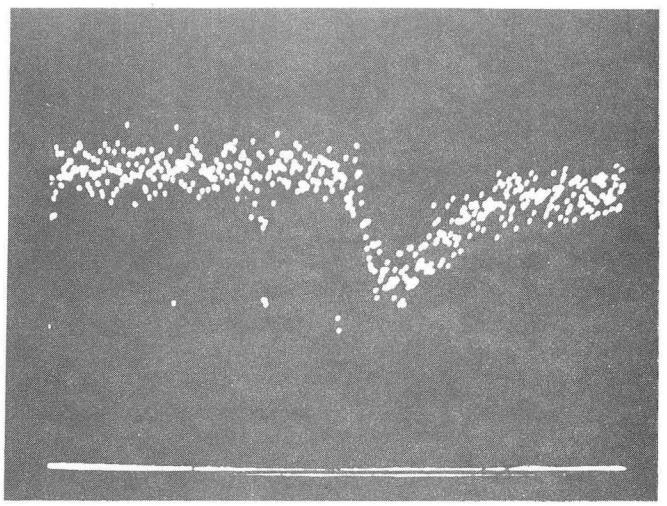

Fig. VI-6. Compound: $SrBr_2$
Ionized Species: $SrBr^+$
Deflection Voltage: 18.0 KV
Stopwire: Hole

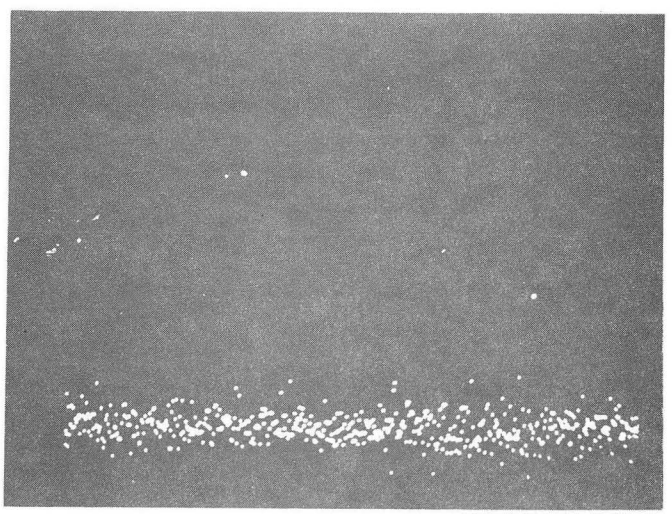

XBB 738-4769

Compound: $SrBr_2$
Ionized Species: $SrBr^+$
Deflection Voltage: 15.0 KV
Stopwire: 1/16" ball

Table VI-4. Focusing characteristics of $SrBr_2$

Mass Fragment	Temperature (°K)	Stopwire Position	Percent Refocused (%)	Deflection Voltage (KV)
$SrBr^+$	1470 ± 10	beam stop	0.00 ± 0.25	4.2
"	1249 ± 10	hole	-3.81 ± 0.69	15.0
"		hole	-5.68 ± 1.05	18.0
"	1470 ± 10	1/16" ball	0.00 ± 0.55	2.0
"		1/16" ball	0.00 ± 1.05	7.5
"	1222 ± 10	1/16" ball	0.00 ± 0.95	15.0
"	1249 ± 10	1/16" ball	0.41 ± 0.60	18.0
$SrBr_2^+$	1618 ± 10	beam stop	0.00 ± 0.25	2.2
"	1523 ± 10	hole	-3.19 ± 0.85	4.2
"	1723 ± 10	1/16" ball	0.00 ± 1.20	0.5
"	1523 ± 10	1/16" ball	-1.30 ± 0.85	4.6
"	1499 ± 10	1/16" ball	0.00 ± 1.05	6.3
"	1470 ± 10	full rod	0.00 ± 1.05	5.2

Bell, East Rutherford, New Jersey. Both compounds were maintained under vacuum prior to use. Twenty-four hours before introduction into the oven, the sample was heated slowly to ∿ 110°C and held at that temperature in a vacuum oven.

Previous mass spectroscopic studies under Knudsen conditions have shown that CaF_2 vaporizes as a monomer over the temperature range of 1242°K - 1669°K.[103] $CaCl_2$ is also thought to be monomeric upon vaporization.[100] Over the mass range of 25 amu to 340 amu no polymeric fragments have been observed. We do find the ions Ca^+, $CaOH^+$, CaF^+, and CaF_2^+ with approximate relative intensities of 40:<<1:50:100. The $CaOH^+$ fragment readily disappears on additional heating of the sample. For $CaCl_2$, only Ca^+ and $CaCl^+$ fragments are observed. Their relative intensities are 2:100. We could not detect any parent fragment ($CaCl_2^+$) even with a sensitivity of ∿ 0.02% of the intensity of the $CaCl^+$ peak.

A total of forty-two different deflection experiments have been performed on CaF_2 over the temperature range of 1161°K - 1642°K. The maximum deflection voltage was 18.0 KV. Both CaF^+ and CaF_2^+ undergo deflection and refocusing. Several typical spectra appear in Fig. VI-7. A complete summary of the results appears in Table VI-5. CaF_2 is a polar molecule since it is refocused for the "ball" position.

On the other hand, $CaCl_2$ has shown no refocusing or defocusing in any of eighteen separate deflection experiments performed over a temperature range of 1377°K - 1464°K. Because of arcing of the quadrupole and consequent extraneous signals, the maximum attainable voltage (without arcing) proved to be ∿ 11 KV. We conclude that $CaCl_2$ is a nonpolar

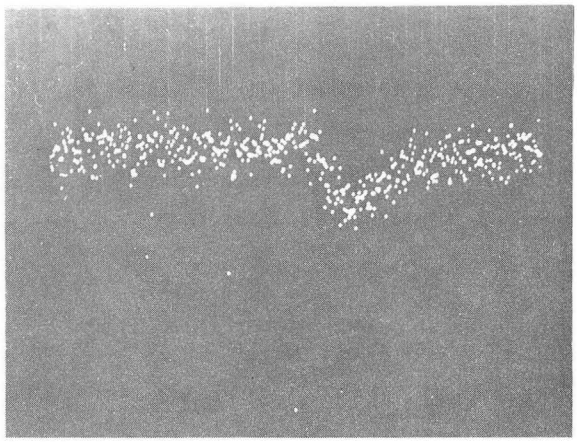

Fig. VI-7. Compound: CaF_2
Ionized Species: CaF^+
Deflection Voltage: 15.0 KV
Stopwire: Hole

Compound: CaF_2
Ionized Species: CaF^+
Deflection Voltage: 9.0 KV
Stopwire: 1/16" ball

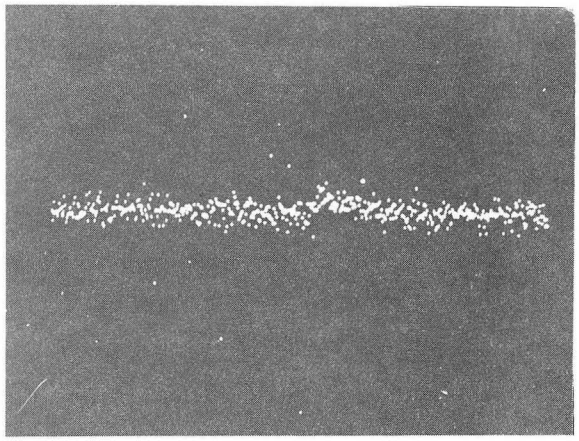

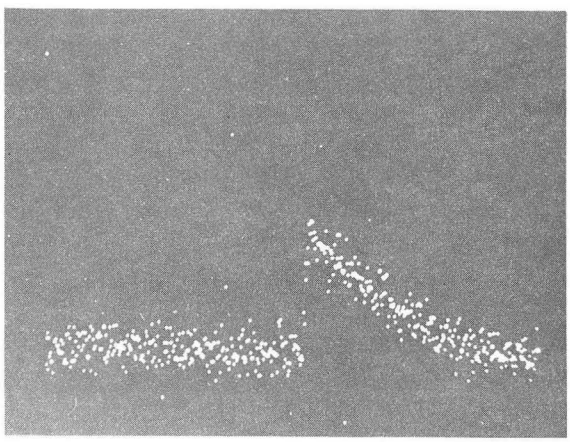

Compound: CaF_2
Ionized Species: CaF^+
Deflection Voltage: 15.0 KV
Stopwire: 1/16" ball

XBB 738-4775

Table VI-5. Focusing characteristics of CaF_2

Mass Fragment	Temperature (°K)	Stopwire Position	Percent Refocused (%)	Deflection Voltage (KV)
CaF_2^+	1161 ± 10	thin rod	1.00 ± 1.00	9.2
"	1161 ± 10	thin rod	2.23 ± 0.70	12.0
"	1161 ± 10	thin rod	4.03 ± 0.81	15.0
"	1210 ± 10	1/16" ball	3.44 ± 0.62	12.0
CaF^+	1585 ± 10	hole	-4.80 ± 0.70	15.0
"	1642 ± 10	hole	-2.78 ± 1.20	18.0
"	1585 ± 10	thin rod	2.00 ± 0.95	9.2
"	1446 ± 10	thin rod	2.95 ± 0.65	11.0
"	1616 ± 10	thin rod	2.30 ± 0.65	12.0
"	1585 ± 10	thin rod	4.43 ± 0.26	15.0
"	1558 ± 10	1/16" ball	0.94 ± 0.31	6.0
"	1558 ± 10	1/16" ball	1.48 ± 0.38	9.0
"	1446 ± 10	1/16" ball	3.50 ± 0.40	11.0
"	1514 ± 10	1/16" ball	2.53 ± 0.35	12.0
"	1616 ± 10	1/16" ball	3.85 ± 1.00	13.0
"	1511 ± 10	1/16" ball	4.90 ± 0.60	15.0
"	1476 ± 10	1/16" ball	10.00 ± 1.20	18.0

(hence linear) molecule. Both the CaF_2 and $CaCl_2$ data agree with the earlier work of WBK.

4. Magnesium Dihalides (MgF_2 and $MgCl_2$)

The gas phase geometry of magnesium fluoride (MgF_2) has been the subject of intense controversy for some time. Early electron diffraction experiments indicated that MgF_2 has a linear symmetric (C_{2v}) structure.[29,30] Similarly, BSK observed no refocusing of MgF_2 using electric deflection spectroscopy, and concluded that the molecule is nonpolar (linear) within the limits of their sensitivity.[12] Numerous infrared absorption studies have been performed on MgF_2 with both inconclusive and contradictory results.[34,36,37,49,72] This disagreement is caused by an inability to detect and/or assign the ν_1 vibration unambiguously. Theoretical arguments are no more helpful. Molecular orbital calculations by semiempirical methods yield an energy minimum at a bending angle of $\sim 140°$,[104,105] which is not consistent with the linear structure predicted by *ab initio* methods using Slater or Gaussian orbitals.[106,107] Therefore, we felt that examining MgF_2 using electric deflection spectroscopy with a very high sensitivity might resolve this geometry problem.

Ab initio calculations,[106,107] electron diffraction studies,[29,30] and infrared absorption experiments[35,38] generally agree that $MgCl_2$ is linear in the gas phase. However, at least one theoretical study[105] suggests a bent geometry for this molecule, as well as for MgF_2. Thus, we have also studied $MgCl_2$ to determine if there is any indication of refocusing.

We purchased a single crystal of magnesium fluoride (optical grade) from Research Organic/Inorganic Corp., Sun Valley, California. Since MgF_2 is nonhygroscopic, samples can be pulverized and introduced directly into the source ovens. Reagent-grade magnesium chloride crystals ($MgCl_2 \cdot 6H_2O$) were obtained from J. T. Baker Chemical Company, Phillipsburg, New Jersey. Twenty-four hours prior to introduction into the oven, the $MgCl_2$ sample was heated slowly to $\sim$ 110°C and held at that temperature in a vacuum oven. Further dehydration occurred during outgassing within the spectrometer.

Previous vaporization studies have shown that MgF_2 exists primarily as a monomer (> 99%) over the temperature range 1536°K - 2130°K.[99,108-111] We have covered the mass range from 20 amu to 200 amu. The only observed fragments containing magnesium are Mg^+, MgF^+, MgF_2^+, and $Mg_2F_3^+$; their relative intensities are 2:16:100:<1. This pattern agrees with previous data. Like MgF_2, $MgCl_2$ exists primarily as a monomer (> 99%) over the temperature range 987°K - 1413°K.[110-112] We have covered the mass range from 25 amu to 320 amu, and have observed only the fragments Mg^+, $MgCl^+$, and $MgCl_2^+$; their relative intensities are $\sim$ 1:20:100.

Thirty-eight separate deflection experiments have been performed on MgF_2 over a temperature range of 1134°K - 1738°K. Deflection voltages have ranged up to 19.0 KV. Typical spectra for MgF_2^+ are given in Fig. VI-8. A summary of results appears in Table VI-6. The small deflections for the "rod" and "ball" positions at higher voltages have a magnitude that is less than the experimental uncertainty. Therefore, MgF_2 is also a linear molecule.

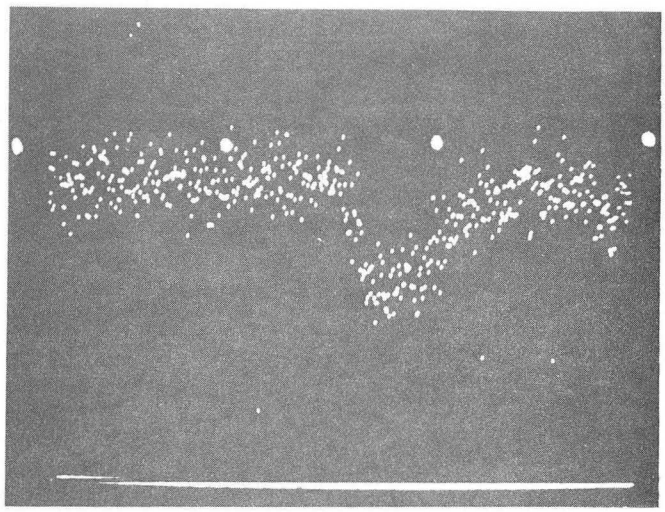

Fig. VI-8. Compound: MgF_2
Ionized Species: MgF_2^+
Deflection Voltage: 15.8 KV
Stopwire: Hole

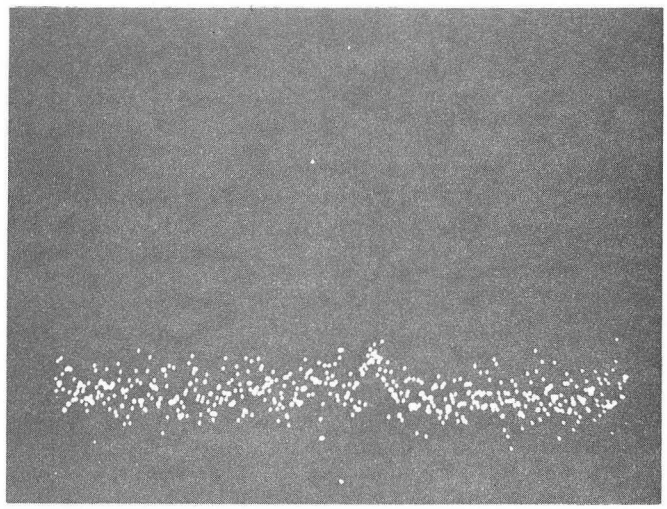

XBB 738-4770

Compound: MgF_2
Ionized Species: MgF_2^+
Deflection Voltage: 19.0 KV
Stopwire: 1/16" ball

Table VI-6. Focusing characteristics of MgF_2

Mass Fragment	Temperature (°K)	Stopwire Position	Percent Refocused (%)	Deflection Voltage (KV)
MgF_2^+	1577 ± 10	beam stop	0.00 ± 0.25	10.0
"	1577 ± 10	hole	-0.89 ± 0.46	10.0
"	1673 ± 10	hole	-1.26 ± 0.27	15.8
"	1145 ± 10	thin rod	0.00 ± 1.05	7.0
"	1178 ± 10	thin rod	0.00 ± 0.50	10.0
"	1228 ± 10	thin rod	0.52 ± 1.00	18.0
"	1374 ± 10	1/16" ball	0.00 ± 0.60	10.0
"	1178 ± 10	1/16" ball	-0.50 ± 0.60	14.0
"	1335 ± 10	1/16" ball	0.00 ± 0.75	15.0
"	1607 ± 10	1/16" ball	0.25 ± 0.65	16.0
"	1673 ± 10	1/16" ball	0.44 ± 0.50	17.0
"	1286 ± 10	1/16" ball	0.37 ± 1.00	18.0
"	1673 ± 10	1/16" ball	0.19 ± 0.24	19.0
"	1228 ± 10	1/8" ball	0.23 ± 0.80	15.0
MgF^+	1374 ± 10	hole	-0.10 ± 0.80	8.0
"	1286 ± 10	hole	-0.85 ± 0.50	15.0
"	1607 ± 10	1/16" ball	0.00 ± 0.40	8.0

Only six separate deflection experiments have been performed on $MgCl_2$. At voltages up to 18.0 KV, no refocusing or defocusing has been observed for any stopwire position. Once again, quadrupole arcing has been a persistent problem. Nevertheless, the spectra of $MgCl_2$ indicate that it is a linear molecule in the gas phase.

D. Rare Earth Halides

1. Lanthanum Fluoride (LaF_3)

We chose lanthanum fluoride (LaF_3) to introduce ourselves to the behavior of the rare earth halides within the framework of electric deflection experiments. Recent investigators have reached conflicting conclusions as to the gas phase geometry of LaF_3. Electron diffraction experiments have indicated that LaF_3 has a planar symmetric (D_{3h}) structure.[113] Using electric deflection in conjunction with velocity selection, Story[91] observed no indication of a permanent dipole moment. Thus, he also deduced that LaF_3 has a planar or very nearly planar structure. Wesley and DeKock[114] have examined the matrix-isolated infrared vibrational spectra of LaF_3 and assigned it a D_{3h} symmetry. Conflicting conclusions were drawn from a similar infrared study by Hauge *et al.*;[115] they assigned LaF_3 a non-centrosymmetric structure. In a recent study using molecular beam electric deflection spectroscopy, Kaiser *et al.*[116] obtained substantial refocusing indicative of polar distortions. An unambiguous assignment of the gas phase geometry of LaF_3 is also necessary for any future trihalide polarizable ion model.

We purchased anhydrous lanthanum trifluoride powder, of 99.9% listed purity, from K & K Products, Inc., Plainview, New York. Unlike

most of the alkaline earth dihalides, LaF_3 is not noticeably hygroscopic. Nevertheless, the LaF_3 was heated slowly to $\sim$ 150°C in a vacuum oven. The sample was maintained at this temperature at least twenty-four hours prior to loading an oven.

Previous mass spectroscopic studies under Knudsen conditions have shown that LaF_3 solid vaporizes primarily as monomer over the temperature range 1200°K - 1500°K.[117,118] Recently, however, Skinner and co-workers[119,120] have observed dimeric $La_2F_6(g)$ over the temperature range 1220°K - 1780°K. We have covered the mass range from 20 amu to 420 amu and have found no evidence of dimeric fragments (e.g. $La_2F_5^+$ or $La_2F_6^+$). The only fragments observed which contain lanthanum are La^+, LaF^+, and LaF_2^+. The relative intensities of these fragments are 20:34:100. This fragmentation concurs with the general trend observed for rare earth trifluorides by Kaiser et al.[116] This pattern, combined with the reduction studies quoted by the same authors, implies a monomeric LaF_3 parent molecule. However, no parent LaF_3^+ fragment could be detected even with a sensitivity of $\sim$ 0.03% of the intensity of the La^+ ion.

Eighteen separate deflection experiments have been performed on LaF_3 over a temperature range of 1434°K - 1511°K. A summary of the results appears in Table VI-7. To within the above accuracy, these results agree quite well with those of Kaiser et al.[116] The LaF^+ and LaF_2^+ fragments show very similar refocusing behavior, indicating that they indeed arise from the same parent species (LaF_3). Figure VI-9 shows typical spectra of LaF_3.

From the refocusing data of LaF_3, we conclude that LaF_3 indeed exhibits polar distortions. This implied net dipole moment, however,

Table VI-7. Focusing characteristics of LaF_3

Mass Fragment	Temperature (°K)	Stopwire Position	Percent Refocused (%)	Deflection Voltage (KV)
LaF^+	1480 ± 10	hole	-5.45 ± 0.72	16.0
"	1500 ± 10	1/16" ball	0.90 ± 0.29	16.0
"	1455 ± 10	1/16" ball	0.00 ± 0.50	8.0
LaF_2^+	1500 ± 10	hole	-2.60 ± 0.44	16.0
"	1455 ± 10	thin rod	1.95 ± 0.96	18.0
"	1455 ± 10	1/16" ball	0.00 ± 0.50	5.0
"	1455 ± 10	1/16" ball	0.00 ± 0.50	8.0
"	1455 ± 10	1/16" ball	1.02 ± 0.80	10.0
"	1480 ± 10	1/16" ball	1.07 ± 0.26	13.0
"	1455 ± 10	1/16" ball	1.34 ± 0.50	14.0
"	1500 ± 10	1/16" ball	1.00 ± 0.70	16.0
"	1455 ± 10	1/16" ball	2.35 ± 0.53	18.0

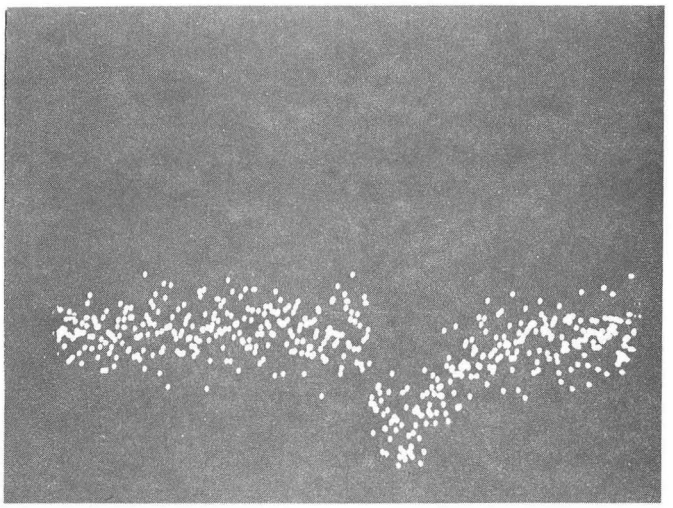

Fig. VI-9. Compound: LaF_3
Ionized Species: LaF_2^+
Deflection Voltage: 16.0 KV
Stopwire: Hole

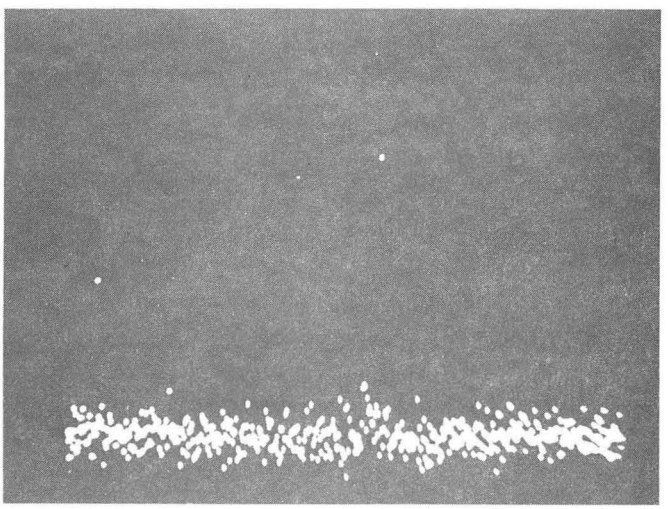

XBB 738-4771

Compound: LaF_3
Ionized Species: LaF_2^+
Deflection Voltage: 10.0 KV
Stopwire: 1/16" ball

is relatively small since refocusing occurs to only a slight degree. These conclusions agree with those of Kaiser et al.[116] and are consistent with the 117° F-La-F angle postulated by Hauge et al.[115]

2. Europium Dihalides ($EuCl_2$, $EuBr_2$, EuI_2)

The bonding of the rare-earth dihalides should be very similar to that of the alkaline earth dihalides. This should be especially true for the europium dihalides, since the ionic radius of Eu^{++} is 1.12 Å while that of Sr^{++} is 1.13 Å (see Chapter II). Thus it is of interest to see if the geometries of the europium dihalides are analogous to those of the strontium dihalides.

Previous studies on europium fluoride (EuF_2) using electric deflection[116] and matrix isolation infrared spectroscopy[40,63] indicate a strongly bent gas phase geometry (similar to that of SrF_2). During the course of our experiments, two geometry investigations were reported on europium chloride ($EuCl_2$) employing the matrix isolation technique.[40,63] However, the vibrational frequency assignments (especially ν_1 and ν_2) in these studies are ambiguous because of matrix effects of unknown magnitude. No structural or vibrational information was available for either europium bromide ($EuBr_2$) or europium iodide (EuI_2) prior to this study.

We purchased anhydrous europium trichloride ($EuCl_3$), of 99.9% listed purity, from Research Organic/Inorganic Chemical Corp., Sun Valley, California. We obtained anhydrous europium tribromide ($EuBr_3$) and europium triiodide (EuI_3), each of 99.95% listed purity, from Bram Metallurgical, Philadelphia, Pennsylvania. The europium dihalides are prepared using thermal decomposition of these anhydrous trihalides.

$$2\ EuX_3(s) \rightarrow 2\ EuX_2(s) + X_2(g) \quad . \qquad \text{(VI-2)}$$

Ease of reduction at elevated temperatures increases in the series $Cl^- - Br^- - I^-$.[121,122] This reduction is accomplished in situ during each experiment. The evolution of halogen gas is readily monitored with the mass fragment X_2^+.

To confirm the spectra obtained using the reduction of the trihalide, we purchased europium chloride ($EuCl_2$), of 99.9% listed purity, from Electronic Space Products, Los Angeles, California. The two sets of fragmentation patterns are identical to within experimental accuracy. Moreover, in each case, the residue remaining in the ovens after experimentation has the white color characteristic of $EuCl_2$. No significant difference in deflection patterns is observed between $EuCl_2$ and the $EuCl_3/EuCl_2$ system. Therefore, the reduction method was deemed suitable for preparation of the other europium dihalides.

All of the europium dihalides are known to vaporize congruently according to [123-126]

$$EuX_2(l) \rightarrow EuX_2(g) \quad .$$

The temperature ranges of these mass spectroscopic studies are 1135°K - 1569°K, 1185°K - 1568°K, and 1086°K - 1395°K for the chloride, bromide, and iodide, respectively.

Other than chloride fragments ($Cl^+ > Cl_2^+ > Cl_3^+ > Cl_4^+$), only the ions Eu^+, $EuCl^+$, and $EuCl_2^+$ are observed over the mass range 20 amu to 450 amu for $EuCl_3/EuCl_2$ or pure $EuCl_2$. This fragmentation pattern is

similar to that seen by Hastie et al.[123] and Hariharan and Eick.[124] The relative intensities we observed are 100:100:45. No evidence of polymeric species or of the "parent" $EuCl_3$ molecule is observed even with a sensitivity of ∿ 0.01% of the $EuCl^+$ intensity.

Thirty separate deflection experiments have been performed on $EuCl_2$ and $EuCl_3/EuCl_2$ over a temperature range 1231°K - 1612°K. Deflection voltages have ranged up to 18.0 KV. All three ionized species (Eu^+, $EuCl^+$, and $EuCl_2^+$) undergo deflection and refocusing. Typical $EuCl^+$ spectra are given in Fig. VI-10. A summary of results appears in Table VI-8. Not only does the focusing pattern of $EuCl_2$ confirm the nonlinearity of the molecule in the gas phase, but also the pattern is very similar to that exhibited by $SrCl_2$ (see Table VI-3).

For the $EuBr_3/EuBr_2$ system, the only fragments observed which contain europium are Eu^+, $EuBr^+$, and $EuBr_2^+$. The relative intensities of these fragments are 47:100:12; this fragmentation pattern agrees very well with that found by Haschke and Eick.[125] No evidence of polymeric species or of the "parent" $EuBr_3$ molecule is observed. This follows the pattern established for other rare earth di- and trihalides.

Twenty-two separate deflection experiments have been performed on $EuBr_3/EuBr_2$ over a temperature range of 1330°K - 1505°K. Deflection voltages have ranged up to 18.0 KV. Typical $EuBr^+$ spectra are given in Fig. VI-11. A summary of the results appears in Table VI-9. The focusing characteristics of $EuBr_2$ are very similar to those of $SrBr_2$ under similar conditions. Once again strong defocusing is observed for the "hole" position. Refocusing at the "ball" position is at best uncertain.

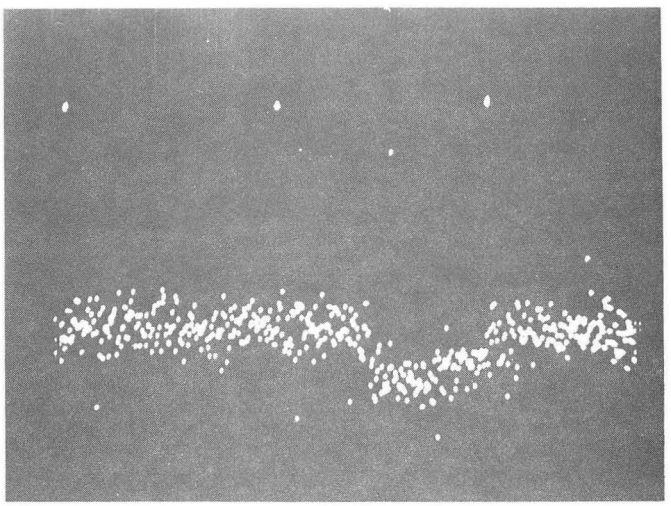

Fig. VI-10. Compound: $EuCl_3/EuCl_2$
Ionized Species: $EuCl_2^+$
Deflection Voltage: 12.0 KV
Stopwire: Hole

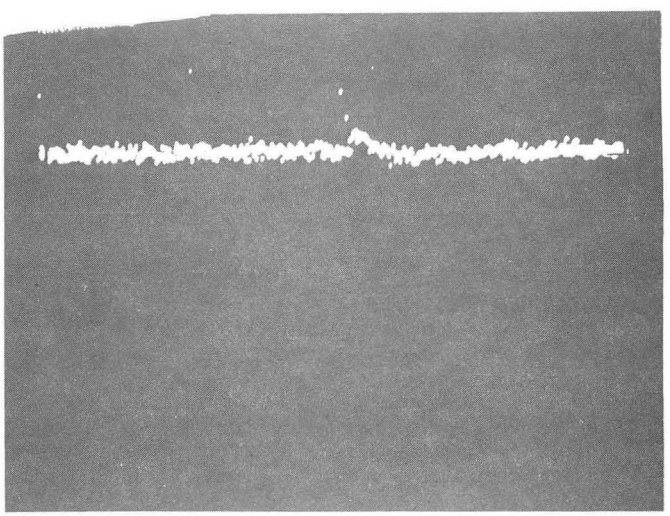

XBB 738-4772

Compound: $EuCl_2$
Ionized Species: $EuCl_2^+$
Deflection Voltage: 11.0 KV
Stopwire: 1/16" ball

Table VI-8. Focusing characteristics of $EuCl_2$ ($EuCl^+$ only)

Temperature (°K)	Stopwire Position	Percent Refocused (%)	Deflection Voltage (KV)
1268 ± 10	hole	0.00 ± 1.00	8.0
1470 ± 10	hole	-4.00 ± 0.65	12.0
1525 ± 10	hole	-4.51 ± 0.90	15.0
1268 ± 10	1/16" ball	0.00 ± 0.50	5.0
1388 ± 10	1/16" ball	2.11 ± 0.75	10.0
1609 ± 10	1/16" ball	1.36 ± 0.65	11.0
1428 ± 10	1/16" ball	2.25 ± 0.65	12.0
1231 ± 10	1/16" ball	3.92 ± 0.80	13.0
1609 ± 10	1/16" ball	3.88 ± 0.60	14.0
1388 ± 10	1/16" ball	5.89 ± 0.65	15.0
1349 ± 10	1/16" ball	6.69 ± 0.75	16.0
1470 ± 10	1/16" ball	5.64 ± 0.75	17.0
1268 ± 10	1/16" ball	4.28 ± 0.95	18.0

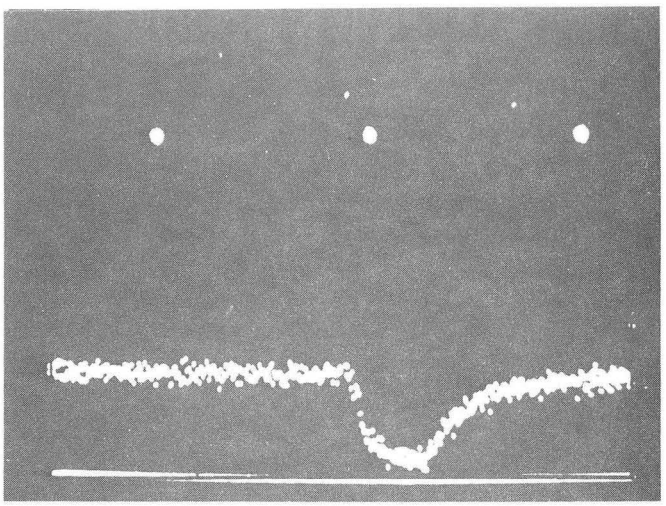

Fig. VI-11. Compound: $EuBr_3/EuBr_2$
Ionized Species: $EuBr^+$
Deflection Voltage: 18.0 KV
Stopwire: Hole

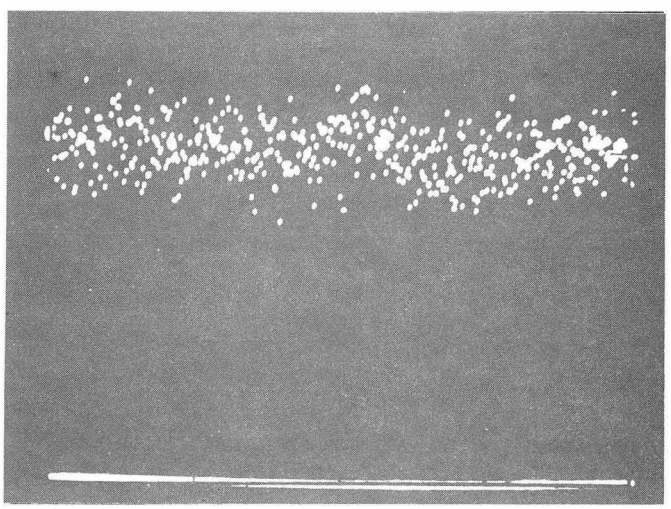

XBB 738-4773

Compound: $EuBr_3/EuBr_2$
Ionized Species: $EuBr_2^+$
Deflection Voltage: 14.0 KV
Stopwire: 1/16" ball

Table VI-9. Focusing characteristics of $EuBr_2$

Mass Fragment	Temperature (°K)	Stopwire Position	Percent Refocused (%)	Deflection Voltage (KV)
$EuBr_2^+$	1497 ± 10	hole	-2.86 ± 0.79	10.0
"	1497 ± 10	1/16" ball	0.02 ± 0.37	12.0
"	1497 ± 10	1/16" ball	0.27 ± 0.75	14.0
$EuBr^+$	1431 ± 10	hole	-1.35 ± 0.57	10.0
"	1353 ± 10	hole	-3.67 ± 0.67	15.0
"	1418 ± 10	hole	-5.14 ± 0.48	18.0
"	1418 ± 10	1/16" ball	0.00 ± 0.18	9.0
"	1397 ± 10	1/16" ball	0.31 ± 0.51	12.0
"	1397 ± 10	1/16" ball	0.33 ± 0.65	15.0
"	1431 ± 10	1/16" ball	0.34 ± 0.32	16.5
"	1418 ± 10	1/16" ball	0.71 ± 0.38	18.0

For the EuI_3/EuI_2 system, the mass spectrometric analysis of the effusate indicates I^+, Eu^+, EuI^+, EuI_2^+ in the respective ratios of 20:49:100:39. This fragmentation pattern concurs with that observed during previous vaporization studies.[126] It also agrees with the general pattern we observed throughout the europium dihalide series: $EuX^+ > Eu^+ > EuX_2^+$. No attempt was made to observe EuI_3^+ since it occurs outside our mass range. However, Hariharan and Eick[126] found no gaseous EuI_3 present in their investigations. A similar conclusion is indicated from our other EuX_3/EuX_2 system studies. The residue retrieved from our source ovens after experimentation has a greenish color, characteristic of EuI_2 solid.

Eighteen separate deflection experiments have been performed on EuI_3/EuI_2 over a temperature range of 1088°K - 1260°K. Deflection voltages have ranged up to 18.0 KV. Typical EuI_2 spectra are given in Fig. VI-12. A summary of the results appears in Table VI-10. Like SrI_2, EuI_2 shows no refocusing of magnitude greater than the background. Thus, we conclude EuI_2 is linear in the gas phase. The strong defocusing pattern observed at the hole position is similar to observations for the other europium dihalides.

E. Summary

Using the "hole" position at high voltages (generally > 10.0 KV), we observe large defocused signals for the alkaline earth dihalides with weak bending potentials. The defocusing is assumed to result from polarization of the bending moment. This polarization is possible because of the combination of large bond moments and flat bending potentials in these alkaline earth dihalide molecules. Presumably, highly bent compounds

0 0 0 0 4 0 0 0 5 1 2

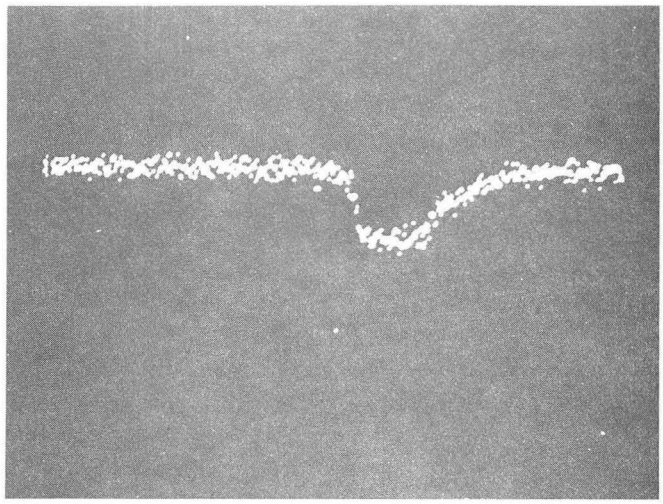

Fig. VI-12. Compound: EuI_3/EuI_2
Ionized Species: EuI_2^+
Deflection Voltage: 18.0 KV
Stopwire: Hole

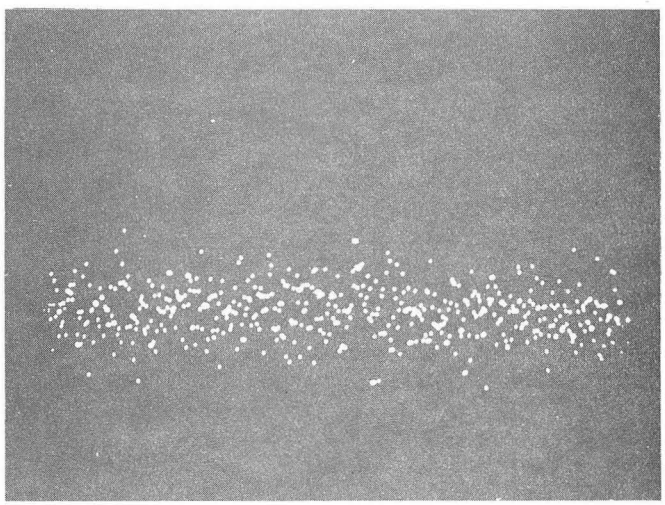

XBB 738-4774

Compound: EuI_3/EuI_2
Ionized Species: EuI_2^+
Deflection Voltage: 18.0 KV
Stopwire: 1/16" ball

Table VI-10. Focusing characteristics of EuI_2

Mass Fragment	Temperature (°K)	Stopwire Position	Percent Refocused (%)	Deflection Voltage (KV)
EuI^+	1101 ± 10	hole	-5.67 ± 0.58	15.0
"	1190 ± 10	1/16" ball	0.00 ± 0.50	5.0
"	1217 ± 10	1/16" ball	0.00 ± 0.50	10.0
"	1190 ± 10	1/16" ball	0.36 ± 0.53	12.0
"	1217 ± 10	1/16" ball	0.30 ± 0.36	15.0
"	1190 ± 10	1/16" ball	0.45 ± 0.40	18.0
EuI_2^+	1101 ± 10	hole	-3.39 ± 0.40	15.0
"	1217 ± 10	hole	-4.75 ± 0.45	18.0
"	1245 ± 10	1/16" ball	0.14 ± 0.49	8.0
"	1101 ± 10	1/16" ball	0.00 ± 0.50	12.0
"	1101 ± 10	1/16" ball	0.48 ± 0.96	15.0
"	1245 ± 10	1/16" ball	0.25 ± 0.46	18.0

such as BaF_2 and $BaCl_2$ would also exhibit this effect if they were studied at higher voltages. On the other hand, $CdBr_2$ was studied at voltages up to 20.0 KV and no defocusing was observed! $CdBr_2$ has a much steeper bending potential (see Appendix A-2); consequently, bending moment polarization is much less likely. Thus, the defocusing or lack thereof gives no implication as to the existence of an intrinsic dipole moment.

On the other hand, refocusing of molecules at the "ball" and "rod" positions indicates the existence of a permanent dipole moment, and, consequently, a bent equilibrium configuration for the symmetric metal dihalides. We observe this refocusing for the following compounds: BaF_2, $BaCl_2$, $SrCl_2$, CaF_2, and $EuCl_2$. Similarly, since LaF_3 shows refocusing, it has a permanent dipole moment and thus a pyramidal (as opposed to planar) equilibrium geometry. Conversely, the absence of any refocused beam is indicative of no detectable net dipole moment (a linear equilibrium geometry for MX_2 compounds). Our results show that $SrBr_2$, SrI_2, $CaCl_2$, MgF_2, $MgCl_2$, ZnF_2, $CdBr_2$, $EuBr_2$, and EuI_2 are linear compounds by this criterion. A summary of the geometries deduced and implied by this work for the alkaline earth dihalides and the europium dihalides appears in Table VI-11.

Table VI-11. Geometry of the alkaline earth and europium dihalides

$\overline{BeF_2}$	$\overline{BeCl_2}$	$\overline{BeBr_2}$	$\overline{BeI_2}$
$\overline{MgF_2}$	$\overline{MgCl_2}$	$\overline{MgBr_2}$	$\overline{MgI_2}$
$\widehat{CaF_2}$	$\overline{CaCl_2}$	$\overline{CaBr_2}$	$\overline{CaI_2}$
$\widehat{SrF_2}$	$\widehat{SrCl_2}$	$\overline{SrBr_2}$	$\overline{SrI_2}$
$\widehat{BaF_2}$	$\widehat{BaCl_2}$	$\widehat{BaBr_2}$	$\widehat{BaI_2}$
$\widehat{EuF_2}$	$\widehat{EuCl_2}$	$\overline{EuBr_2}$	$\overline{EuI_2}$

$\widehat{}$ = bent equilibrium geometry

$\overline{}$ = linear equilibrium geometry

VII. CONCLUSIONS

Despite significantly increased sensitivity, our reinvestigation of the alkaline earth dihalides revealed no disagreement with prior electric deflection studies conducted by Klemperer and co-workers.[12,79] Even greater precision was hampered by persistent electrical discharges at high deflection voltages. Consideration of electrical insulation should be of prime importance in the design of future electric deflection systems. However, our work suggests that voltages in excess of 20.0 KV may be of dubious value.

Contradictions remain between our experimental conclusions and those from matrix-isolation infrared spectroscopic studies. For example, we believe that the isolated molecule MgF_2 is indeed linear, but that it has a very small deformation barrier to external perturbations such as the matrix itself. Recently, this conclusion has been supported by the calculations of Astier et al.[127] Similar conflicts with electric deflection results may arise if the matrix method is applied to other anharmonic linear molecules, such as $CaCl_2$, $SrBr_2$, and $EuBr_2$. Otherwise, our experimentally determined geometries agree with those available from other techniques.

The previously unreported gas phase geometries of $EuBr_2$ and EuI_2 are shown to be linear. These results parallel those for $SrBr_2$ and SrI_2, as expected. Our results agree with previously reported data that $EuCl_2$ is a bent compound (like $SrCl_2$) in the gas phase. The experimental behavior of the strontium and europium analogs is remarkably similar. It would be of interest to determine if the remaining rare earth dihalides resemble their alkaline earth dihalide counterparts.

The above metal dihalide geometries (see Table VI-12) agree with those predicted by our polarizable ion model (see Tables VI-2 and VI-6). The bond angles and bending frequencies calculated from this model compare quite favorably with available high temperature infrared spectroscopic data. The agreement between our predictions and matrix-isolation infrared spectroscopic data is not nearly as good. We believe matrix effects may account for these discrepancies. The linear polarizable ion model provides further molecular parameter predictions for the alkaline earth dihalides. The agreement with experimental internuclear bond lengths is excellent. The predicted stretching frequencies and force constants give reasonable agreement with "known" experimental values.

Certainly both polarizable ion models predict the proper trends throughout a series of compounds within the metal dihalides. These predicted values for molecular parameters should give a good starting point for further calculations and experimental investigations. We conclude that the "ionic model" concept provides a reasonable representation of the interactions within metal dihalide molecules such as the alkaline earth, Group II-b, transition metal and europium dihalides.

Although the algebraic complexity increases markedly upon adding more atoms, the polarizable ion model can be applied to metal trihalides. Currently, we are investigating the feasibility of such a model for predicting the properties of the lanthanum, yttrium and scandium trihalides. Since little experimental data is available for these compounds, electric deflection experiments on the trifluorides and trichlorides of these metals are contemplated.

ACKNOWLEDGEMENTS

I am most grateful to Professor Kenneth Street, Jr. for his guidance and encouragement.

Many thanks are due to Dr. Alvin J. Hebert for his interest and assistance in the experimental aspects of this work. My association with Dr. Craig D. Hollowell has been a most rewarding intellectual and personal experience. I would also like to thank former members of the molecular beam group (Dr. Carlos A. Melendres, Dr. Troy L. Story, and James D. Dake) for their assistance in initiating this project.

Michiyuki Nakamura and John A. Mendes provided invaluable advice and help in solving electronic problems.

Finally, I am especially indebted to my wife, Joyce, who has lent her support in innumerable ways throughout this research.

This work was performed under the auspices of the U. S. Atomic Energy Commission.

APPENDICES

APPENDIX A-1

a. Program **IMHØL

(The ** digits are replaced by FL for the fluorides, CL for the chlorides, BR for the bromides, or IØ for the iodides.)

Purpose:

The program **IMHØL is designed to calculate, by use of our polarizable ion model (Chapter II), the total bending potential energy of the metal dihalides, along with various contributory repulsive and attractive portions, as a function of bending angle.

Input Data:

The data cards that are used to describe the polarizable ion model input data are the following:

Card 1 (Format F8.2, F8.5, F8.2)

RPLS = ionic radius of metal (r_+) in Angstroms (Å).

AQDP = dipole polarizability of metal ion (α_D) in Angstroms cubed ($Å^3$).

D = metal-halide equilibrium internuclear distance (ℓ) in Angstroms (Å).

Card 2 (Format F8.0, F8.3)

ARPL = halide-halide repulsive pre-exponential (A) in electron volts-Angstroms (eV-Å) or electron volts (eV).

EXRP = halide-halide repulsive decay constant (ρ) in Angstroms (Å).

Card 3 (Format 3A10, 2F10.5, F10.6, F5.0, F7.4)

CN1, CN2, CN3

= metal dihalide compound name (maximum of thirty letters and blanks).

ADL = lower limit of bending angle (θ) in degrees (°), generally 0° or linear configuration.

ADG = upper limit of bending angle ($\underline{\theta}$) in degrees (°), generally 50° (i.e., a bent configuration with X-M-X angle (2α) of 80°).

C = deformation constant ($\underline{k}$).

Q = $\underline{d}$-shell filling parameter ($\underline{q}$).

H = proportionality constant ($\underline{h}$).

Library Subroutines:

None.

Output:

Page 1 (Format 3A10, 2F10.5, F5.0)

CN1, CN2, CN3

= metal dihalide compound name supplied on data card 3.

ADL = lower limit of bending angle supplied on data card 3.

ADG = upper limit of bending angle supplied on data card 3.

Q = $\underline{d}$-shell filling parameter supplied on data card 3.

Page 2 (Format 2E15.5, 4E15.4, F12.4; Format 2F10.2, F10.5, F10.6, F10.4, F10.6, F10.0, F10.3)

VTOT = total bending potential energy ($\underline{V}$) in electron volts (eV).

VRPL = repulsive potential energy ($\underline{\phi_r}$) in electron volts (eV).

V = electrostatic potential energy ($\underline{\phi_{ei}}$) in electron volts (eV).

CGCG = charge-charge interaction energy in electron volts (eV).

CGDP = charge-positive dipole interaction energy in electron volts (eV).

CGQP = charge-positive quadrupole interaction energy in electron volts (eV).

DEGR = bending angle ($\underline{\theta}$) in degrees (°).

(All the above quantities are printed for each bending angle ($\underline{\theta}$) between ADL and ADG in increments of <u>two</u> degrees.)

RPLS = ionic radius of metal supplied on data card 1.

D = metal-halide equilibrium internuclear distance supplied on data card 1.

AQDP = dipole polarizability of metal ion supplied on data card 1.

AQQP = spherical conductor quadrupole polarizability of metal ion (α_Q) in Angstroms to the fifth power ($Å^5$).

H = proportionality constant supplied on data card 3.

C = deformation constant supplied on data card 3.

ARPL = halide-halide repulsive pre-exponential supplied on data card 2.

EXRP = halide-halide repulsive decay constant supplied on data card 2.

Page 3 (Format 4E20.5)

Y(J) = total bending potential energy (V) in ergs.

X(J) = displacement coordinate ($r\theta$) in centimeters (cm).

Y1(J) = Y(J) in relative ergs.

X2(J) = $[X(J)]^2$ in centimeters squared (cm^2).

(All the above quantities are printed for each bending angle (θ) between ADL and ADG in increments of <u>two</u> degrees.)

<u>Options</u>:

PUNCH --- Program punches one card associated with each set of values printed on page 3 of the output.

Rows 1-10; Y1(J) in Format E10.3.

Rows 11-20; X2(J) in Format F10.8.

These cards, in turn, are used as input data for the program <u>LSQVMT</u> (See Appendix A-1c).

```
      PROGRAM FLIMHOL (INPUT,OUTPUT,PUNCH)
      DIMENSION X(100), Y(100), Y1(100), X2(100)
      READ 1, RPLS, AQDP, D
    1 FORMAT (F8.2, F8.5, F8.2)
      READ 41, ARPL, EXRP
   41 FORMAT (F8.0, F8.3)
      READ 300, CN1, CN2, CN3, ADL, ADG, C, Q, H
  300 FORMAT (3A10, 2F10.5, F10.6, F5.0, F7.4)
      DEGR=ADL
      PRINT 401
  401 FORMAT (1H1,54H COMPOUND NAME            MINIMUM ANGLE MAXIMUM ANGLE
     1 Q //////)
      PRINT 402, CN1, CN2, CN3, ADL, ADG, Q
  402 FORMAT (3A10, 2F10.5, F5.0)
      AQQP=Q*((AQDP**0.3333)**5.0)
      CGSQ=(23.04)/1.60209
      PRINT 8
    8 FORMAT (1H1,102H TOTAL POTENTIAL REPULSIVE POT. ATTRACTIVE POT. CH
     1ARGE-CHARGE CHARGE-DIPOLE CHARGE-QUADRUPOLE  ANGLE  ////)
      I=1
   31 TH=DEGR/57.2957795
      X(I)=(D*DEGR*0.017453293*1.0E-08)
      X2(I)=(X(I)**2.)
      ANGT=SIN(TH)**2
      ANGF=ANGT**2
      ANGS=ANGT*ANGF
      B=(CGSQ/(-D))
      CGCG=B*(4.+4.*C*ANGT-1./(2.*COS(TH))-(C*ANGT)/(2.*COS(TH)))
      CGDP=B*(AQDP/D**3)*(2.*ANGT+8.*C*ANGF)
      CGQP=B*(AQQP/D**5)*(2.+(12.*C-6.)*ANGT+(6.-36.*C)*ANGF+36.*C*ANGS)
      V=CGCG+CGDP+CGQP
      DPRM=D*(1-C*ANGT)
      R=2*DPRM*COS(TH)
      VRPL=(ARPL/(R**2))*(EXP(-(R)/EXRP))
      VTOT=V+VRPL
      Y(I)=(VTOT*1.60209E-12)
      IF (DEGR) 102,103,102
  103 YO=VTOT
  102 CONTINUE
      Y1(I)=VTOT-YO
      I=I+1
      PRINT 61, VTOT, VRPL, V, CGCG, CGDP, CGQP, DEGR
   61 FORMAT (2E15.5, 4E15.4, F12.4)
      DEGR=DEGR+2.0000
      IF (DEGR-ADG) 31, 31, 11
   11 CONTINUE
      PRINT 28
   28 FORMAT (21(/)85H IONIC RADII RADIUS DIPOLE POL. QUADRUPOLE POL. H
     1    K      REPULSIVE A REPULSIVE RHO///////)
      PRINT 18, RPLS, D, AQDP, AQQP, H, C, ARPL, EXRP
   18 FORMAT (F10.2, F10.2, F10.5, F10.6, F10.4, F10.6, F10.0, F10.3)
      PRINT 13
   13 FORMAT (1H1,81H POTENTIAL (ERGS)   DISPLACEMENT (CM.)  POTENTIAL (
     1REL. EVS) DISPLACEMENT SQUARED//////)
      DO 23 J=1,26,1
      PRINT 33, Y(J), X(J), Y1(J), X2(J)
   33 FORMAT (4E20.5)
      X2(J)=X2(J)*1.0E+16


      PUNCH 101, Y1(J), X2(J)
  101 FORMAT (E10.3, E10.8)
   23 CONTINUE
      STOP
      END
```

RPLS = ionic radius of metal supplied on data card 1.

D = metal-halide equilibrium internuclear distance supplied on data card 1.

AQDP = dipole polarizability of metal ion supplied on data card 1.

AQQP = spherical conductor quadrupole polarizability of metal ion ($\underline{\alpha_Q}$) in Angstroms to the fifth power ($Å^5$).

H = proportionality constant supplied on data card 3.

C = deformation constant supplied on data card 3.

ARPL = halide-halide repulsive pre-exponential supplied on data card 2.

EXRP = halide-halide repulsive decay constant supplied on data card 2.

Page 3 (Format 4E20.5)

Y(J) = total bending potential energy (V) in ergs.

X(J) = displacement coordinate ($r\theta$) in centimeters (cm).

Y1(J) = Y(J) in relative ergs.

X2(J) = $[X(J)]^2$ in centimeters squared (cm^2).

(All the above quantities are printed for each bending angle (θ) between ADL and ADG in increments of <u>two</u> degrees.)

<u>Options</u>:

PUNCH --- Program punches one card associated with each set of values printed on page 3 of the output.

Rows 1-10; Y1(J) in Format E10.3.

Rows 11-20; X2(J) in Format F10.8.

These cards, in turn, are used as input data for the program <u>LSQVMT</u> (See Appendix A-1c).

```
      PROGRAM FLIMHOL (INPUT,OUTPUT,PUNCH)
      DIMENSION X(100), Y(100), Y1(100), X2(100)
      READ 1, RPLS, AQDP, D
    1 FORMAT (F8.2, F8.5, F8.2)
      READ 41, ARPL, EXRP
   41 FORMAT (F8.0, F8.3)
      READ 300, CN1, CN2, CN3, ADL, ADG, C, Q, H
  300 FORMAT (3A10, 2F10.5, F10.6, F5.0, F7.4)
      DEGR=ADL
      PRINT 401
  401 FORMAT (1H1,54H COMPOUND NAME              MINIMUM ANGLE MAXIMUM ANGLE
     1 Q //////)
      PRINT 402, CN1, CN2, CN3, ADL, ADG, Q
  402 FORMAT (3A10, 2F10.5, F5.0)
      AQQP=Q*((AQDP**0.3333)**5.0)
      CGSQ=(23.04)/1.60209
      PRINT 8
    8 FORMAT (1H1,102H TOTAL POTENTIAL REPULSIVE POT. ATTRACTIVE POT. CH
     1ARGE-CHARGE CHARGE-DIPOLE CHARGE-QUADRUPOLE  ANGLE  ////)
      I=1
   31 TH=DEGR/57.295779
      X(I)=(D*DEGR*0.017453293*1.0E-08)
      X2(I)=(X(I)**2.)
      ANGT=SIN(TH)**2
      ANGF=ANGT**2
      ANGS=ANGT*ANGF
      B=(CGSQ/(-D))
      CGCG=B*(4.+4.*C*ANGT-1./(2.*COS(TH))-(C*ANGT)/(2.*COS(TH)))
      CGDP=B*(AQDP/D**3)*(2.*ANGT+8.*C*ANGF)
      CGQP=B*(AQQP/D**5)*(2.+(12.*C-6.)*ANGT+(6.-36.*C)*ANGF+36.*C*ANGS)
      V=CGCG+CGDP+CGQP
      DPRM=D*(1-C*ANGT)
      R=2*DPRM*COS(TH)
      VRPL=(ARPL/(R**2))*(EXP(-(R)/EXRP))
      VTOT=V+VRPL
      Y(I)=(VTOT*1.60209E-12)
      IF (DEGR) 102,103,102
  103 YO=VTOT
  102 CONTINUE
      Y1(I)=VTOT-YO
      I=I+1
      PRINT 61, VTOT, VRPL, V, CGCG, CGDP, CGQP, DEGR
   61 FORMAT (2E15.5, 4E15.4, F12.4)
      DEGR=DEGR+2.0000
      IF (DEGR-ADG) 31, 31, 11
   11 CONTINUE
      PRINT 28
   28 FORMAT (21(/)85H IONIC RADII RADIUS DIPOLE POL. QUADRUPOLE POL. H
     1    K      REPULSIVE A REPULSIVE RHO//////)
      PRINT 18, RPLS, D, AQDP, AQQP, H, C, ARPL, EXRP
   18 FORMAT (F10.2, F10.2, F10.5, F10.6, F10.4, F10.6, F10.0, F10.3)
      PRINT 13
   13 FORMAT (1H1,81H POTENTIAL (ERGS)   DISPLACEMENT (CM.)  POTENTIAL (
     1REL. EVS) DISPLACEMENT SQUARED//////)
      DO 23 J=1,26,1
      PRINT 33, Y(J), X(J), Y1(J), X2(J)
   33 FORMAT (4E20.5)
      X2(J)=X2(J)*1.0E+16


      PUNCH 101, Y1(J), X2(J)
  101 FORMAT (E10.3, E10.8)
   23 CONTINUE
      STOP
      END
```

APPENDIX A-1

b. Program BSLF00*

(The * is replaced by a number.)

Purpose:

The program BSLF00* is designed to evaluate the wavefunctions (in this case, Bessel functions of order m, $J_m(\chi)$) for a two-dimensional cyclindrical potential well (see Appendix A-3a), as a function of the energy. This system is taken as a model of the potential energy well for metal dihalide molecules in the gas phase.

Input Data:

The data cards that are used to describe the input data for the Bessel function evaluation are preceded by a comment card designating the metal dihalide molecule being considered.

Card 1 (Format E10.4)

D = metal-halide equilibrium internuclear distance (ℓ) in centimeters (cm.); corresponds to half-width of the potential well.

Card 2 (Format I5)

NMB = number of successive energy level increments to be made for a Bessel function of a given order.

Card 3 (Format 2F10.4)

ALKA = atomic mass of the metal (m_m) in atomic mass units (amu).

HALIDE = atomic mass of the halide (m_x) in atomic mass units (amu).

Card 4 (Format F10.4, 2I5)

OW = lower limit of energy level value in electron volts (eV).

N = the order of the Bessel function sought.

SIGN = 1. if initially Bessel function is positive.

= 0. if initially Bessel function is negative.

Library Subroutines:

BESSJY - Identified as C3 BKY BESSJY, this subroutine evaluates the Bessel functions $J_m(\chi)$ and $Y_m(\chi)$, and is available from the LBL Computer Library.

Output:

Page 1 (Format 5E15.6)

BJ(N + 1) = value of Bessel function $J_m(\chi)$.

X = value of χ (see Appendix A-3a).

R = well coordinate in centimeters (cm).

S = energy of level E in electron volts (eV).

Z = energy of level E in ergs.

(All of the above quantities are printed for well coordinates increasing in regular increments from zero to the metal-halide equilibrium internuclear distance. The energy of the level is increased, and the process is repeated.)

Page * (Format F15.8, I3)

RMASS = reduced mass (μ) of the metal dihalide.

N = the order of the Bessel function, supplied on data card 4.

(* This output appears immediately following completion of all steps listed under Page 1.)

Remarks:

Due to the boundary condition $(J_m(\chi) \equiv 0.)_{R=\ell}$ constraining this system, the energy corresponding to a given wavefunction can be determined from the output of this program. By successive approximations, the energy of this level can be evaluated to any needed accuracy by an iterative procedure.

```
      PROGRAM BSLF001 (INPUT,OUTPUT)
      DIMENSION BJ(15), BY(15)
      READ 101, D
  101 FORMAT (E10.4)
      READ 102, NMB
  102 FORMAT (I4)
      READ 103, ALKA, HALIDE
  103 FORMAT (2F10.4)
      RMASS=(2.*ALKA*HALIDE)/(ALKA+2.*HALIDE)
$ STRONTIUM BROMIDE
      DO 19 N=10,17
      PRINT 20
   20 FORMAT (70H BESSEL FUNCTION    X    RADIAL DISPLACEMENT   ENERGY(I
     1 ENERGY(ERGS)   )
      DO 1 JP=1,NMB
      XP=SQRT(2.*RMASS*1.60209E-12*JP*0.0001)
      X=(XP*D/5.14195E-15)
      CALL BESSJY (X, BJ, BY, N)
      Z=JP*1.60209E-12*0.0001
      PRINT 16, BJ(N+1), X, D, JP, Z
   16 FORMAT (3E15.6, I10, E15.6)
    1 CONTINUE
      PRINT 24
   24 FORMAT (21H REDUCED MASS,  ORDER)
      PRINT 25, RMASS, N
   25 FORMAT (F15.8, I3)
   19 CONTINUE
      STOP
      END
```

APPENDIX A-1

c. Program LSQVMT

Purpose:

The library program LSQVMT uses the non-linear least-squares method to fit a given theoretical function to the data points supplied. In our case, the data are the punched output of the program **IMHØL (see Appendix A-1a). The theoretical function is the potential energy function for a harmonic oscillator with a superimposed Gaussian perturbative hump (see Appendix A-3b). This particular type of potential energy function is used to model the predicted potential energy well for the metal dihalide gas molecules.

Input Data:

The user must supply a subroutine to the library program LSQVMT.

The data cards that are required by our subroutine are as follows:

Card 1 (Format 12I5)

IREAD = 1, if some parameters of the fitting function (F(T,X)) are to be fixed constants; = 0, otherwise.

IWRITE = 3

K = 5

ISIZE = 8

(VARMIT control card - other parameters have values suggested in LSQVMT writeup.)

Card 2 (Format 6I10)

N = number of fitting parameters (X(I)).

INVAR = number of independent variables (T(J)).

NUMDTA = number of data cards from punched output of program **IMHØL.

IWGT = 2

(LSQ Control Card - other parameters have values suggested in LSQVMT writeup.)

Card 3 (Format 12A6)

Alphanumeric card of user's choice.

Cards 4 through 4 + N - 1 (Format 8E10.0)

Punched output cards from program **IMHØL.

Card 4 + N (Format F20.8, E15.5)

GMH = atomic mass of the halide (m_x) in atomic mass units (amu).

GMAE = atomic mass of the alkaline earth (m_m) in atomic mass units (amu).

CN1 = alphanumeric chemical formula of the alkaline earth dihalide compound.

Card 4 + N + 1 (Format 8E10.0)

X(1), X(2), X(3), and X(4)

= initial guesses of the values of X(I) (generally, each set equal to one or zero).

Card 4 + N + 2 (Format 8E10.0)

X(1), X(2), X(3), and X(4)

= 1., if parameter X(I) is fixed.

= 0., if parameter X(I) is free to float.

(Card is removed if IREAD ≠ 1.)

Card 4 + N + 3 (Format E10.4, F10.1)

FC1 = stretching force constant (k_1) for alkaline earth dihalide in dynes per centimeter (dynes/cm).

THET = bending angle (α) in degrees (°).

(All of the above input data cards are explained in greater detail in the library subroutine LSQVMT writeup.)

Library Subroutines:

LSQVMT - Identified as E2 BKY LSQVMT, this subroutine least-squares fits a given theoretical function (F(T,X)) to supplied data and is available from the LBL Computer Library.

Output:

Page 1 (Format 12I5)

Printout of values of parameters on VARMIT control card, supplied on data card 1.

Page 2 (Format 6I10)

Printout of values of parameters on LSQ control card, supplied on data card 2. The quantity of information printed depends on the choice of parameter values on this card. Also, the data supplied on cards 3, 4, ..., 4 + N - 1, 4 + N + 1, and 4 + N + 2 are printed.

Page * (Format 3E15.6; Format F10.4; Format F10.4; and Format A10)

ALPHA = pre-exponential (η) for Gaussian hump.

BETA = decay constant (λ) of Gaussian hump.

CAPPA = harmonic bending force constant (k_b) of unperturbed potential well in dynes per centimeter (dynes/cm).

V1 = symmetric stretching frequency (ν_1) in inverse centimeters (cm^{-1}).

V2 = bending frequency (ν_2) of unperturbed potential well in inverse centimeters (cm^{-1}).

CN1 = compound identification, supplied on data card 4 + N.

(* This output appears on the final pages of the printout, and includes the parameters of the best least-squares fit. All constants are explained in Appendix A-3b.)

Options:

As mentioned under data card 2, the user may choose the quantity of information (including tables and graphs) to be printed. Using data cards 4 through 4 + N - 1, the user can weight input data according to his needs. Data card 4 + N + 2 allows variable or constant values for the dependent variables X(I).

Remarks:

The program LSQVMT, as currently designed, always ends with a dump. The program searches for a new set of data to least-squares fit; when this data is not found, a dump ensues.

```
      PROGRAM LSQVMT (INPUT,OUTPUT,TAPE2=INPUT,TAPE3=OUTPUT)

      SUBROUTINE TABLE (F,G,X,T,M1)
      DIMENSION G(40)
      DIMENSION X(40), T(10)
      IF (M1.EQ.1) GO TO 100
      G(1)=T(1)
      G(2)=(EXP((-X(3))*T(1)))-1.0000
      G(3)=(X(2)*(-T(1))*(EXP((-X(3))*T(1))))
      CAPPA=(2.*X(1))
      CAPPA=CAPPA*1.60209E+04
      ALPHA=((X(2)*SQRT(UMASS))/(HBAR*SQRT(CAPPA)))
      ALPHA=ALPHA*1.60209E-12
      BETA=((X(3)*HBAR)/SQRT((CAPPA*UMASS)))
      BETA=BETA*1.0E+16
      F=(X(1)*T(1))+(X(2)*EXP((-X(3))*T(1)))-X(2)
      IF (M1.EQ.4) GO TO 1
      GO TO 5
    1 CONTINUE
      PRINT 11
   11 FORMAT (47H ALPHA          BETA                    FORCE CONST. )
      PRINT 12, ALPHA, BETA, CAPPA
   12 FORMAT (3E15.6)
      READ 999, FC1, THET
  999 FORMAT (E10.4, F10.1)
      SS=(SIN(THET)*SIN(THET))
      SC=(COS(THET)*COS(THET))
      U1=(2.*GMH/GMAE)
      U2=(GMH/AVOGN)
      W1=(2.*(1.+U1)*FC1*CAPPA/(U2*U2))
      W2=(W1/(16.*(PI**4.)))
      W3=((1.+(U1*SC))*(FC1/U2))+((1.+(U1*SS))*(CAPPA/U2))
      W4=(W3/(4.*(PI**2.)))
      T1=(W4*W4)-(4.*W2)
      IF (T1.LE.0) GO TO 899
      T2=SQRT(T1)
      V1=(SQRT((W4+T2)/2.))/CL
      V2=(SQRT((W4-T2)/2.))/CL
      GO TO 898
  899 V1=0.
  898 CONTINUE
      PRINT 998, V1
  998 FORMAT (51H SYMMETRIC STRETCHING FREQUENCY, V1  -DYNES/CM.-  =F10.
     14)
      PRINT 997, V2
  997 FORMAT (38H BENDING FREQUENCY, V2  -DYNES/CM.-  =F10.4)
      PRINT 996, CN1
  996 FORMAT (17H COMPOUND NAME  =A10)
    5 CONTINUE
      GO TO 110
  100 READ 1002, GMH, GMAE, CN1
 1002 FORMAT (2F10.4, A10)
      AVOGN=6.02252E+23
      CL=2.997925E+10


      UMASS=(2.*GMH*GMAE)/((GMAE+(2.*GMH))*AVOGN)
      HBAR=(6.62554E-27/6.2831853071)
      PI=3.14159265
  110 CONTINUE
      RETURN
      END
```

APPENDIX A-1

d. Program HØAEH1

Purpose:

The program HØAEH1 is designed to evaluate the eigenvalues for a harmonic bending potential well with a superimposed Gaussian perturbative hump. The bending frequencies of the metal dihalide molecule can be calculated, to a first approximation, from the spacing between energy levels.

Input Data:

The data cards that are used to describe the constants of the perturbed harmonic potential are preceded by a comment card designating the metal dihalide molecule under consideration.

Card 1 (Format I5, 3E15.6, 2I5)

N = number of eigenvalues to be evaluated.

ALPHA = pre-exponential constant (η) of Gaussian perturbative hump.

BETA = decay constant (λ) of Gaussian perturbative hump.

VNU = bending frequency (ν') for harmonic potential in inverse centimeters (cm^{-1}).

L1 = lower limit of angular momentum quantum number ($\mathcal{L}$).

L2 = upper limit of angular momentum quantum number ($\mathcal{L}$).

(All of the above constants are explained in Appendix A-3b.)

Library Subroutines:

HØQR - Identified as F2 CAL HØQR, this subroutine computes the eigenvalues of a real symmetric matrix (see Appendix A-3b).

GAMMAR - Identified as C3 BKY GAMMAR, this subroutine evaluates the gamma function $\Gamma(x)$ of any real argument x.

Both subroutines are available from the LBL Computer Library.

Output:

Page 1 (Format E17.8, I5, I5)

EIVU = eigenvalues (E) for a given angular momentum of a harmonic potential with a Gaussian perturbative hump, in ergs.

IL = energy level number.

L = value of angular momentum quantum number ($\mathcal{L}$).

Page 2 (Format 3E30.5)

ALPHA = pre-exponential for the Gaussian perturbative hump, supplied on data card 1.

BETA = decay constant for the Gaussian perturbative hump, supplied on data card 1.

GAMMA = value of parameter γ (see Appendix A-3b).

(Pages 1 & 2 are repeated for each value of the angular momentum previously specified.)

```
      PROGRAM HOAEH1 (INPUT,OUTPUT)
      DIMENSION A(100,100), H(100,100), EIVU(100)
      NDIM=100
      NOYES=0
      READ 1, N, ALPHA, BETA, VNU, L1, L2
    1 FORMAT (I5, 3F15.6, 2I5)
      HPLNK=6.62554E-27
      CLGHT=2.997925E+10
      VNU=VNU*CLGHT
      DO 16 L=L1,L2,1
      GAMMA=1./(1.+BETA)
      N2=2*N
      DO 625 I=1,N2,2
      KI=(I-1)/2
      DO 81 J=1,N2,2
      KF=(J-1)/2
      IF (KF-KI) 64, 121, 121
  121 CONTINUE
  289 IV=I+L-1
      B=(BETA**(KF-KI))
      G=(GAMMA**(L+KI+KF+1))
      ASMT=0.0000
      DO 4 KT=0,KI,1
      B1=(BETA**(2.*KT))
      X=KI+1.
      Y=GAMMAR(X)
      YKI=Y
      X=KF+1.
      Y=GAMMAR(X)
      YKF=Y
      X=L+KI+1.
      Y=GAMMAR(X)
      YLKI=Y
      X=L+KF+1.
      Y=GAMMAR(X)
      YLKF=Y
      X=KT+1.
      Y=GAMMAR(X)
      YT=Y
      X=KF-KI+KT+1.
      Y=GAMMAR(X)
      YFIT=Y
      X=KI-KT+1.
      Y=GAMMAR(X)
      YIT=Y
      X=KI+L-KT+1.
      Y=GAMMAR(X)
      YILT=Y
      SUMT=(B1*((YKI*YKF*YLKI*YLKF)**0.5000))/(YT*YFIT*YIT*YILT)
    4 ASMT=ASMT+SUMT
      I=(I+1)/2
      J=(J+1)/2
      H(I,J)=(ALPHA*G*B*ASMT)
      E=IV+1.
      IF (J-I) 25, 36, 49


   36 A(I,J)=E+H(I,J)
      GO TO 25
   49 A(I,J)=H(I,J)
      A(J,I)=A(I,J)
   25 CONTINUE
      I=(2*I)-1
      J=(2*J)-1
   64 CONTINUE
   81 CONTINUE
  625 CONTINUE
      CALL HOQR (A, NDIM, N, EIVU, NOYES, DUMMY)
      PRINT 144
  144 FORMAT (27H EIGENVALUES(I)=    I1=    L=)
      DO 196 I1=1,N,1
      EIVU(I1)=EIVU(I1)*HPLNK*VNU
      PRINT 169, EIVU(I1), I1, L
  169 FORMAT (E17.8, I5, I5)
  196 CONTINUE
      PRINT 225
  225 FORMAT (32H ALPHA=        BETA=        GAMMA=)
      PRINT 256, ALPHA, BETA, GAMMA
  256 FORMAT (3E30.5)
   16 CONTINUE
      STOP
      END
```

APPENDIX A-1

e. Program NEWTØN

Purpose:

The library program NEWTØN calculates equilibrium internuclear bond lengths of the metal dihalide molecules (see Eq. (III-17b)) using the "linear" polarizable ion model. The stretching force constant and the stretching frequencies for these molecules also are determined (see Chapter III).

Input Data:

The user must furnish a subroutine to the library program NEWTØN. This subroutine supplies the form of and the values of a set of equations and their first derivatives. The input data for the program NEWTØN itself are fully explained in the library writeup, and need not be altered from compound to compound. Thus, only the individual data necessary for each molecule are described herein.

Card 1 (Format 4E10.4)

P(1) = charge of an electron squared (e^2) in electrostatic units squared (esu^2).

P(2) = polarizability of the halide (β_D) in centimeters cubed (cm^3).

P(3) = pre-exponential repulsion constant (A) in ergs (or ergs-cm^2).

P(4) = repulsive decay constant (ρ) in centimeters (cm).

(Card immediately follows "PARAMETERS" data card from NEWTØN program.)

Card 2 BLANK

Card 3 (Format 2F10.4, A10)

GMH = atomic mass of the halide (m_x) in atomic mass units (amu).

GMAE = atomic mass of the alkaline earth (m_m) in atomic mass units (amu).

CN1 = alphanumeric chemical formula of the alkaline earth dihalide compound.

Card 4 (Format F10.4)

ANGLE = bending angle (θ) in degrees (°).

(Card 4 appears only for non-linear version of the "linear" polarizable ion model described in Chapter III; otherwise, this card is absent.)

Library Subroutines:

NEWTØN - Identified as C2 BKY NEWTØN, this program computes zeroes of an arbitrary set of functions using Newton's method. It is available from the LBL Computer Library.

Output:

Page 1

Printout of the values of all parameters supplied to program NEWTØN by user.

Page 2 (Format 4E15.4, A10)

X(1) = equilibrium internuclear distance of metal-halide bond (ℓ) in centimeters (cm).

FC1 = stretching force constant (k_1) in dynes per centimeter (dynes/cm).

V1 = symmetric stretching frequency (ν_1) in inverse centimeters (cm^{-1}), for linear molecules only.

V3 = asymmetric stretching frequency (ν_3) in inverse centimeters (cm^{-1}).

CN1 = compound identification, supplied on data card 3.

(Since this program employs an iterative fitting procedure, the values of the parameters on this page are printed for each iteration until convergence is attained.)

Options:

All options are fully explained in the NEWTØN writeup.

Remarks:

The initial guess value (card following NEWTØN data card "GUESSES") is critical. If the equilibrium internuclear bond length is greatly over- or underestimated, the program may "blow-up".

```
      PROGRAM NEWTON (INPUT,OUTPUT,TAPE3=OUTPUT)

      SUBROUTINE FCN (X,F,G,P)
      DIMENSION X(20),F(20,20),G(20),P(20)
      G(1)=(-7.*P(1)/(4.*(X(1)**2.)))-(49.*P(1)*P(2)/(8.*X(1)**5.))+((P(
     13)/P(4))*EXP(-X(1)/P(4)))
      F(1,1)=(7.*P(1)/(2.*X(1)**3.))+(245.*P(1)*P(2)/(8.*X(1)**6.))-((P(
     13)/(P(4)**2.))*EXP(-X(1)/P(4)))
      PRINT 1000,X(1)
 1000 FORMAT(//////44H EQUILIBRIUM INTERNUCLEAR DISTANCE  -CM.-  =E15.4)
      FC1=-(F(1,1))
      PRINT 1001,FC1
 1001 FORMAT(//////46H STRETCHING FORCE CONSTANT, K1  -DYNES/CM.-  =E15.
     14)
      IF (X(1)-1.5E-08) 1005,1006,1005
 1005 IF (X(1)-2.0E-08) 1007,1006,1007
 1006 CONTINUE
      PI=3.14159265
      READ 1002,GMAE,GMH,CN1
 1002 FORMAT(2F10.4,A10)
      AVOGN=6.02252E+23
      U=((2.*GMH*GMAE)/((2.*GMH)+GMAE))/AVOGN
      CL=2.997925E+10
 1007 CONTINUE
      IF (FC1.LE.0.) FC1=0.
      V1=(SQRT(FC1*AVOGN/GMH))/(2.*PI*CL)
      PRINT 1003,V1
 1003 FORMAT(//////48H SYMMETRIC STRETCHING FREQUENCY, V1  -1./CM.-  =E1
     15.4)
      V3=(SQRT(2.*FC1/U))/(2.*PI*CL)
      PRINT 1008, V3
 1008 FORMAT(//////49H ASYMMETRIC STRETCHING FREQUENCY, V3  -1./CM.-  =E
     115.4)
      PRINT 1004,CN1
 1004 FORMAT(//////27H COMPOUND IDENTIFICATION  =A10)
      RETURN
      END
```

APPENDIX A-2

Bending Potential Energy Curves

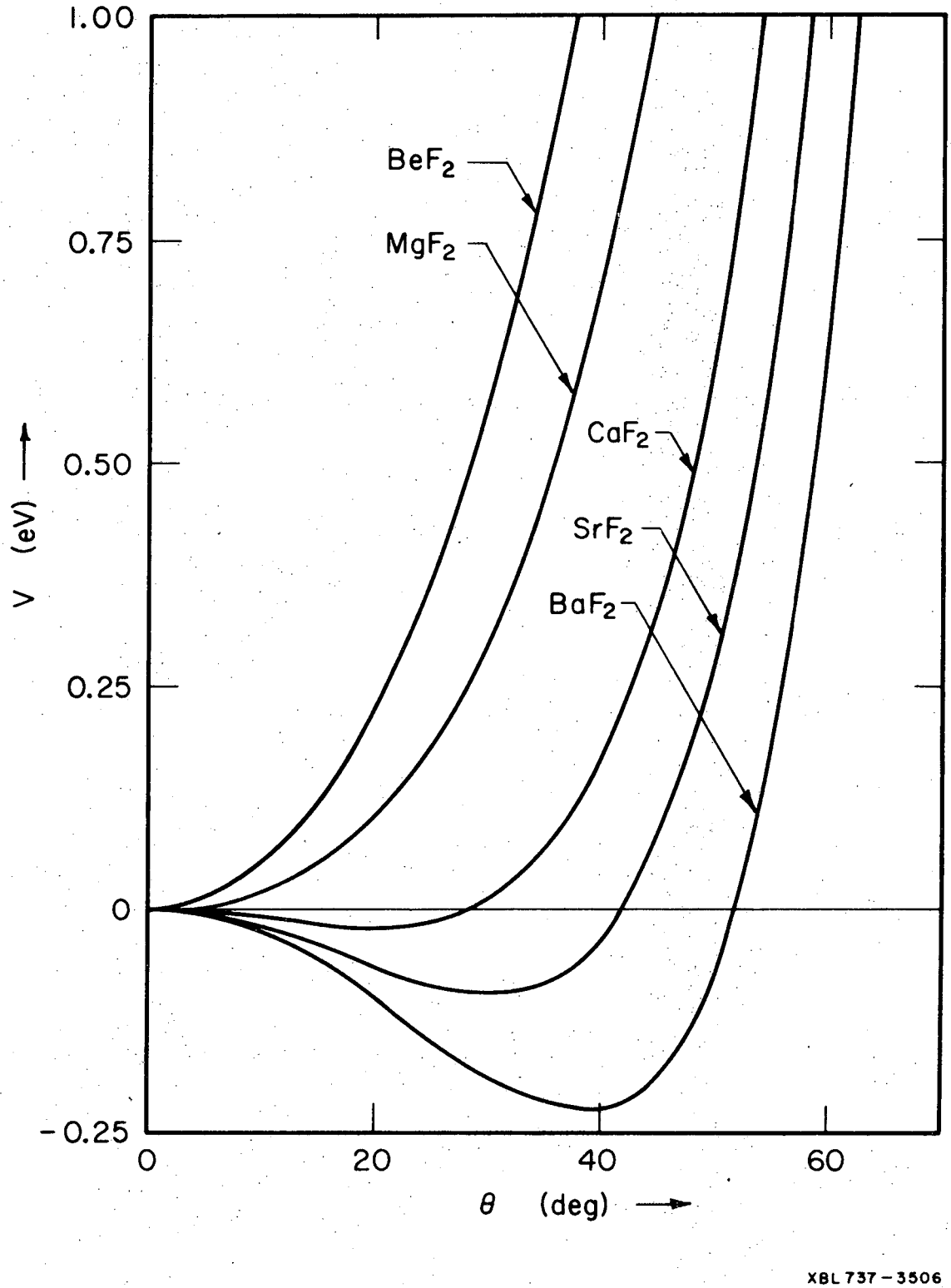

Fig. A-2-1. Alkaline earth fluorides.

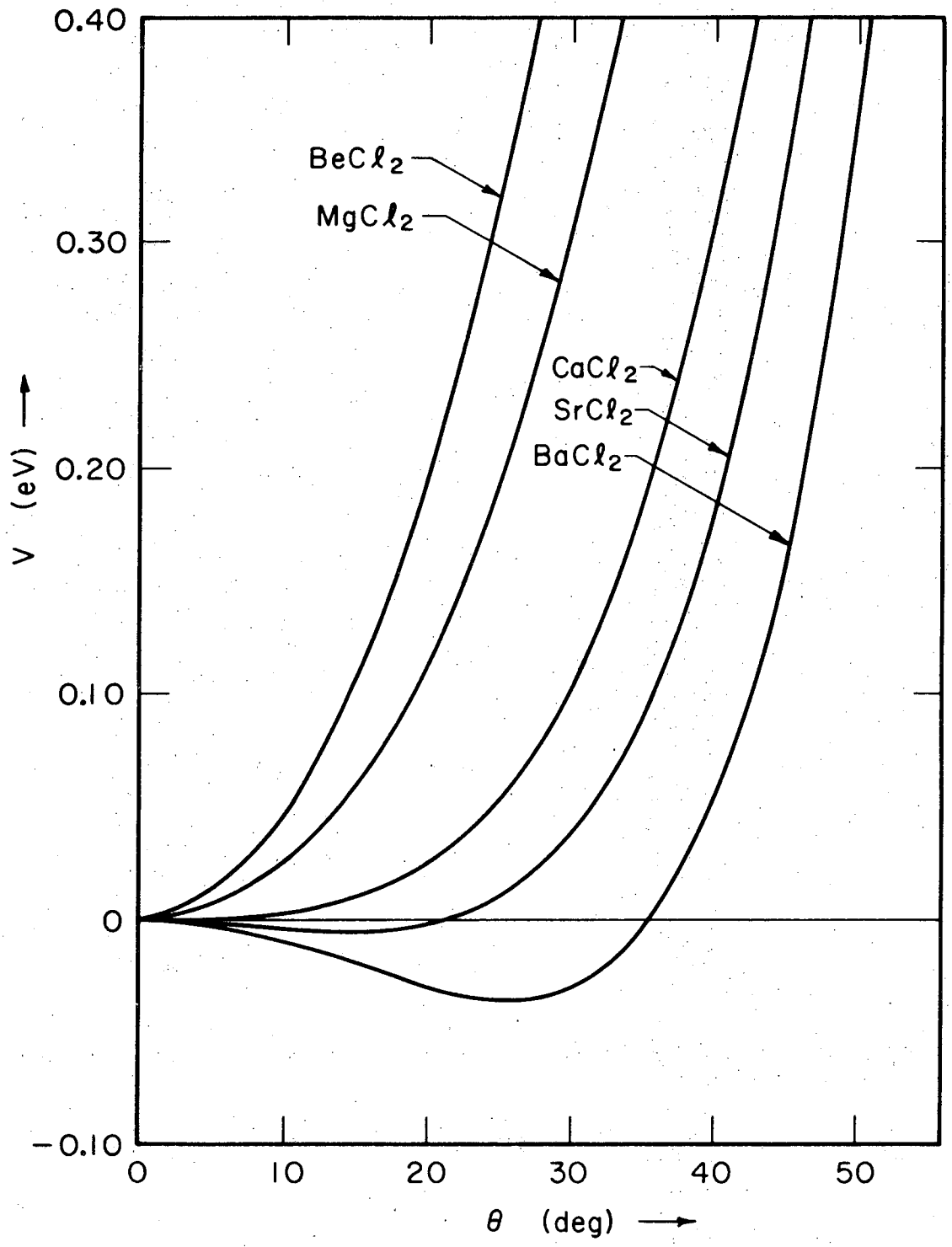

XBL 737-3507

Fig. A-2-2. Alkaline earth chlorides.

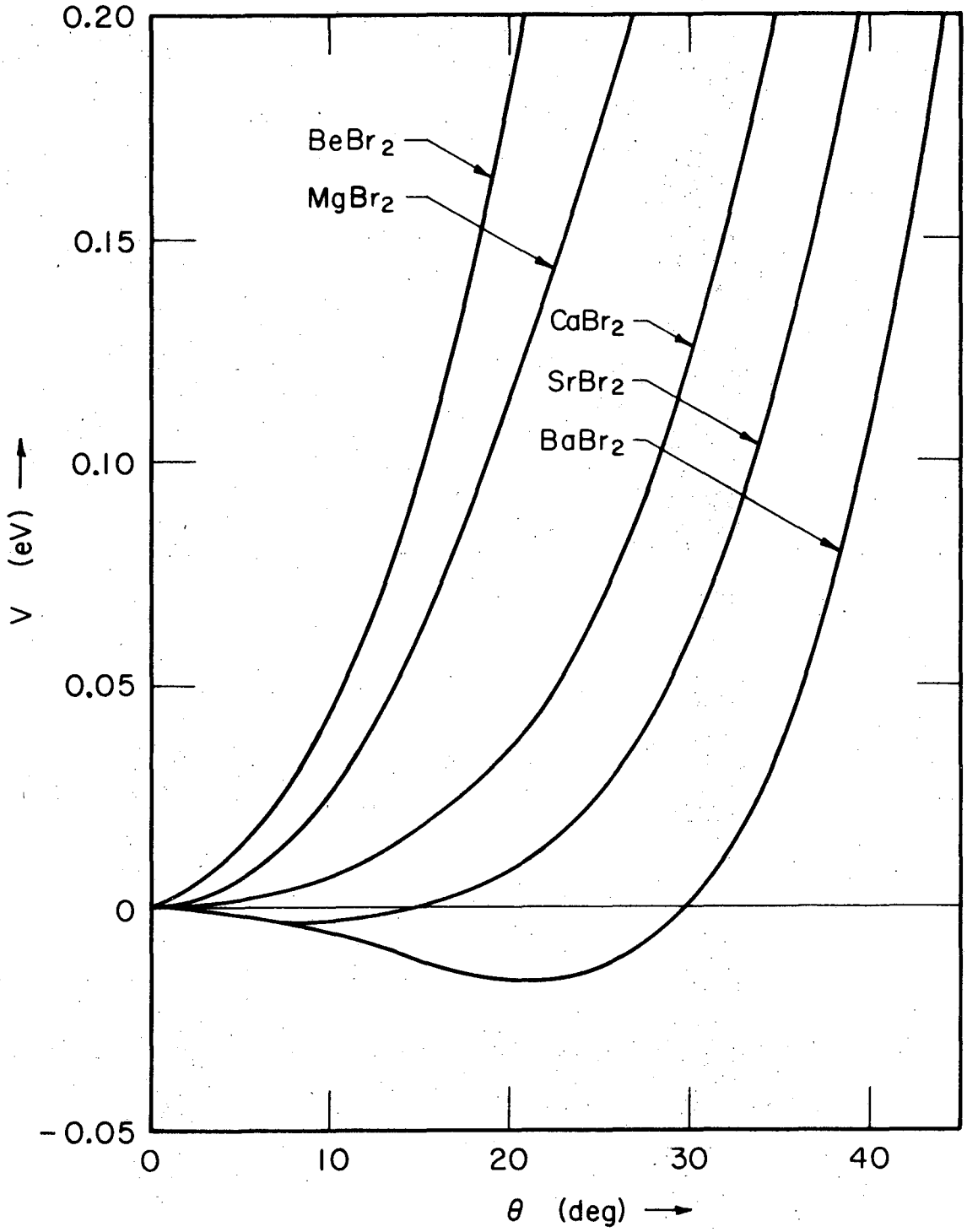

Fig. A-2-3. Alkaline earth bromides.

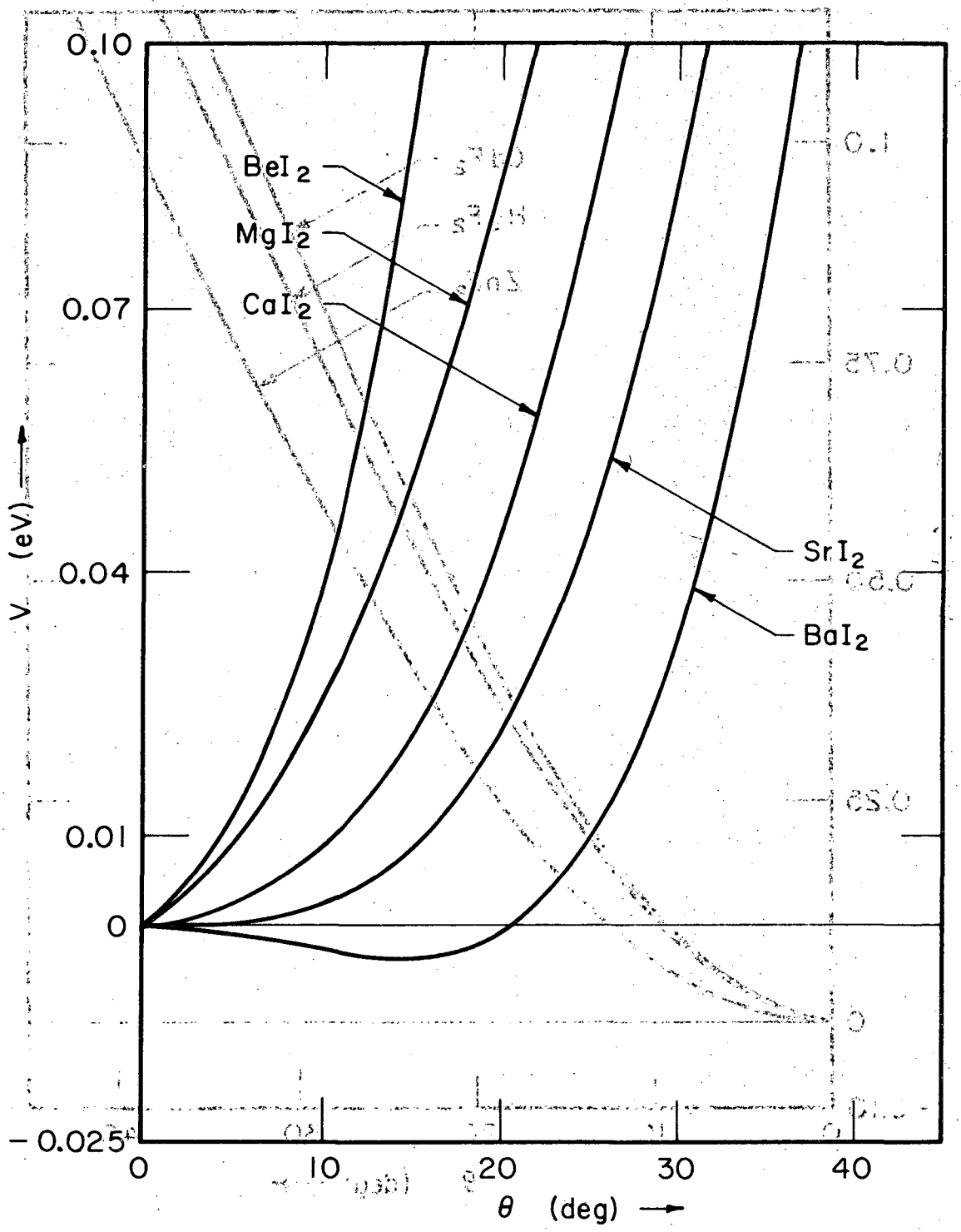

XBL 737 – 3509

Fig. A-2-4. Alkaline earth iodides.

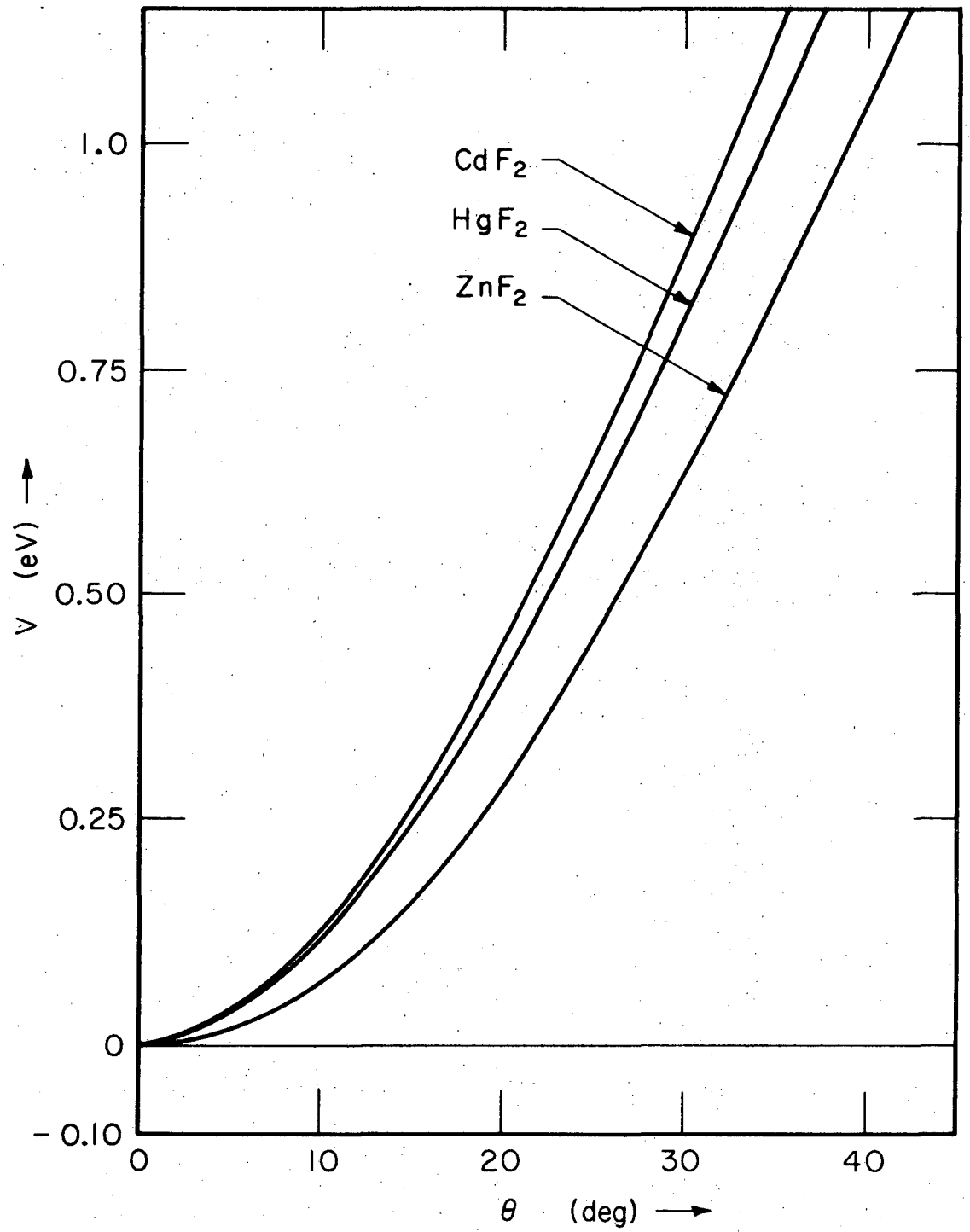

Fig. A-2-5. Group II-b fluorides.

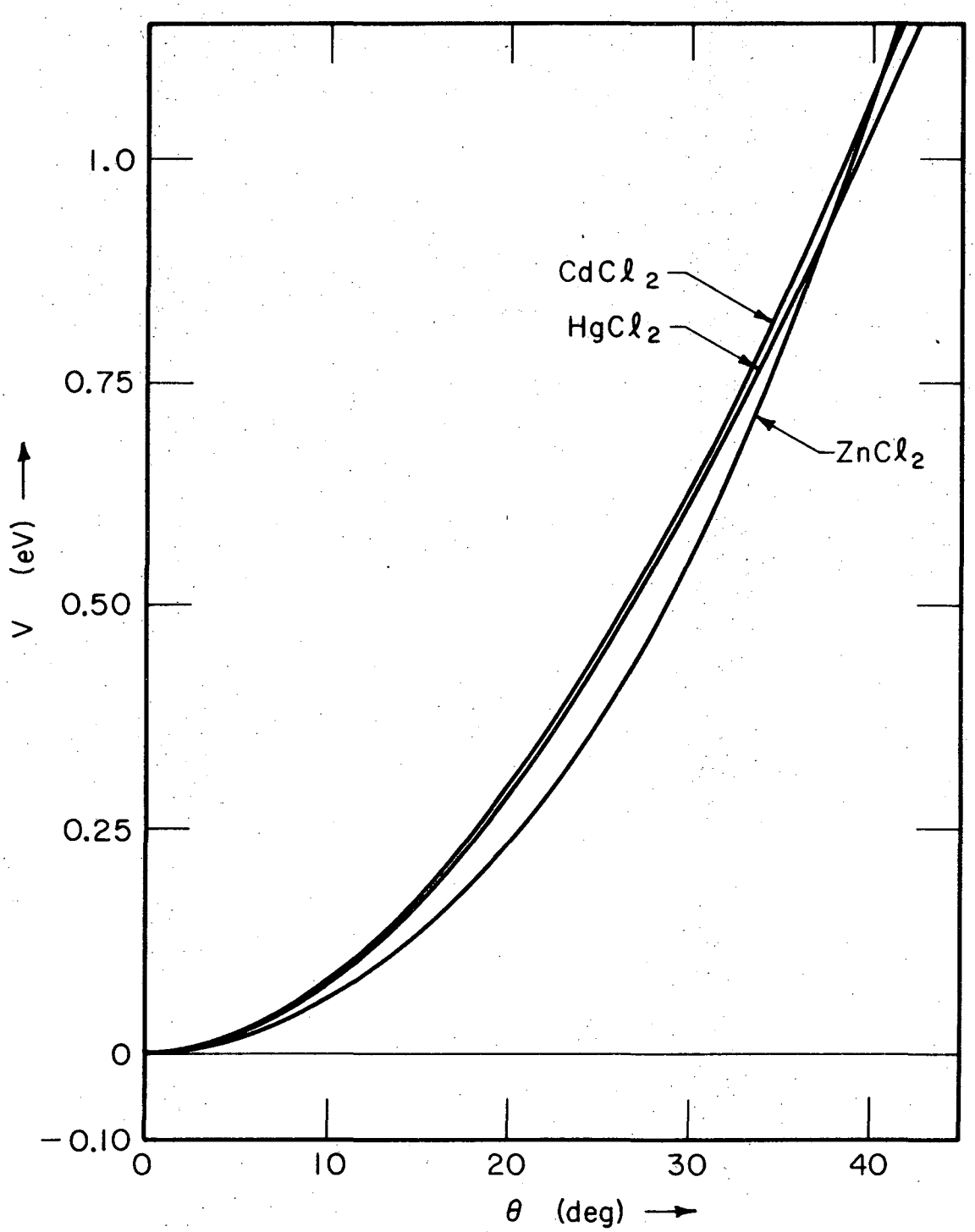

Fig. A-2-6. Group II-b chlorides.

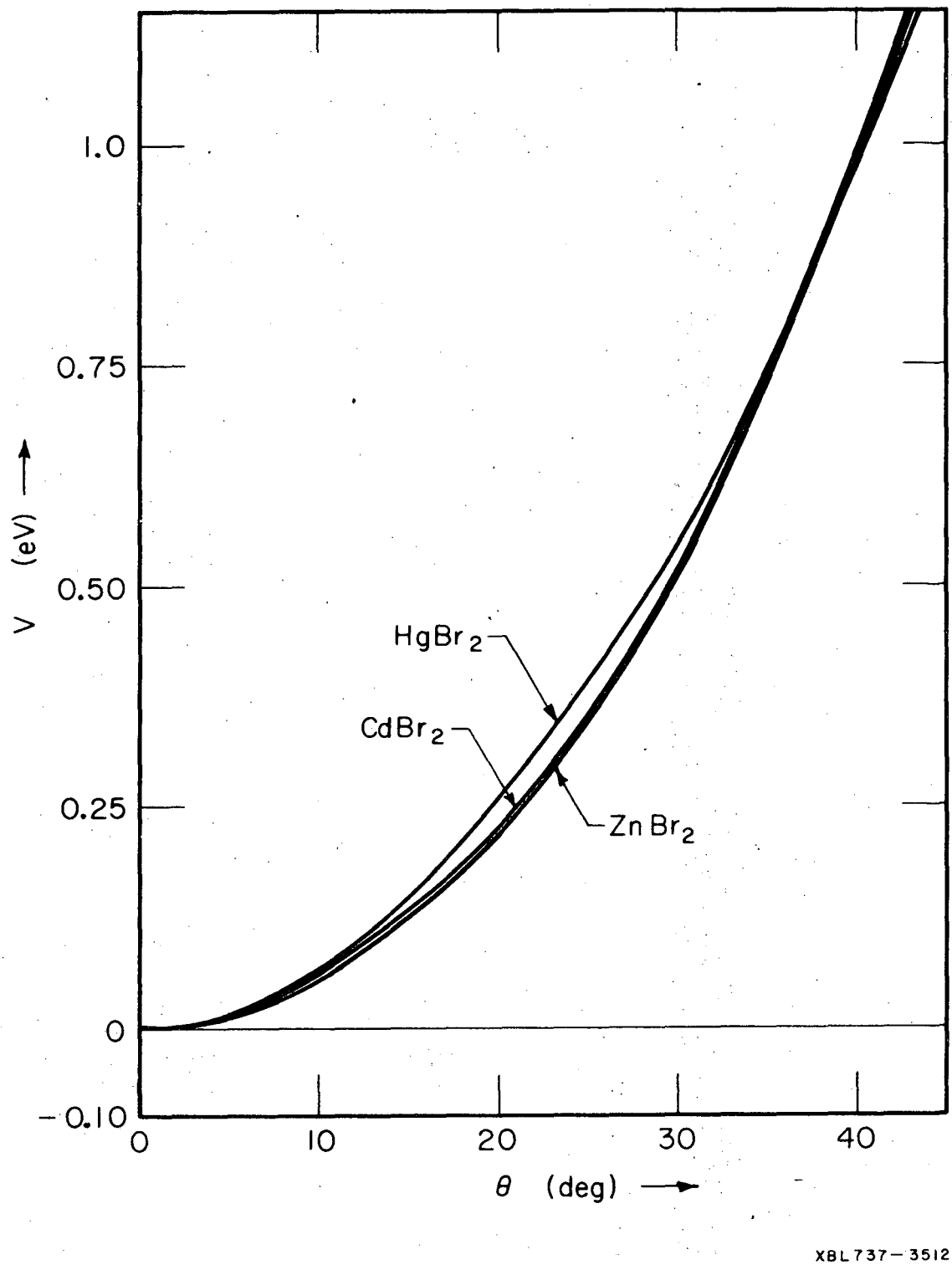

Fig. A-2-7. Group II-b bromides.

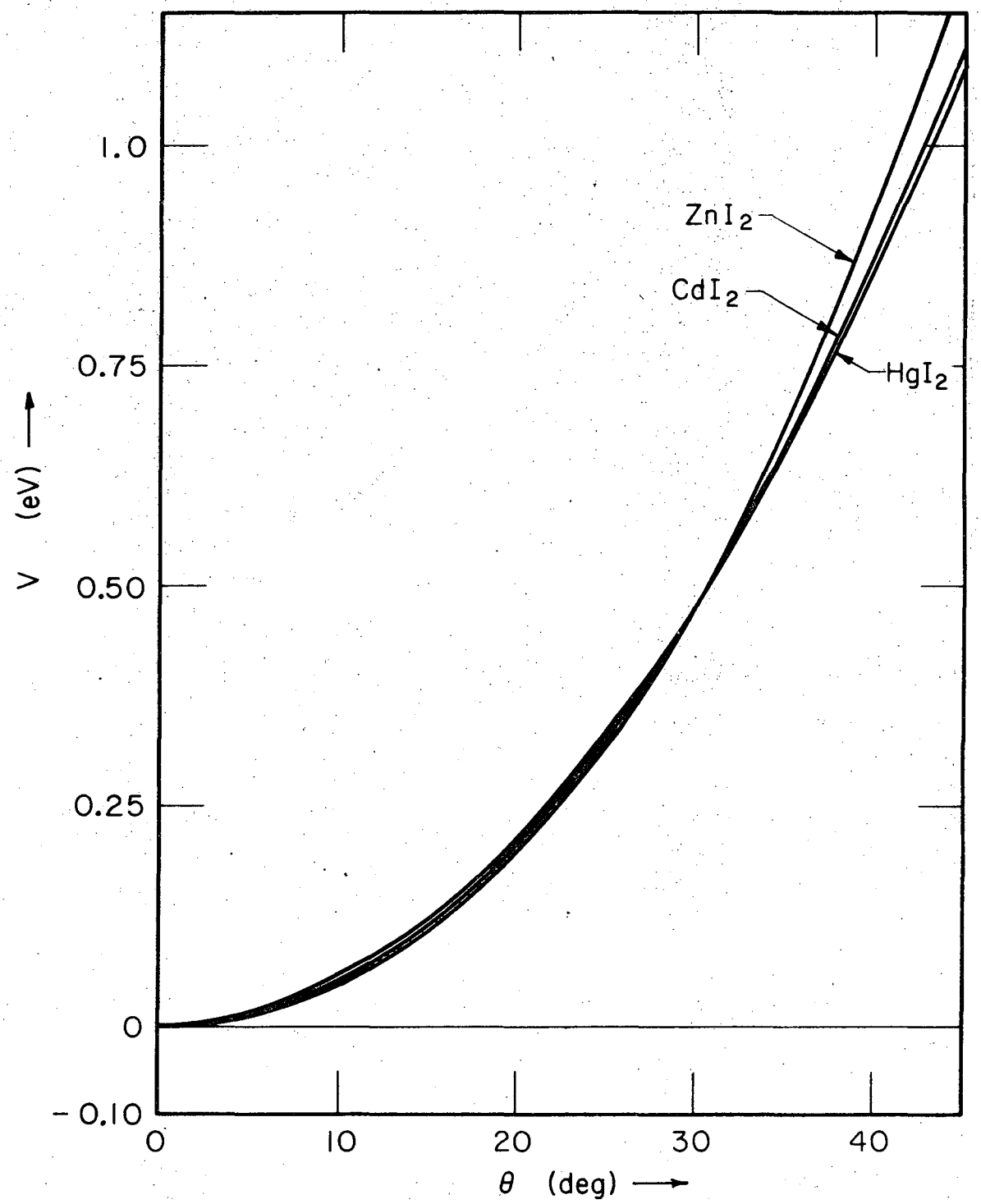

XBL 737-3513

Fig. A-2-8. Group II-b iodides.

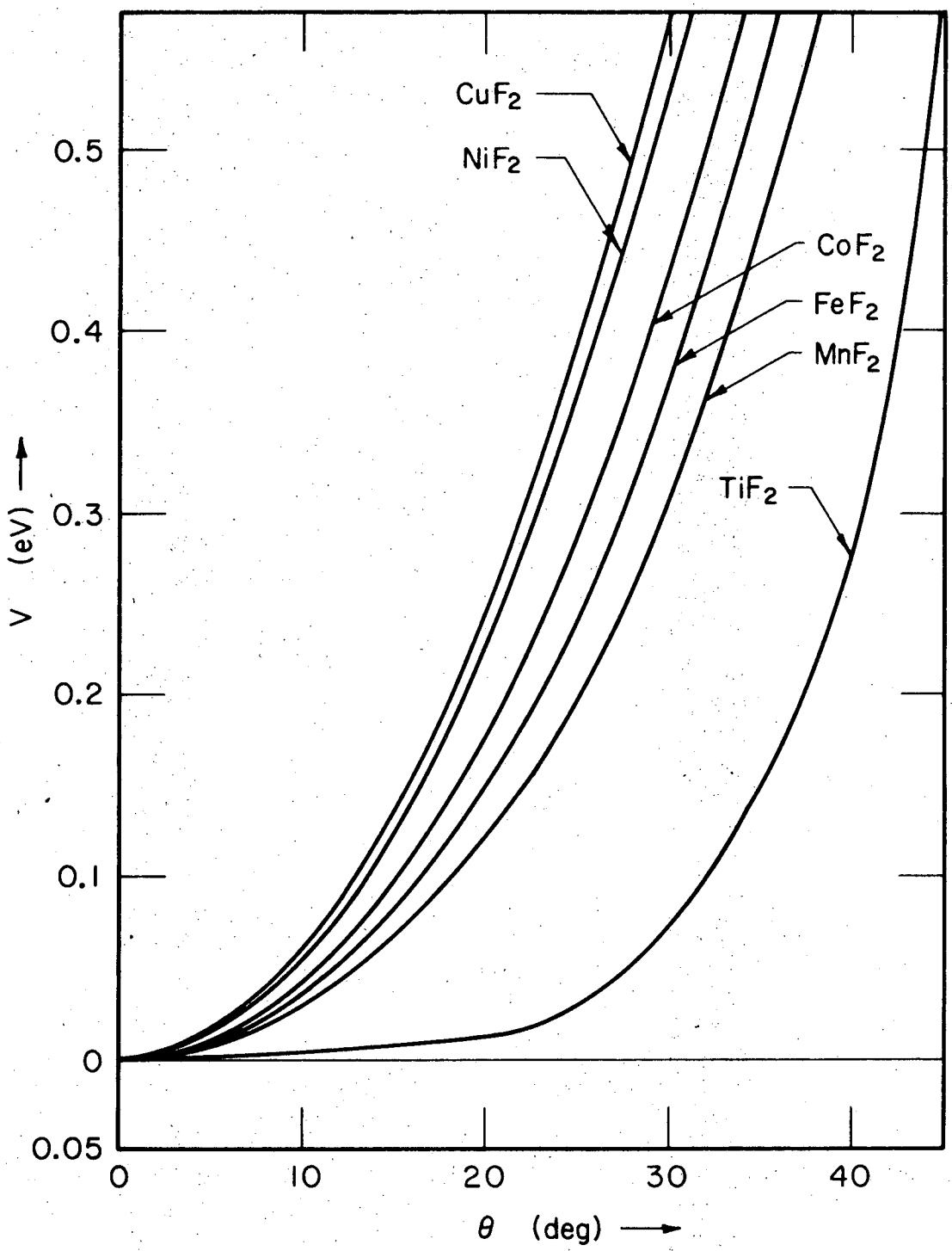

XBL 737-3584

Fig. A-2-9. Transition metal fluorides.

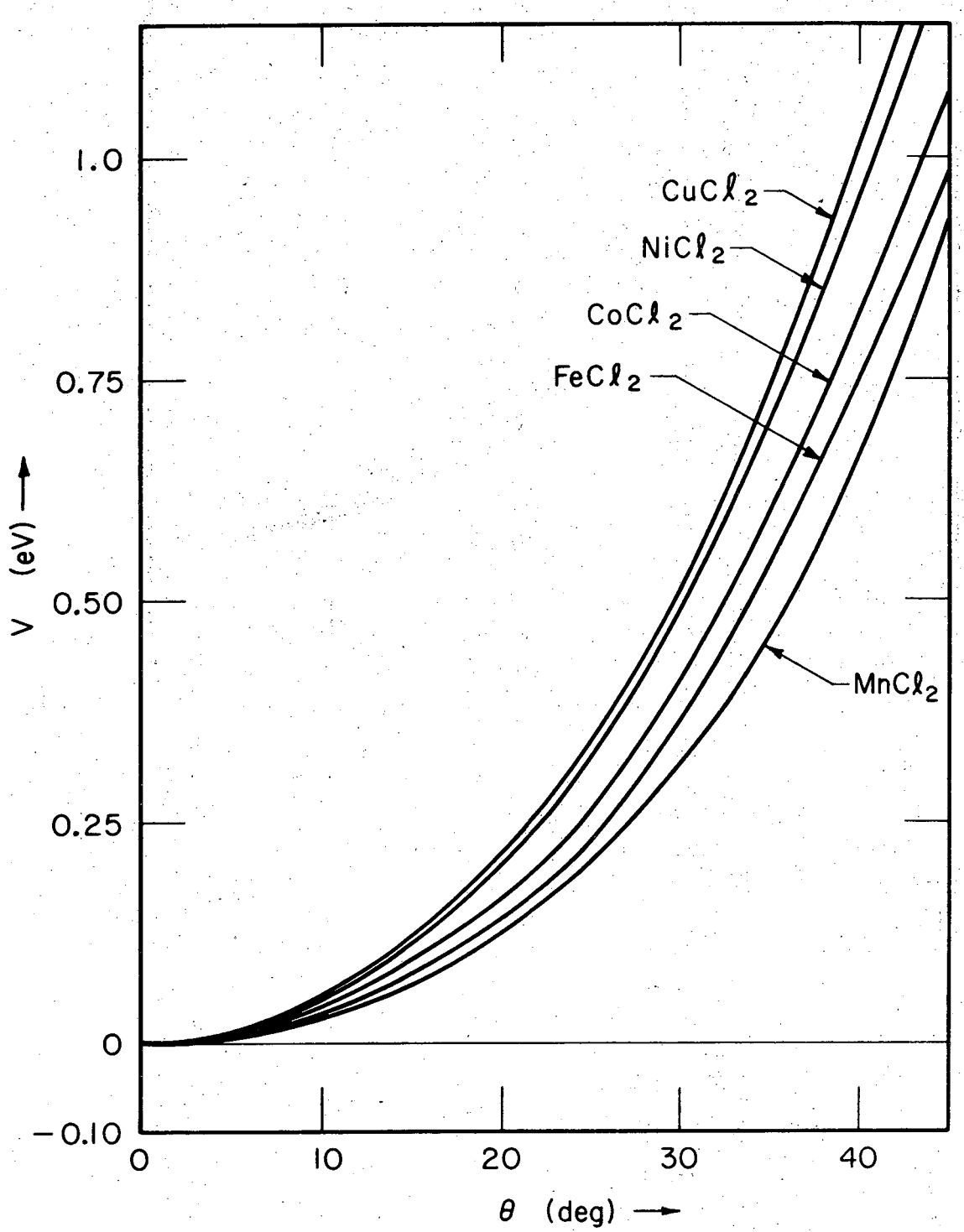

XBL 737 – 3514

Fig. A-2-10. Transition metal chlorides.

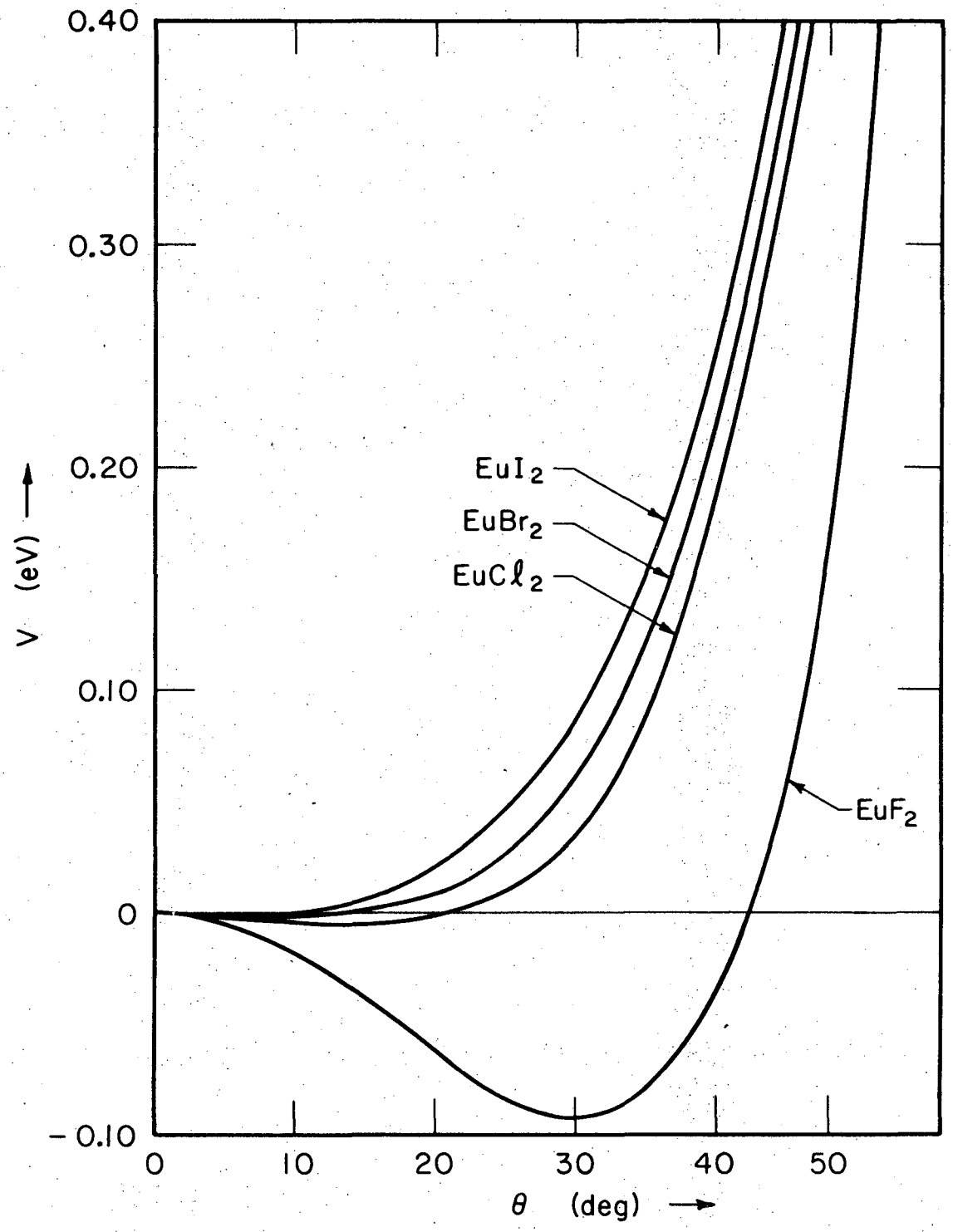

XBL737-3516

Fig. A-2-11. Europium dihalides.

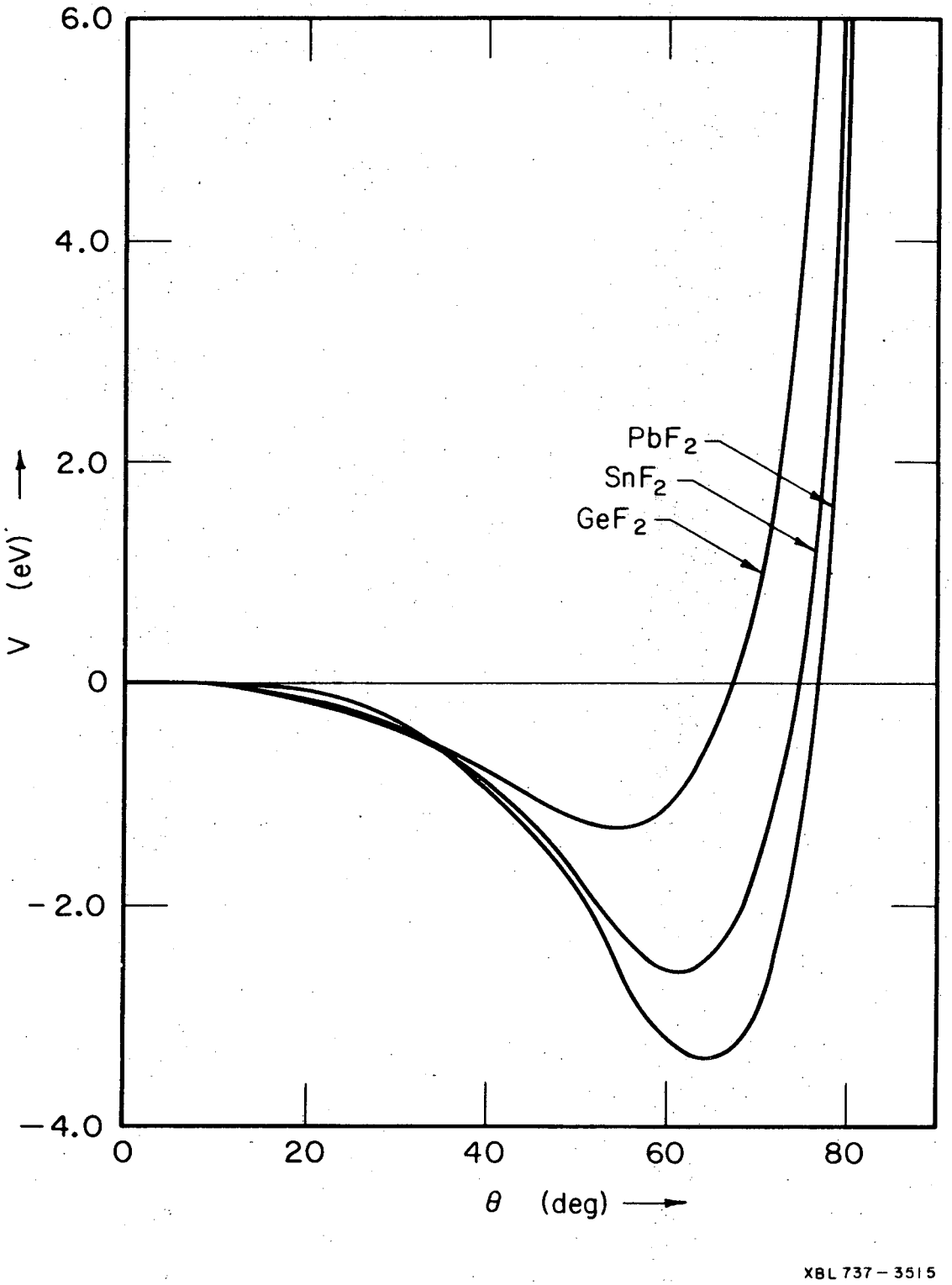

Fig. A-2-12. Group V-a fluorides.

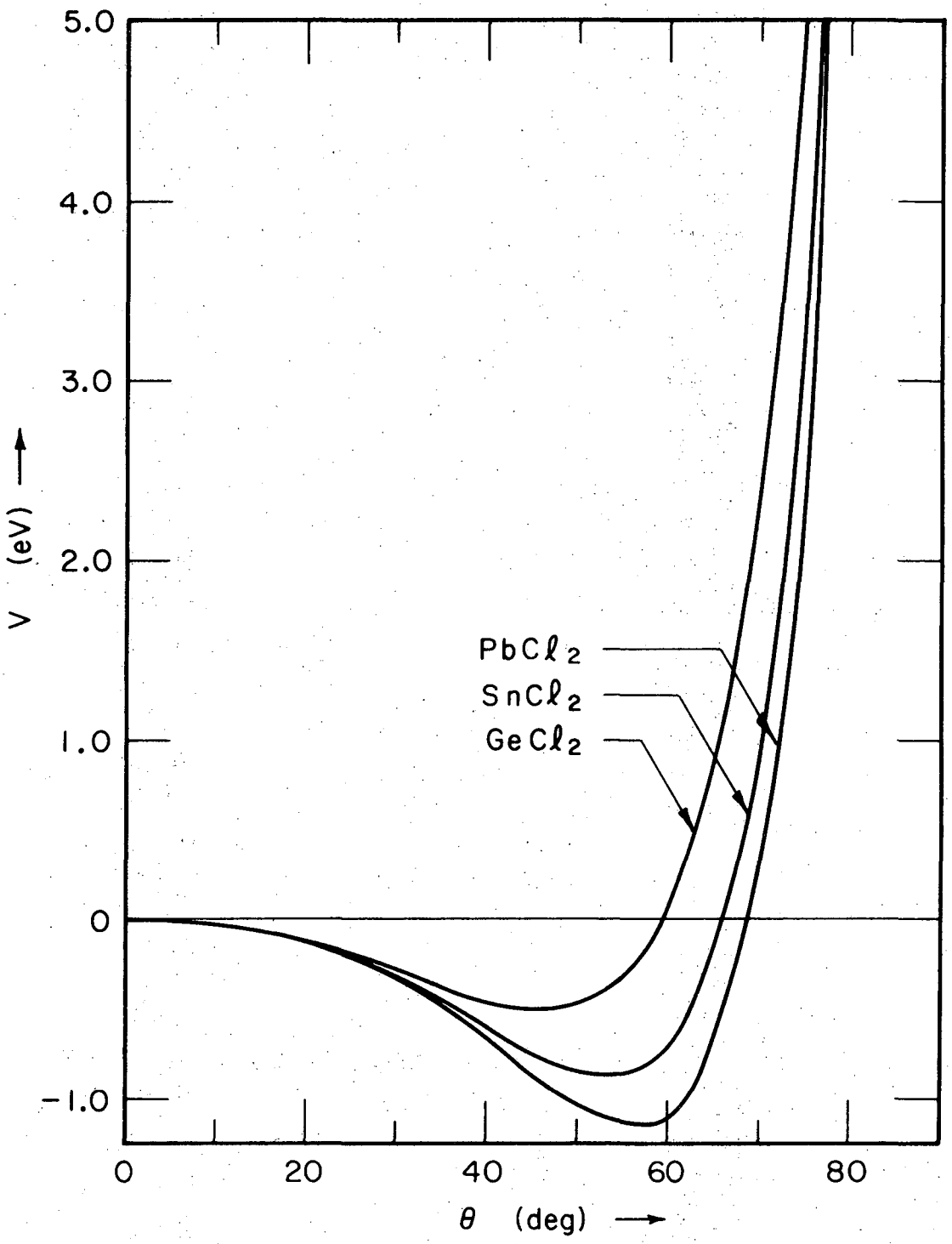

XBL 737 - 3585

Fig. A-2-13. Group V-a chlorides.

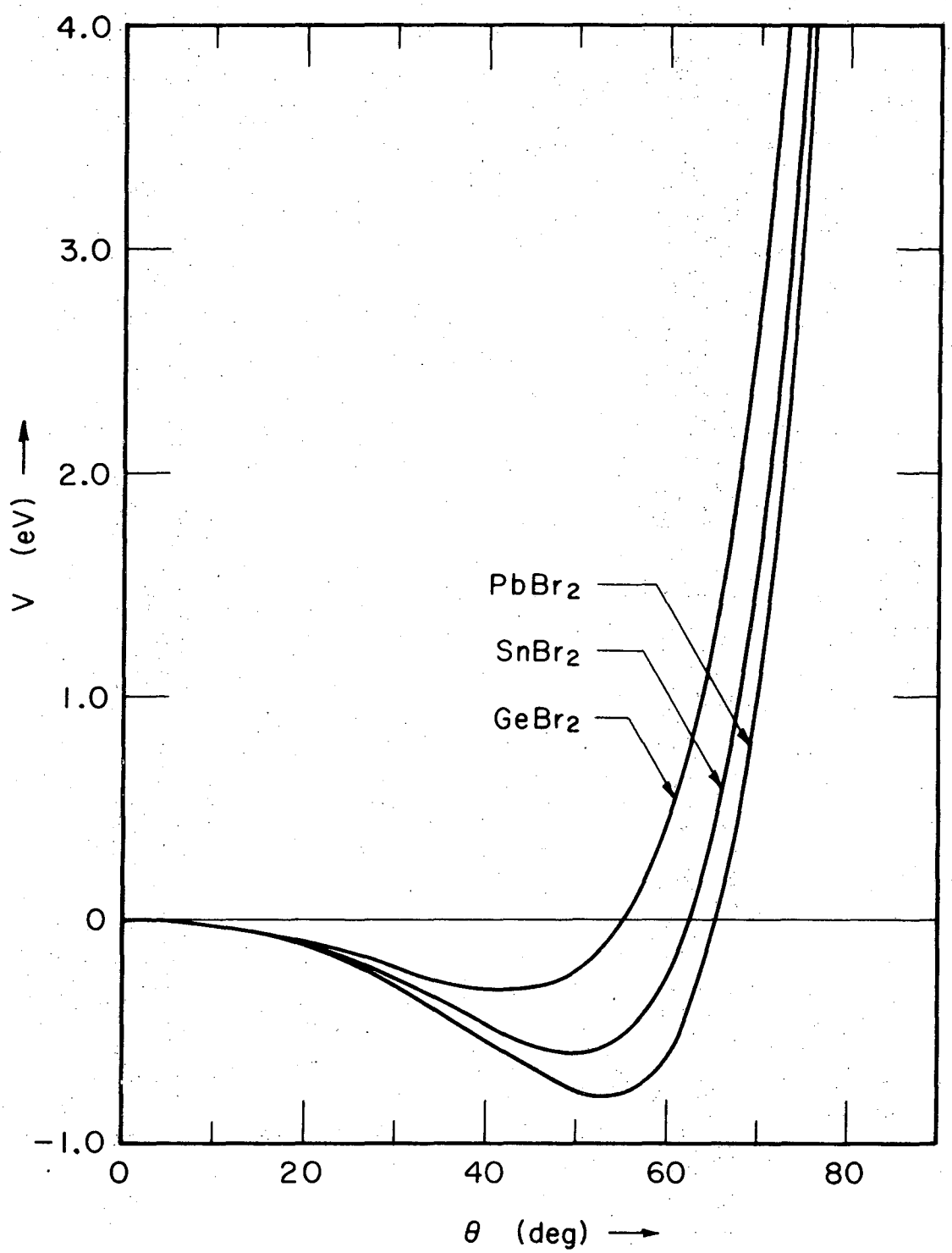

XBL 737-3586

Fig. A-2-14. Group V-a bromides.

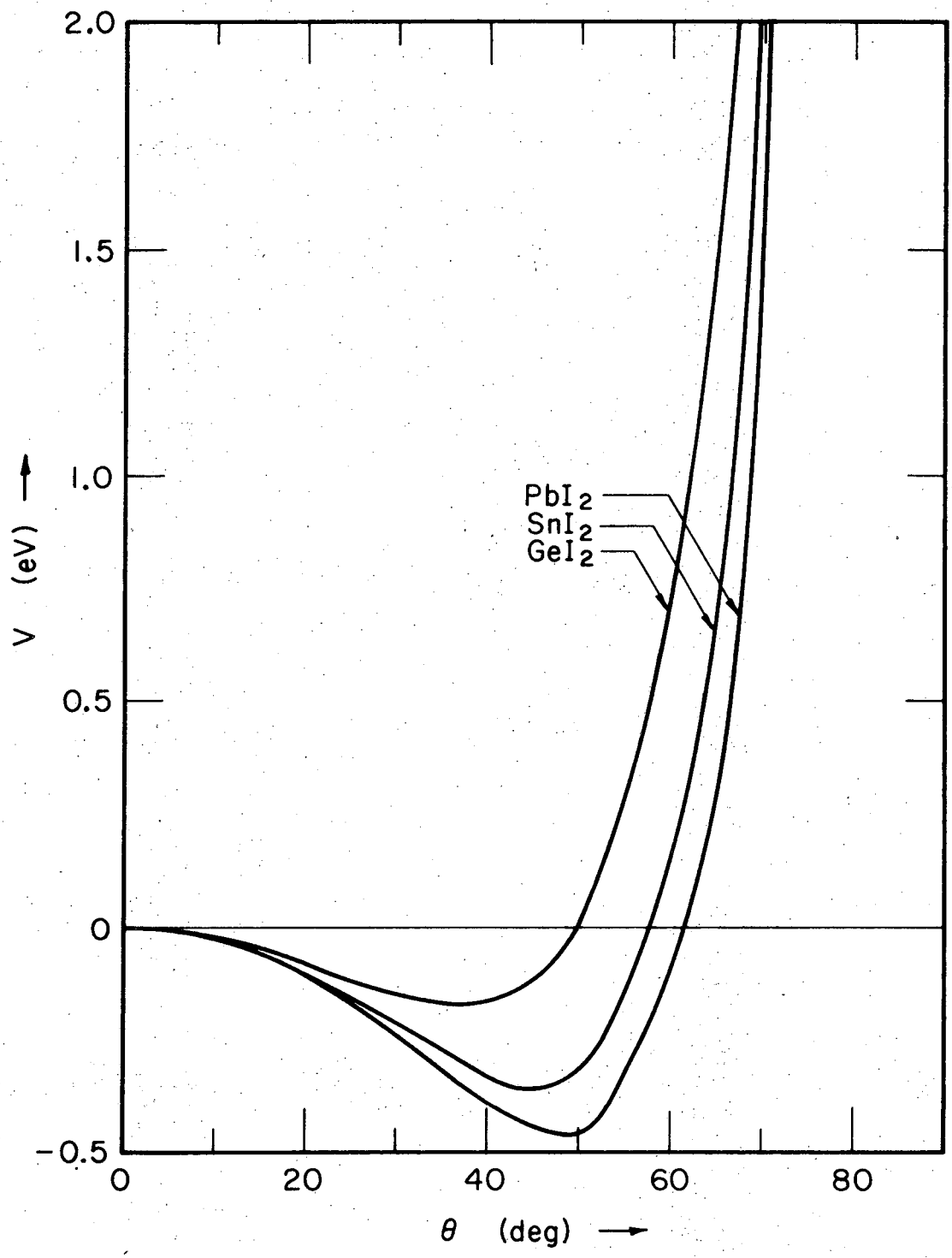

XBL737-3587

Fig. A-2-15. Group V-a iodides.

APPENDIX A-3a

Two-Dimensional Cylindrical Potential Well

Let the potential energy $\underline{V'}$ be expressed as

$$V'(y,z) = 0 \quad \text{for } y^2 + z^2 < \ell^2 \tag{II-15a}$$

$$V'(y,z) = \infty \quad \text{for } y^2 + z^2 > \ell^2 \quad . \tag{II-15b}$$

Then the Schröedinger equation is

$$-\frac{\hbar^2}{2\mu}\left(\frac{\partial^2}{\partial y^2} + \frac{\partial^2}{\partial z^2}\right) \Psi(y,z) + V'(y,z)\,\Psi(y,z) = E\Psi(y,z) \quad . \tag{II-14}$$

Converting from Cartesian to polar coordinates ($y = r\cos\omega$ and $z = r\cos\omega$),

$$\frac{\partial^2}{\partial y^2} + \frac{\partial^2}{\partial z^2} = 1/r\,\frac{\partial}{\partial r}\left(r\,\frac{\partial}{\partial r}\right) + \frac{1}{r^2}\left(\frac{\partial^2}{\partial \omega^2}\right) \quad ; \tag{A-3-1}$$

and Eq. (II-14) becomes, upon rearrangement,

$$\left[r\,\frac{\partial}{\partial r}\left(r\,\frac{\partial}{\partial r}\right) + \left(\frac{\partial^2}{\partial \omega^2}\right) - \frac{2\mu r^2}{\hbar^2}(V' - E)\right] \Psi(r,\omega) = 0 \quad . \tag{A-3-2}$$

Remembering the wavefunction $\Psi(r,\omega)$ consists of a radial term and an angular term:

$$\Psi(r,\omega) = R(r)\,\Phi(\omega) \quad . \tag{A-3-3}$$

Since $\underline{V'}$ does not depend on $\underline{r}$ or $\underline{\omega}$ in our case, Eq. (A-3-2) can be separated into two equations:

$$\frac{1}{\Phi(\omega)} \frac{d^2}{d\omega^2} \Phi(\omega) = -m^2 \tag{A-3-4a}$$

and

$$\frac{1}{R(r)} [r \frac{d}{dr}(r \frac{d}{dr}) - \frac{2\mu r^2}{\hbar^2}(V' - E)] R(r) = +m^2 \quad , \tag{A-3-4b}$$

where the constant m is the magnetic quantum number.

Redefining our variables,

$$\upsilon \equiv \frac{(E - V')}{\hbar^2} 2\mu \tag{A-3-5a}$$

and

$$\chi \equiv \sqrt{\upsilon}\, r \quad . \tag{A-3-5b}$$

Then noting that $d\chi = \sqrt{\upsilon}\, dr$ and $\sqrt{\upsilon} \frac{d}{d\chi} = \frac{d}{dr}$, Eq. (A-3-4b) is transformed into

$$[\chi \frac{d}{d\chi}(\chi \frac{d}{d\chi}) + (\chi^2 - m^2)] R(\chi) = 0 \quad . \tag{A-3-7}$$

The solutions of this differential equation are Bessel functions of order m.[128] The complete solution of this equation can be expressed by the linear combination:

$$R(\chi) = C_1 J_m(\chi) + C_2 Y_m(\chi) \quad , \tag{A-3-8a}$$

where C_1 and C_2 are constants. However, the $Y_m(\chi)$ solution does not remain finite, so the acceptable solution reduces to

$$R(\chi) = J_m(\chi) \quad . \tag{A-3-8b}$$

The computer program BSLFOO* (see Appendix A-1b) was designed to calculate these eigenfunctions $J_m(\chi)$ as a function of the energy E.

APPENDIX A-3b

Harmonic Potential with a Gaussian Perturbative Hump

Let the potential energy $\underline{V'}$ be expressed as a function of the displacement coordinate $\underline{x}$ (which is zero for a linear configuration):

$$V' = \frac{1}{2} k_b x^2 + H \exp(-\Lambda x^2) \quad . \tag{II-15c}$$

If the angle between the plane of deformation and the reference plane is $\underline{\delta}$, the system Hamiltonian is

$$\mathcal{H}_x = \frac{p_x^2}{2\mu} + \frac{p_\delta^2}{2\mu x^2} + \frac{1}{2} k_b x^2 + H \exp(-\Lambda x^2) \quad . \tag{A-3-9}$$

$\underline{p_x}$ is the momentum conjugate to $\underline{x}$, while $\underline{p_\delta}$ is the momentum conjugate to $\underline{\delta}$. Thus, the Schröedinger Eq. (II-14) can be solved for the eigenvalues and eigenfunctions. To accomplish this, the units of displacement are converted to those convenient for a harmonic oscillator:

$$\xi = \left(\frac{\sqrt{\mu k_b}}{\hbar}\right)^{\frac{1}{2}} x \quad . \tag{A-3-10a}$$

The momentum $\underline{p_x}$ is transformed to $\underline{p_\xi}$

$$p_\xi^2 = \left(\frac{\hbar}{\sqrt{k_b \mu}}\right) p_x^2 \quad . \tag{A-3-10b}$$

Substituting Eqs. (A-3-10a) and (A-3-10b) into Eq. (A-3-9),

$$\mathcal{H}_x = \frac{p_\xi^2 \sqrt{k_b}}{2\hbar\sqrt{\mu}} + \frac{p_\delta^2 \sqrt{k_b}}{2\hbar\sqrt{\mu}\,\xi^2} + \frac{\hbar\sqrt{k_b}\,\xi^2}{2\sqrt{\mu}} + H \exp(-\Lambda\,\hbar\,\xi^2/\sqrt{\mu k_b}) \quad . \tag{A-3-11a}$$

Dividing this expression by $\hbar\sqrt{k_b/\mu}$,

$$\frac{\mathcal{H}_x}{\hbar\sqrt{k_b/\mu}} = \frac{p_\xi^{\,2}}{2\hbar^2} + \frac{p_\delta^{\,2}}{2\hbar^2\,\xi^2} + \frac{\xi^2}{2} + \frac{H}{\hbar\sqrt{k_b/\mu}}\ \exp(-\Lambda\ \hbar\ \xi^2/\sqrt{k_b\ \mu})\ . \tag{A-3-11b}$$

The Hamiltonian and energy are then redefined as

$$\mathcal{H}' = \mathcal{H}_x/\hbar\sqrt{k_b/\mu} \tag{A-3-12a}$$

$$E' = E/\hbar\sqrt{k_b/\mu}\ . \tag{A-3-12b}$$

This Hamiltonian can be split into two parts

$$\mathcal{H}' = \mathcal{H}_o + \mathcal{H}_1\ , \tag{A-3-13a}$$

where

$$\mathcal{H}_o = \frac{p_\xi^{\,2}}{2\hbar^2} + \frac{p_\delta^{\,2}}{2\hbar^2\ \xi^2} + \frac{\xi^2}{2} \tag{A-3-13b}$$

$$\mathcal{H}_1 = \frac{H}{\hbar\sqrt{k_b/\mu}}\ \exp(-\Lambda\ \hbar\ \xi^2/\sqrt{k_b/\mu}) \equiv \eta\ \exp(-\lambda\ \xi^2)\ . \tag{A-3-13c}$$

$\underline{\mathcal{H}_o}$ is simply the Hamiltonian of a doubly degenerate isotropic oscillator. The corresponding eigenvalues are[129]

$$E' = h\ \nu'(v + 1)\ , \tag{A-3-14}$$

where $\underline{\nu'}$ is the bending frequency and $\underline{v}$ is the vibrational quantum number. The eigenfunctions contain associated Laguerre polynomials.[45] Redefining $\tau = \xi^2$,

$$\Psi(\tau,\delta) = \Phi(\delta)\, R^{\mathcal{L}}_{\mathcal{L}+\kappa}(\tau) \quad , \tag{A-3-15}$$

where $\underline{\mathcal{L}}$ is the angular momentum and $\kappa = \frac{1}{2}(v - \mathcal{L})$. More explicitly the radial term is

$$R^{\mathcal{L}}_{\mathcal{L}+\kappa}(\tau) = \frac{(\kappa!)^{\frac{1}{2}}}{(\mathcal{L} + \kappa)!^{3/2}}\, \tau^{\frac{1}{2}\mathcal{L}} \exp(-\tfrac{1}{2}\tau)\, L^{\mathcal{L}}_{\mathcal{L}+\kappa}(\tau) \quad . \tag{A-3-16}$$

$\underline{L^{\mathcal{L}}_{\mathcal{L}+\kappa}(\tau)}$ are the associated Laguerre polynomials; these are interrelated by

$$L^{\mathcal{L}}_{\mathcal{L}+\kappa}(\gamma\tau) = \sum_{t=0}^{\kappa} \gamma^{t}(1 - \gamma)^{\kappa-t}\, \frac{(\mathcal{L} + \kappa)!^{2}}{(\mathcal{L} + t)!^{2}(\kappa - t)!}\, L^{\mathcal{L}}_{\mathcal{L}+t}(\tau) \quad . \tag{A-3-17}$$

Let $\gamma = 1/(1 + \lambda)$ and $\tau = \gamma s$; then appropriately manipulating Eqs. (A-3-16) and (A-3-17),

$$\exp(-\tfrac{1}{2}\lambda\tau)\, R^{\mathcal{L}}_{\mathcal{L}+\kappa}(\tau) = \gamma^{\kappa+(\mathcal{L}/2)} \sum_{t=0}^{\kappa} \lambda^{\kappa-t}\, \frac{(\kappa!)^{\frac{1}{2}}(\mathcal{L} + \kappa)!^{\frac{1}{2}}}{(\kappa - t)!(\mathcal{L} + t)!^{\frac{1}{2}}(t!)^{\frac{1}{2}}} \times$$

$$\times\, R^{\mathcal{L}}_{\mathcal{L}+t}(s) \quad . \tag{A-3-18}$$

From this expression, the matrix elements of $\eta \exp(-\lambda\tau)$, necessary for a solution of the problem by perturbation theory, can be constructed:

$$\langle v_i,\mathcal{L}|\eta \exp(-\lambda\tau)|v_f,\mathcal{L}\rangle = \eta \int_0^{2\pi} \int_0^{\infty} R^{\mathcal{L}}_{\mathcal{L}+\kappa_i}(\tau)\, \Phi(\delta) \times$$

$$\times \exp(-\lambda\tau)\, R^{\mathcal{L}^*}_{\mathcal{L}+\kappa_f}(\tau)\, \Phi^*(\delta)\, d\tau\, d\delta \quad , \qquad \text{(A-3-19a)}$$

where the subscripts i and f denote initial and final states. Since $d\tau = \gamma\, ds$, and if $\kappa_i \leqslant \kappa_f$ and $u \equiv \kappa_i - t$,

$$\langle v_i,\mathcal{L}|\eta \exp(-\lambda\tau)|v_f,\mathcal{L}\rangle = \eta \int_0^{\infty} R^{\mathcal{L}}_{\mathcal{L}+\kappa_i}(\tau) \exp(-\lambda\tau) \times$$

$$\times R^{\mathcal{L}^*}_{\mathcal{L}+\kappa_f}(\tau)\, d\tau \quad . \qquad \text{(A-3-19b)}$$

The angular functions are eliminated using the property of orthonormality, while the orthonormality of the radial functions helps simplify Eq. (A-3-19b):

$$\langle v_i,\mathcal{L}|\eta \exp(-\lambda\tau)|v_f,\mathcal{L}\rangle = \gamma^{\mathcal{L}+\kappa_i+\kappa_f+1}\, \lambda^{\kappa_f-\kappa_i} \times$$

$$\times \sum_{u=0}^{\kappa_i} \frac{\lambda^{2u}[(\mathcal{L}+\kappa_i)!(\mathcal{L}+\kappa_f)!\,\kappa_i!\,\kappa_f!]^{\frac{1}{2}}}{u!(\kappa_f-\kappa_i+u)!(\kappa_i-u)!(\kappa_i+\mathcal{L}-u)!} \quad . \qquad \text{(A-3-19c)}$$

The perturbation matrix elements calculated in Eq. (A-3-19c) are added to the diagonal matrix with elements $h\,\nu'(v+1)$ (see Eq. (A-3-14)) to determine the perturbed eigenvalues. The computer program HØAEH1 (see Appendix A-1d) was designed to calculate the eigenvalues appropriate to a given harmonic potential with a Gaussian perturbative hump.

0 0 0 0 4 0 0 0 3 1

APPENDIX A-4

Component Equipment

Table V-1. List of vacuum equipment for quadrupole mass spectrometer.

COMPONENT	SPECIFICATIONS	MODEL NUMBER	MANUFACTURER
Mechanical Pump (MP)	Duo seal oil rotary vacuum pump; maximum rated speed = 7 l/sec; base pressure = 10^{-4} torr.	1397 B	Welch Scientific Co. 7300 N. Linden Ave. Skokie, Illinois
Diffusion Pump (DP-1)	Oil diffusion pump; rated pumping speed = 1400 l/sec; rated base pressure = 10^{-7} torr.	PMC 1440	Consolidated Electrodynamics Rochester Division Rochester, New York
Diffusion Pump (DP-2)	Oil diffusion pump; rated pumping speed = 300 l/sec; rated base pressure = 10^{-7} torr.	309	Consolidated Vacuum Corp. Rochester, New York
Ion Pumps (IP-1 & 2)	Vacion pumps, two in number; pumping speed = 8 l/sec.		Varian Associates Palo Alto, California
Ion Pump Control Unit (not pictured)	Vacion control unit.	921-0014	Varian Associates Palo Alto, California
Valve (V-1)	Aluminum gate valve for high vacuum; 6" diameter; manual throttling; 150#ASA flange style.	VCS 61B	Consolidated Vacuum Corp. Rochester, New York
Valve (V-2)	Aluminum gate valve for high vacuum; 4" diameter; manual throttling; light flange.	STL-1	Temescal Metallurgical Co. Berkeley, California
Valve (V-3)	Brass gate valve; 1 $\frac{1}{2}$" diameter.		CHA Industries Palo Alto, California

(continued)

Table V-1 (continued)

COMPONENT	SPECIFICATIONS	MODEL NUMBER	MANUFACTURER
Valves (V-4, V-5, V-6)	Aluminum gate valves; 2" diameter.	STL-1	Temescal Metallurgical Co. Berkeley, California
Valve (V-7)	Brass gate valve, 1 $\frac{1}{2}$" diameter.		NRC Equipment Corp. Palo Alto, California
Ion Gauges (not pictured)	UCRL ion gauge tubes.	V6/1A	LBL*
Power Supply (not pictured)	Standard ion gauge power supply.		LBL* Plan No. 17X 1405W2
Vacuum Gauge Tubes (M-1, M-2)	Vacuum gauge tubes, two in number.	DV-3M	Hastings Company Hampton, Virginia
Vacuum Interlock (not pictured)	Vacuum gauge monitor; dual DV-3M.		LBL* Plan No. 4X 9334
Diffusion Pump Power Interlock (not pictured)	Diffusion pump monitor.	#2	LBL* Plan No. 4X 5964

*Lawrence Berkeley Laboratory, Berkeley, California 94720.

N.B. Code given in parenthesis after each component refers to Fig. V-1.

Table V-2. Electronic equipment for mass spectrometer signal detection system.

COMPONENT	SPECIFICATIONS	MODEL NUMBER	MANUFACTURER
Picoammeter	High speed picoammeter; output impedance 5 ohms; output signal = 1 milliamp, 3 volts.	417	Keithley Instruments Co. Cleveland, Ohio
Low-noise Amplifier	Low-noise amplifier; maximum gain = 104.	CR4	Princeton Applied Research Princeton, New Jersey
Input Transformer	Impedance matching transformer; range = 5 Hz to 10 kHz.	AM-1	Princeton Applied Research Princeton, New Jersey
Lock-in Amplifier	Lock-in amplifier; frequency range = 1.5 Hz to 150 kHz.	JB-5	Princeton Applied Research Princeton, New Jersey
Chart Recorder	10 millivolt recorder; dual pen.	Speedomax G	Leeds and Northrup Co. North Wales, Pennsylvania
Power Supplies	Transistorized power supplies, two in number; output range = 0 to 50 volts dc, 0 to 1.5 amps.	5015	Power Designs, Inc. New York, New York
Voltage to RPM Motor Control	Voltage to RPM motor control.		LBL* Plan No. 13X 2270
Power Amplifier	Direct coupled solid state amplifier; 700 watts r.m.s.; frequency range = 0 Hz to 20. kHz.		Phase Linear, Inc. Seattle, Washington
Motor	Synchronous hysteresis motor; 2-pole; 400 cycle, 42 volts maximum power input.	75A570	Globe Industries, Inc. Dayton, Ohio

*Lawrence Berkeley Laboratory, Berkeley, California 94720.

Table V-3. Electronic equipment for data retrieval system.

UNIT	MODEL NUMBER	MANUFACTURER
Linear pre-amplifier (long time constant)		LBL* Plan No. 11X 6541-P1
Transistorized linear pulse amplifier		LBL* Plan No. 15X 4845
Single channel analyzer	NC-11	Hammer Electronic Co., Inc. Princeton, New Jersey
Electronic counter	5245L	Hewlett-Packard Co. Palo Alto, California
Nim standard regulated power supply (6 volts DC)	AEC-650	Power Designs Pacific, Inc. Palo Alto, California
4 Quad multiplexer (restart delay 1.0 msec.)		LBL* Plan No. 19X 3121-P1
4 Quad multiplexer relay box		LBL* Plan No. 19X 3141-P1
Frequency synchronizer control		LBL* Plan No. 19X 2691-P1
Switch programed time based oscillator		LBL* Plan No. 15X 8410
Multichannel analyzer (1024 channels in 4 quadrants, 3×10^{-5} seconds dead time per channel)	NS-611	Northern Scientific, Inc. Madison, Wisconsin
Paper tape printer	1200	Mohawk Data Science Corp. Franklin Electronics, Inc. King of Prussia, Pennsylvania

*Lawrence Berkeley Laboratory, Berkeley, California 94720.

REFERENCES

1. P. Debye, Polar Molecules (Dover Publications, New York, 1945).

2. E. S. Rittner, J. Chem. Phys. 19, 1030 (1951).

3. A. Honig, M. Mandel, M. L. Stitch, and C. H. Townes, Phys. Rev. 96, 629 (1954).

4. W. Klemperer and S. A. Rice, J. Chem. Phys. 26, 618 (1957).

5. S. A. Rice and W. Klemperer, J. Chem. Phys. 27, 573 (1957).

6. W. Klemperer, W. G. Norris, and A. Büchler, J. Chem. Phys. 33, 1534 (1960).

7. C. D. Hollowell, The Molecular-Beam Electric-Resonance Spectra of LiF, NaF, and KCl (Ph.D. Thesis), Lawrence Radiation Laboratory Report UCRL-17019, November 1966.

8. F. J. Lovas, Radio Frequency Stark Spectra of RbF, RbCl, CsF, CsCl, and NaI (Ph.D. Thesis), Lawrence Radiation Laboratory Report UCRL-17909, November 1967.

9. C. D. Hollowell (Lawrence Berkeley Laboratory, University of California, Berkeley, California) private communication, March 1973.

10. "Dipolmomente und Chemische Struktur", (Leipziger Vortrage 1929, P. Debye, ed., S. Hirzel, Leipzig, 1929); P. Debye, Polar Molecules (Dover Publications, New York, 1945), 2nd ed.

11. J. H. Van Vleck, The Theory of Electric and Magnetic Susceptibilities (Oxford University Press, London, 1932).

12. A. Büchler, J. L. Stauffer, and W. Klemperer, J. Am. Chem. Soc. 86, 4544 (1964).

13. R. G. Pearson, J. Chem. Phys. 30, 1537 (1959).

14. R. S. Berry, J. Chem. Phys. 30, 286 (1959).

15. A. Büchler, W. Klemperer, and A. G. Emslie, J. Chem. Phys. 36, 2499 (1962).

16. There is ample precedent for bent triatomic molecules in chemistry, while there is no indication of any triatomic molecule of the type MX_2 asymmetric due to unequal bonds.

17. R. M. Eisberg, Fundamentals of Modern Physics (John Wiley and Sons, Inc., New York, 1961), pp. 365-368.

18. E. A. Mason and J. T. Vanderslice, Atomic and Molecular Processes, ed. by D. R. Bates (Academic Press, New York, 1962), Chapter 17.

19. I. Amdur and J. E. Jordan, Advan. Chem. Phys. 10, 29 (1966).

20. J. E. Jordan, S. O. Colgate, I. Amdur, and E. A. Mason, J. Chem. Phys. 52, 1143 (1970).

21. H. Inouye and S. Kita, J. Chem. Phys. 56, 4877 (1972).

22. D. D. Konowalow and D. S. Zakheim, J. Chem. Phys. 57, 4375 (1972).

23. A. Dalgarno, Advan. Phys. 11, 281 (1962).

24. J. E. Mayer and M. G. Mayer, Phys. Rev. 43, 605 (1933).

25. G. Burns, Phys. Rev. 115, 1198 (1959).

26. J. Jeans, The Mathematical Theory of Electricity and Magnetism (University Press, Cambridge, England, 1925), 5th ed., p. 189.

27. Ibid., p. 94, pp. 184 et seq.

28. N. H. Frank, Introduction to Electricity and Optics (McGraw-Hill Book Company, Inc., New York, 1950), 2nd ed., p. 50.

29. P. A. Akishin and V. P. Spiridonov, Kristallografiya 2, 475 (1957); P. A. Akishin, V. P. Spiridonov, G. A. Sobolev, and V. A. Naumov, Zh. Fiz. Khim. 31, 461, 648, 1871 (1957); 32, 58 (1958).

30. P. A. Akishin, V. P. Spiridonov, and G. A. Sobolev, Dokl. Akad. Nauk SSSR 118, 1134 (1958); P. A. Akishin and V. P. Spiridonov, Zh. Fiz. Khim. 32, 1682 (1958).

31. B. Edlen, "Atomic Spectra", in Handbuch der Physik, ed. by S. Flügge, XXVII (Springer-Verlag, Berlin, 1959).

32. L. Pauling, Proc. Roy. Soc. (London) A114, 191 (1927).

33. A. Snelson, J. Phys. Chem. 72, 250 (1968).

34. A. Snelson, J. Phys. Chem. 70, 3208 (1966).

35. A. Büchler and W. Klemperer, J. Chem. Phys. 29, 121 (1958).

36. G. V. Calder, D. E. Mann, K. S. Seshadri, M. Allavena, and D. White, J. Chem. Phys. 51, 2093 (1969).

37. D. E. Mann, G. V. Calder, K. S. Seshadri, D. White, and M. J. Linevsky, J. Chem. Phys. 46, 1138 (1967).

38. S. P. Randall, F. T. Greene, and J. L. Margrave, J. Phys. Chem. 63, 758 (1959).

39. J. W. Hastie, R. H. Hauge, and J. L. Margrave, High Temp. Sci. 3, 257 (1971).

40. Ibid., 3, 56 (1971).

41. P. J. Dagdigian and L. Wharton, J. Chem. Phys. 58, 1243 (1973).

42. G. M. Barrow, J. Chem. Phys. 26, 558 (1957).

43. W. H. Shaffer, Revs. Mod. Phys. 16, 245 (1944).

44. W. R. Thorson and I. Nakagawa, J. Chem. Phys. 33, 994 (1960).

45. J. D. Swalen and J. A. Ibers, J. Chem. Phys. 36, 1914 (1962).

46. S. I. Chan, J. Zinn, J. Fernandez, and W. D. Gwinn, J. Chem. Phys. 33, 1643 (1960).

47. R. N. Dixon, Trans Faraday Soc. 60, 1363 (1964).

48. S. I. Chan and D. Stelman, J. Chem. Phys. 39, 545 (1963).

49. V. I. Baikov, Opt. Spektrosk. 25, 356 (1968).

50. R. M. Sternheimer, Phys. Rev. 118, 1198 (1959); ibid., 107, 1565 (1957).

51. O. Bastiansen and E. W. Lund, Ann. Rev. Phys. Chem. 10, 31 (1959).

52. L. E. Sutton, Special Publications No. 11, The Chemical Society, London (1958).

53. J. R. Tessman, A. H. Kahn, and W. Shockley, Phys. Rev. 92, 890 (1953).

54. J. W. Hastie, R. H. Hauge, and J. L. Margrave, High Temp. Sci. 1, 76 (1969).

55. A. Lowenschuss, A. Ron, and O. Schnepp, J. Chem. Phys. 49, 272 (1968).

56. Ibid., 50, 2502 (1969).

57. J. W. Hastie, R. H. Hauge, and J. L. Margrave, J. Chem. Phys. 51, 2648 (1969).

58. K. R. Thompson and K. D. Carlson, J. Chem. Phys. 49, 4379 (1968).

59. J. W. Hastie, R. H. Hauge, and J. L. Margrave, J. Chem. Soc. D Chem. Commun. 1452 (1969).

60. C. W. DeKock, R. D. Wesley, and D. D. Radtke, High Temp. Sci. 4, 41 (1972).

61. J. W. Hastie, R. Hauge, and J. L. Margrave, J. Phys. Chem. 72, 4492 (1968).

62. H. Sponer and E. Teller, Revs. Mod. Phys. 13, 75 (1941).

63. M. Wehrli, Helv. Phys. Acta 11, 339 (1938).

64. M. Wehrli, Helv. Phys. Acta 13, 153 (1940).

65. J. T. Waber and D. T. Cromer, J. Chem. Phys. 42, 4116 (1965).

66. B. Fricke and J. T. Waber, J. Chem. Phys. 56, 3246 (1972).

67. K. M. S. Saxena and S. Fraga, J. Chem. Phys. 57, 1800 (1972).

68. G. Horzberg, Molecular Spectra and Molecular Structure II. Infrared and Raman Spectra of Polyatomic Molecules (D. Van Nostrand Company, Inc., Princeton, New Jersey, 1945), pp. 239-240.

69. K. Street, Jr. (Chemistry Department, University of California, Berkeley, California) private communication, March 1973.

70. N. Bjerrum, Verh. d. d. Phys. Ges. 16, 737 (1914).

71. Ref. 68, pp. 168-173.

72. V. I. Baikov, Opt. Spekstrosk. 27, 923 (1969).

73. F. T. Greene and T. A. Milne, Advan. Mass Spectrom. 4, 301 (1968).

74. C. H. Townes and A. L. Schawlow, Microwave Spectroscopy (McGraw-Hill Book Company, Inc., New York, 1955).

75. G. Herzberg, Molecular Spectra and Molecular Structure I. Spectra of Diatomic Molecules (D. Van Nostrand Company, Inc., Princeton, New Jersey, 1959), 6th ed.

76. W. Gordy and R. L. Cook, Microwave Molecular Spectra (Interscience Publishers, New York, 1970), 2nd ed.

77. H. G. Bennewitz, W. Paul, and C. Schlier, Z. Physik 141, 6 (1955).

78. C. A. Melendres, Radio Frequency Stark Spectra of NaCl, NaBr, and BaS by the Molecular Beam Electric Resonance Method (Ph.D. Thesis), Lawrence Radiation Laboratory Report UCRL-18344, June 1968.

79. L. Wharton, R. A. Berg, and W. Klemperer, J. Chem. Phys. 39, 2023 (1963).

80. T. Coor, Industrial Research, 52 (May 1972).

81. M. Kaufman and C. E. Kolb, Chem. Instrum. 3, 175 (1971).

82. C. E. Kolb and M. Kaufman, J. Phys. Chem. 76, 947 (1972).

83. W. Paul, H. P. Reinhard, and U. von Zahn, Z. Physik 152, 143 (1958).

84. J. W. Hastie and D. L. Swingler, High Temp. Sci. 1, 46 (1969).

85. A thoriated iridium filament was chosen to ensure a longer filament lifetime and to provide a strong source of electrons at significantly lower temperatures than either a pure iridium or a tungsten filament would permit.

86. M. Knudsen, The Kinetic Theory of Gases (Methuen and Company, Ltd., London, 1934).

87. R. G. J. Fraser, Molecular Rays (Cambridge University Press, Cambridge, 1931).

88. I. Estermann, Revs. Mod. Phys. 18, 300 (1946).

89. R. C. Miller and P. Kusch, Phys. Rev. 99, 1314 (1955).

90. N. F. Ramsey, Molecular Beams (Clarendon Press, Oxford, 1956).

91. T. L. Story, Jr., Dipole Moments of Alkali Halides by the Electric Deflection Method (Ph.D. Thesis), Lawrence Radiation Laboratory Report UCRL-18484, September 1968.

92. C. I. Whitman, J. Chem. Phys. 20, 161 (1952).

93. M. G. Rossman and J. Yarwood, J. Chem. Phys. 21, 1406 (1953).

94. J. D. Dake (Department of Chemistry, Louisiana State University, Baton Rouge, Louisiana) private communication, August 1968.

95. A. J. Hebert (Lawrence Berkeley Laboratory, University of California, Berkeley, California) private communication, May 1970.

96. D. J. Meschi, J. Phys. Chem. 76, 2947 (1972).

97. A. J. Hebert, F. W. Breivogel, Jr., and K. Street, Jr., J. Chem. Phys. 41, 2368 (1964).

98. J. W. Green, G. D. Blue, T. C. Ehlert, and J. L. Margrave, J. Chem. Phys. 41, 2245 (1964).

99. O. Ruff and L. LeBoucher, Z. Anorg. Allgem. Chem. 219, 376 (1934).

100. L. Brewer, G. R. Somayajulu, and E. Brackett, Chem. Rev. 63, 111 (1963).

101. R. D. Loehman, R. A. Kent, and J. L. Margrave, J. Chem. Eng. Data 10, 296 (1965).

102. D. T. Peterson and J. F. Hutchison, J. Chem. Eng. Data 15, 320 (1970).

103. G. D. Blue, J. W. Green, R. G. Bautista, and J. L. Margrave, J. Phys. Chem. 67, 877 (1963).

104. M. Allavena and S. Besnainov, J. Mol. Struct. 11, 439 (1972).

105. J. F. Labarre and C. Leibovici, J. Chim. Phys. 69, 541 (1972).

106. M. Astier, Compt. Rend. C270, 911 (1970).

107. M. Astier and P. Millie, J. Organomet. Chem. 31, 139 (1971).

108. K. G. Gunther, Glastechnol. Ber. 31, 9 (1958).

109. R. R. Hammer, The Vapor Pressure of Magnesium Fluoride (Ph.D. Thesis), University of California, Berkeley, 1961.

110. J. Berkowitz and J. R. Marquart, J. Chem. Phys. 37, 1853 (1962).

111. D. L. Hildenbrand, W. F. Hall, F. Ju, and N. D. Potter, J. Chem. Phys. 40, 2882 (1964).

112. E. E. Schrier and H. M. Clark, J. Phys. Chem. 67, 1259 (1963).

113. P. A. Akishin, V. A. Naumov, and V. M. Tatevskii, Vestnik Moskov. Univ., Ser. Mat., Mekh., Astron., Fiz., Khim. 14, 229 (1959); P. A. Akishin and V. A. Naumov, Nauch. Doklady Vysshei Shkoly, Khim. i Khim. Tekhnol. No. 1, 5 (1959).

114. R. D. Wesley and C. W. DeKock, J. Chem. Phys. 55, 3866 (1971).

115. R. H. Hauge, J. W. Hastie, and J. L. Margrave, J. Less-Common Metals 23, 359 (1971).

116. E. W. Kaiser, W. E. Falconer, and W. Klemperer, J. Chem. Phys. 56, 5392 (1972).

117. R. A. Kent, K. F. Zmbov, A. S. Kana'an, G. Besenbruch, J. D. McDonald, and J. L. Margrave, J. Inorg. Nucl. Chem. 28, 1419 (1966).

118. K. F. Zmbov and J. L. Margrave, J. Less-Common Metals 12, 494 (1967); ibid., Advan. Chem. Ser. 72, 267 (1968).

119. H. B. Skinner and A. W. Searcy, J. Chem. Phys. 75, 108 (1971).

120. J. A. Roberts, Jr. and A. W. Searcy, High Temp. Sci. 4, 411 (1972).

121. T. Moeller, The Chemistry of the Lanthanides (Reinhold Publishing Company, New York, 1963).

122. O. G. Polyachenok and G. I. Novikov, Russ. J. Inorg. Chem. 9, 429 (1964).

123. J. W. Hastie, P. Ficalora, and J. L. Margrave, J. Less-Common Metals 14, 83 (1967).

124. A. V. Hariharan and H. A. Eick, High Temp. Sci. 4, 91 (1972).

125. J. M. Haschke and H. A. Eick, J. Phys. Chem. 74, 1806 (1970).

126. A. V. Hariharan and H. A. Eick, High Temp. Sci. 4, 379 (1972).

127. M. Astier, G. Berthier, and P. Millie, J. Chem. Phys. 57, 5008 (1972).

128. F. B. Hildebrand, Advanced Calculus for Applications (Prentice-Hall, Inc., Englewood Cliffs, New Jersey, 1965), 5th ed., pp. 142 et seq.

129. A. Messiah, Quantum Mechanics (North-Holland Publishing Co., Amsterdam 1961), Vol. I, pp. 454-456.

LEGAL NOTICE

This report was prepared as an account of work sponsored by the United States Government. Neither the United States nor the United States Atomic Energy Commission, nor any of their employees, nor any of their contractors, subcontractors, or their employees, makes any warranty, express or implied, or assumes any legal liability or responsibility for the accuracy, completeness or usefulness of any information, apparatus, product or process disclosed, or represents that its use would not infringe privately owned rights.

TECHNICAL INFORMATION DIVISION
LAWRENCE BERKELEY LABORATORY
UNIVERSITY OF CALIFORNIA
BERKELEY, CALIFORNIA 94720